



universität
wien

DISSERTATION

Titel der Dissertation

“Pulsation models of selected δ Scuti stars”

Verfasser

Mag. rer. nat. Patrick Lenz

angestrebter akademischer Grad

Doktor der Naturwissenschaften (Dr. rer. nat.)

Wien, im September 2009

Studienkennzahl lt. Studienblatt:
Dissertationsgebiet lt. Studienblatt:
Betreuer:

A 091 413
Astronomie
O. Univ. Prof. Dr. Michel Breger

Contents

1	Introduction to the δ Scuti stars	1
1.1	Theory of δ Scuti pulsations	2
1.1.1	Driving mechanism for oscillations	2
1.1.2	Oscillation properties of modes	4
1.1.3	Linear stability of pulsation modes	6
1.2	Motivation to do asteroseismology of δ Scuti stars	8
1.3	δ Scuti stars examined in this work	9
1.3.1	44 Tauri	9
1.3.2	FG Virginis	11
1.3.3	4 Canum Venaticorum	12
1.3.4	Position of 4 CVn, FG Vir and 44 Tau in the HR diagram	13
2	The computational tools to study δ Scuti stars	15
2.1	Warsaw - New Jersey stellar evolution code	15
2.2	Dziembowski's pulsation code	16
2.3	Treatment of stellar rotation	17
2.4	Input data for the models	18
2.4.1	Element abundance mixtures for stellar models	19
2.4.2	Equation of state	20
2.4.3	Opacity data	21
2.4.4	Implementation of updated low-temperature opacities into the codes	22

3	Mode identification and its diagnostic power	26
3.1	Mode identification techniques	26
3.1.1	A least-squares approach for three passbands (the DD-method)	28
3.2	Application to 44 Tau	31
3.2.1	Photometric mode identification	31
3.2.2	Spectroscopic mode identification	38
3.2.3	Mode identification with the DD-method	39
3.2.4	Summary of mode identification for 44 Tau	39
3.3	Application to 4 CVn	41
3.3.1	Photometric mode identification	41
3.3.2	Spectroscopic mode identification	47
3.3.3	Application of the DD-method	48
3.3.4	Summary of mode identification for 4 CVn	50
4	Asteroseismic modeling of 44 Tau	51
4.1	The choice of the element mixture	52
4.2	Inferences from the observed radial modes	53
4.2.1	Petersen diagrams	54
4.2.2	Effect of different solar element mixtures on the radial period ratio	57
4.2.3	Effect of different opacity data on the radial period ratio	59
4.2.4	Effect of the CEFF equation of state on the period ratio	63
4.3	Main sequence models	64
4.4	Post-main sequence expansion models	68
4.4.1	Mode trapping as a mechanism of mode selection	68
4.4.2	Mode instability	70
4.5	Post-MS contraction models	72
4.6	Mixed modes as probes of the stellar core region	75
4.7	Predictions of the post-MS contraction model	78
4.8	Variability of photometric mode amplitudes	81
4.8.1	A geometrical explanation: precession of the pulsation axis	82
4.8.2	Beating between close frequencies	84
4.8.3	Resonant coupling of pulsation modes	87

5	Asteroseismic models for 4 CVn	91
5.1	Validity of the perturbation approach for rotation in the case of 4 CVn . . .	91
5.2	Inferences from the observed radial mode	92
5.2.1	Post-main sequence models in the expansion phase	93
5.2.2	Post-main sequence models in the contraction phase	95
5.2.3	Main sequence models	96
5.2.4	Theoretical frequency spectra	96
6	Determination of intrinsic mode amplitudes	101
6.1	The method	102
6.2	Intrinsic mode amplitudes of 44 Tau	102
6.3	Intrinsic mode amplitudes of FG Vir	105
6.4	Discussion	106
7	Conclusion	111
	Bibliography	118
A	Appendix	119
A.1	Zusammenfassung	119
A.2	Abstract	121
A.3	Danksagung / Acknowledgement	122
A.4	Lebenslauf	123

Chapter 1

Introduction to the δ Scuti stars

δ Scuti stars are pulsating stars with spectral types between A0 and F2 and periods between 18 minutes and 8 hours. Their masses range between 1.5 and 2.5 solar masses and their source of energy is hydrogen burning in the core, or in more evolved phases, hydrogen shell burning. In the Hertzsprung-Russell diagram (or shorter: HR diagram) they are situated in the lower part of the classical Cepheid instability strip. Figure 1.1 schematically shows the part of the HR diagram in which the δ Scuti stars are located.

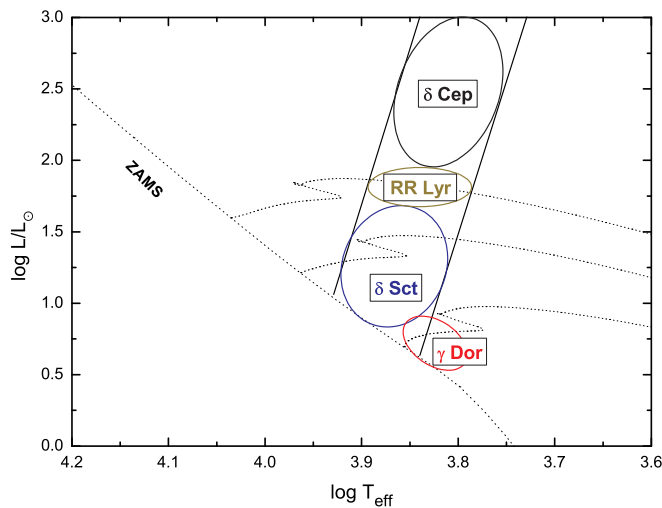


Figure 1.1: HR diagram with the schematic position of different types of pulsators in the classical instability strip. The evolutionary tracks for Population I models with 1.5, 2.0 and 2.5 M_{\odot} are shown. For better clarity only a few types of pulsators are shown in the diagram, omitting some other groups of pulsators in the same region.

In the HR diagram the δ Scuti stars are surrounded by other types of pulsators with different oscillation characteristics. The instability strips of different groups of pulsators

partly overlap. At the extension of the instability strip to higher luminosities the RR Lyrae stars and Cepheids can be found. Contrary to the δ Scuti stars which are main sequence and immediate post-main sequence stars (exhibiting hydrogen core or shell burning, respectively), the RR Lyrae stars are more evolved objects of Population II or old Population I. They are in the helium core burning phase on the so-called horizontal branch and have typical masses around $0.8 M_{\odot}$ and periods less than one day. The classical Cepheids are also in an advanced evolutionary stage with central helium burning but have higher masses between $5\text{-}15 M_{\odot}$. Their periods are longer than those of the RR Lyrae stars and are of the order of days and months.

On the red edge, or in other words, the cold border of the instability strip the δ Scuti pulsators overlap with the γ Doradus stars. These stars are main sequence stars with periods of the order of one day and masses between 1.4 and $1.8 M_{\odot}$. Stars in which both γ Dor and δ Scuti-like periods are excited have already been found (e.g., Henry & Fekel 2005). Due to their dual nature these stars are sometimes called hybrid pulsators.

One group of pulsators which has similar periods as the δ Scuti stars, are the β Cephei stars. The main differences between the two groups are due to the different fundamental parameters, since the β Cephei stars are primarily main sequence B-stars with masses around 8 to $12 M_{\odot}$. The physical processes that drive the pulsations will be discussed in the next sections.

1.1 Theory of δ Scuti pulsations

δ Scuti stars pulsate in radial and nonradial modes. Radial pulsation maintains the spherical symmetry of a star. This is not the case for nonradial oscillations, which cause some parts of the stellar surface to contract while other parts expand. Since the radius variation due to pulsation is small compared to the stellar radius the surface geometry of the oscillations can be described by spherical harmonics, Y_{ℓ}^m . ℓ is the spherical degree of the pulsation mode; it characterizes the number of node lines on the surface of the star. m is the azimuthal order and represents the number of node circles crossing the equator in latitudinal direction. By definition $|m|$ can only be lower or equal to ℓ . In this work we use the common terminology of denoting modes with $m = 0$ as zonal modes, $|m| < \ell$ as tesseral and $|m| = \ell$ as sectoral modes. The sign of the azimuthal order determines whether a mode is prograde (i.e., a running wave in the direction of rotation), retrograde or axisymmetric ($m = 0$). According to the sign convention used in this work, positive m indicate prograde modes.

1.1.1 Driving mechanism for oscillations

The observed pulsations of stars are caused by a mechanism that transforms thermal energy into mechanical energy of oscillation. Consequently, pulsating stars are nothing but a thermodynamical heat engine. This was already noted by Eddington (1919) who suggested this mechanism to explain the pulsation of the radially oscillating Cepheids.

In a stellar layer in which the opacity, κ , increases with increasing temperature, e.g., due to compression, the radiative flux will be blocked in the compression phase. The second temperature derivative of κ is positive in outward direction in such a case. Energy is temporarily stored in that layer and transformed into expansion work. Contrary to the concept of a usual combustion engine (which is based on a variation-of-heat concept) the energy generation in the center of a star remains constant over a work cycle. However, in the zones where the second temperature derivative of κ is positive the energy leakage varies with temperature. The opacity driving mechanism, therefore, acts like a valve mechanism in such a layer. This mechanism is commonly termed κ mechanism.

The second temperature derivative of the opacity is positive when the first temperature derivative, κ_T , is increasing, which occurs at different temperatures inside a star as can be seen in the lower panel of Figure 1.2 for a δ Scuti model. The zones where κ_T increases in outward direction are connected to bumps in the opacity shown in the upper panel of the diagram. The opacity bumps are situated at temperatures at which the ionization of specific abundant elements takes place. As marked in Figure 1.2 the partial ionization zone of neutral hydrogen and neutral helium are located close to the surface at a temperature of approximately 14 000 K. The second ionization of helium (He II) occurs at a temperature of 45 000 K and the so-called Z bump at 200 000 K is attributed to the partial ionization of M-shell electrons of iron. In these partial ionization zones the specific elements are permanently ionized and recombined due to pulsation.

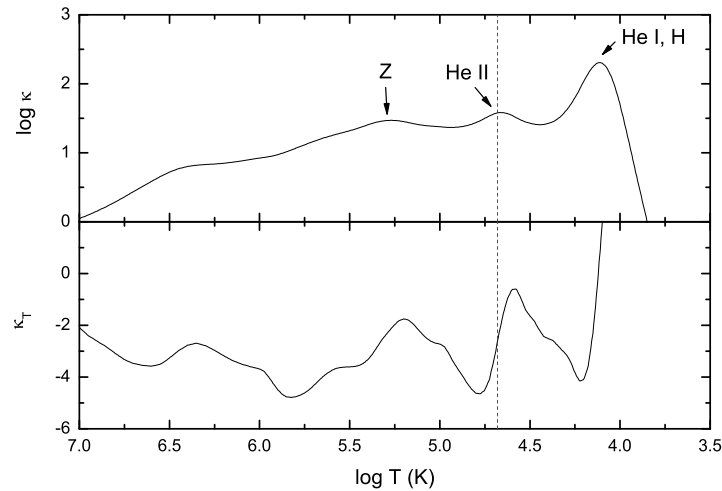


Figure 1.2: Variation of opacity, κ , and its temperature derivative from the center (left) to the surface (right) inside a post-main sequence δ Scuti model. The vertical line marks the stellar layer in which the conditions are favorable for the κ mechanism to excite pulsations in δ Scuti stars.

It was shown by Cox (1963) that in most of the stars situated in the classical instability strip the opacity mechanism is acting in the partial ionization zone of He II. It is exactly

the same mechanism which drives the pulsations in δ Scuti stars and in the more evolved RR Lyrae stars and Cepheids. Contrary, the more massive β Cephei pulsators with masses around 8-12 M_{\odot} , were found to be unstable due to the opacity mechanism operating at the Z bump (Moskalik & Dziembowski 1992; Cox et al. 1992).

For low degree modes in δ Scuti stars the ionization zones of neutral helium and hydrogen have a negligible contribution to the driving. However, the contribution of these outer layers slowly increases with the spherical degree of the mode. It was shown by Dziembowski (1980) that for modes with $\ell=80-100$ the He I and H ionization zone dominate the driving. Currently, such modes are only of theoretical interest because even with present day satellites it is very unlikely that they can be observed due to their expected small amplitudes.

1.1.2 Oscillation properties of modes

Solving the equations of linear stellar oscillations leads to two characteristic frequencies: a critical acoustic frequency, commonly termed as Lamb frequency, defined as

$$L_{\ell}^2 = \frac{\ell(\ell+1)}{r^2} c^2, \quad (1.1)$$

where ℓ is the spherical mode degree and c is the speed of sound at the radius r from the center of the star. The Brunt-Väisälä frequency, N , is given by the equation

$$N^2 = g \left(\frac{1}{H} - \frac{g}{c^2} \right), \quad (1.2)$$

where H is the density scale height, and g the local gravity. The Brunt-Väisälä frequency is the oscillation frequency of a vertically displaced fluid element due to buoyancy. Pulsation modes can only oscillate in specific regions (so-called cavities) in the star which are constrained by the Lamb and Brunt-Väisälä frequencies:

- $\omega^2 > L_{\ell}^2$ and $\omega^2 > N^2$ where ω is the eigenfrequency of the mode.
The cavity for propagating modes that suffice these conditions is mainly situated in the outer layers of the star. Since the restoring force of oscillations in this regime is pressure, propagating modes in this cavity are called acoustic modes or p modes.
- $\omega^2 < L_{\ell}^2$ and $\omega^2 < N^2$.
In this cavity the restoring force is buoyancy. Pulsation modes propagating in this cavity are called gravity modes or shorter: g modes.

Almost all mode energy is confined to the layers where the pulsation mode can propagate. Outside the propagation zones the mode is evanescent (i.e., damped). The propagation regions defined by the Brunt-Väisälä and the Lamb frequency for dipole ($\ell=1$) modes are shown in Figure 1.3 for a post-main sequence model with 2 M_{\odot} . The inner boundary for

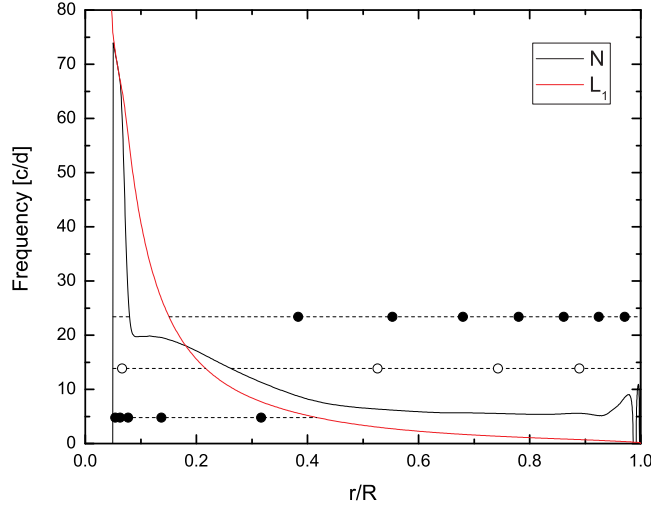


Figure 1.3: Propagation diagram for dipole modes in a post-MS model with a mass of $2 M_{\odot}$. The horizontal lines mark the propagation zones of an acoustic, a gravity and a mixed mode. The positions of the radial nodes are depicted by circles (using empty circles for the mixed mode).

the acoustic mode cavity moves closer to the surface with higher ℓ . The Brunt-Väisälä frequency shows a more complicated dependence on the radius than the Lamb frequency. Generally, the real part of the complex frequency N is zero in layers where convection takes place. Just above the convective core the Brunt-Väisälä frequency exhibits a sharp maximum. This feature is a consequence of the evolution in the chemical composition. During the main sequence evolution of a δ Scuti star the CNO cycle is the dominant energy source in hydrogen burning. The high temperature sensitivity of this nuclear process leads to the formation of a convective core. The core shrinks during the main sequence evolution and leaves behind a gradient in the mean molecular weight between the envelope (which, generally speaking, still exhibits the original element abundances) and the fully mixed hydrogen burning core. This chemical gradient affects the sound speed which enters N through equation 1.2.

The evolutionary changes of the Brunt-Väisälä frequency affect the pulsation properties of a star significantly, because the boundaries of the g mode cavity are modified. Due to the development of a maximum in the Brunt-Väisälä frequency in the partially mixed layer above the convective core, gravity modes penetrate into the frequency region of acoustic modes. When a gravity mode interacts with an acoustic mode it adopts a dual nature. This phenomenon is known as avoided crossing (Aizenman et al. 1977). The mode then acts like an acoustic mode in the envelope and like a gravity mode in the interior. Such modes are called mixed modes.

δ Scuti stars oscillate in low-order acoustic and gravity modes. In Figure 1.3 three representative pulsation modes are shown, an acoustic mode (with a frequency of 23.4 cd^{-1}), a gravity mode (4.8 cd^{-1}) and a mixed mode (13.9 cd^{-1}). In this model unstable modes are only predicted between 6.5 and 16 cd^{-1} and most of the pure p and g modes are damped. This exemplifies that the nonradial modes in evolved δ Scuti stars are mostly of mixed character. Only if a star is close to the ZAMS the gravity modes are well separated from the acoustic modes.

Commonly, the modes for each spherical degree are numbered by their radial order: for example, p_3 denotes an acoustic mode with three radial nodes and g_7 a gravity mode with seven radial nodes. This numbering scheme cannot directly be applied to mixed modes. It has been shown by Scuflaire (1974) that mixed modes exhibit additional radial nodes which appear in-between the radial nodes in the g mode cavity and the p mode cavity. For mixed modes the numbering scheme is therefore modified: the number of radial nodes in the g mode cavity is subtracted from the number of nodes in the acoustic cavity. Following this scheme a mixed mode with the label p_3 does not necessarily have only three radial nodes.

1.1.3 Linear stability of pulsation modes

As mentioned in the previous section, not all of the modes in a cavity are unstable. Whether an individual mode is unstable or not, is determined by an additional set of requirements. These additional conditions for instability are:

- (i) The amplitude of the Lagrangian pressure eigenfunction, $\delta P/P$, of the mode is large and changes only slowly in the driving region.
- (ii) The thermal relaxation time, τ_{th} , in the driving region is longer or of similar magnitude as the period of the pulsation mode. Otherwise, the heat stored in the layer leaks outward and cannot be used to perform mechanical work.

For a mode to be unstable, the driving effects have to exceed the damping effects, i.e., the dissipation of energy throughout the star. These different contributions are summed up by the work integral, W , which expresses the work done over one pulsation cycle. W is evaluated between the surface and a sphere of radius r . If the quantity W is positive local driving occurs.

The growth-rate of a mode, γ , describes the increase of oscillation energy during one cycle and is directly connected to the work integral through the equation $\gamma = \frac{W}{2\omega I}$ where I is the mode inertia and ω is the mode frequency. From a computational survey of linear growth-rates Dziembowski (1975) concluded that nonradial modes are likely to be excited along with radial modes in δ Scuti stars. This was confirmed by observations.

For a comparison between the frequency range of predicted unstable modes and the observed range of frequencies the normalized growth-rate, η , according to Stellingwerf

(1978) is commonly used,

$$\eta = \frac{\int_0^R \frac{dW}{dr} dr}{\int_0^R \left| \frac{dW}{dr} \right| dr}. \quad (1.3)$$

A value of $\eta = -1$ corresponds to full damping and $\eta = +1$ to full driving. The mode instability is mainly governed by the conditions in the stellar envelope.

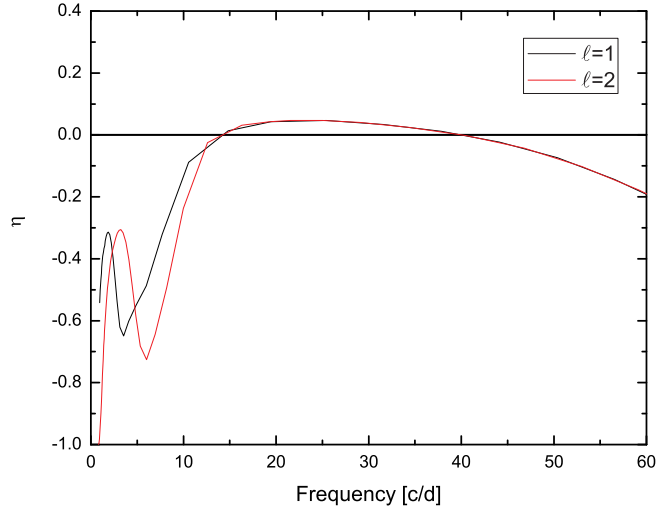


Figure 1.4: Instability parameter, η , for a main sequence model with $1.6 M_{\odot}$ and $T_{\text{eff}}=8500$ K. The results for $\ell=1$ and 2 modes are shown.

It was shown by Dziembowski & Pamiatnykh (1993) and discussed in more detail in Dziembowski et al. (1993) that for the β Cephei stars a second instability domain at low frequencies exists. The predicted unstable modes in this region are high-order g modes which are also driven by the κ -mechanism. These modes correspond to SPB (slowly pulsating B-star) pulsations.

A similar behaviour in η can be seen in some δ Scuti models. As shown in Figure 1.4 for an early main sequence δ Scuti model η is locally higher at frequencies below 5 cd^{-1} . This is the frequency region, where the γ Dor pulsations are expected. However, due to the negative values of η at this low-frequency bump no mode driving occurs. Currently, a convective blocking mechanism is the most promising explanation for the oscillations of γ Dor stars (Guzik et al. 2000). Nevertheless, the somewhat lower damping at low frequencies may contribute to the mode instability.

The reason for the given variation of η with frequency shown in Figure 1.4 is related to condition (i) mentioned above. At high frequencies relative Lagrangian pressure variation, $\delta P/P$, varies too rapidly in the driving region and in the frequency region in-between the absolute value of $\delta P/P$ is too small in the driving region.

1.2 Motivation to do asteroseismology of δ Scuti stars

The occurrence of many mixed acoustic and gravity modes in δ Scuti stars is fortunate because they allow us to study the conditions in deep layers inside these stars. The δ Scuti stars are good laboratories to test stellar opacities, internal rotation rates, rotationally induced element mixing, the extent of convective overshooting from the core and envelope convection. Consequently, the δ Scuti stars also provide an important test whether our understanding of stellar evolution is correct.

Due to historic reasons one distinguishes between two main groups. The high-amplitude δ Scuti stars (short: HADS) with peak-to-peak pulsation amplitudes of the order of 0.3 mag and the low-amplitude δ Scuti stars (LADS) exhibiting amplitudes at the millimag level. While in HADS stars radial pulsation is dominant the LADS stars pulsate in many nonradial modes. Empirical studies indicate that this difference is related to the rotational velocity of these stars (see Fig. 1.5). However, in the recent years it became clear that these two groups are connected. Stars in an intermediate region – slowly rotating stars which exhibit radial modes with large amplitudes along with many nonradial pulsation modes – could be found.

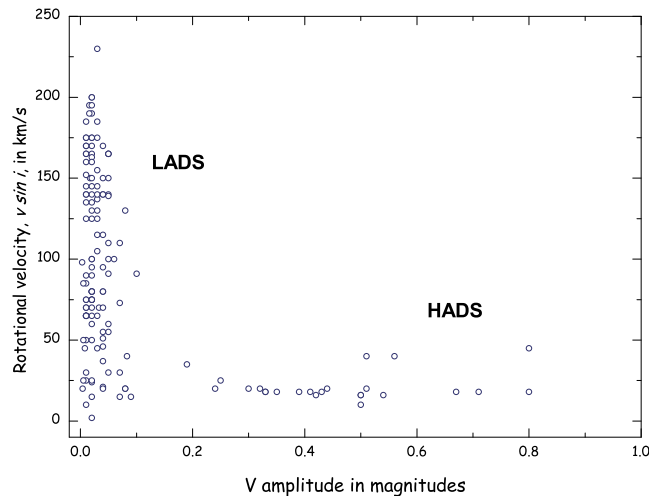


Figure 1.5: Johnson V amplitude versus $v \sin i$. Diagram courtesy of Michel Breger.

For theoretical studies of δ Scuti pulsations these 'intermediate' stars are ideal for the following reasons:

- They pulsate in a sufficient number of radial and nonradial modes. This makes them more interesting for an asteroseismic study than mainly radially oscillating HADS, because each additional frequency provides an independent information about the star.

- They do not rotate as fast as most of the low-amplitude δ Scuti stars. This is an advantage for modeling since the effects of rotation are small enough to be approximated by one-dimensional models. The pulsation theory for fast rotators relying on two-dimensional models is currently being developed (e.g., Roxburgh 2004, 2006; Lignières et al. 2006; Reese et al. 2006; Lovekin & Deupree 2008, ...).
- Slow rotation also reduces uncertainties in mode identification, as will be discussed later.

It is therefore desirable to study a δ Scuti star with such properties. This was the motivation to observe 44 Tau. On the other hand it is interesting to test our asteroseismic methods for a star which may be at the limit of the validity of our methods. The evolved δ Scuti star 4 CVn represents such a challenge.

1.3 δ Scuti stars examined in this work

1.3.1 44 Tauri

44 Tau is one of the stars in the intermediate region between the HADS and LADS stars shown in Figure 1.5. Smith (1982) was the first to determine the projected rotational velocity, $v \sin i$, for 44 Tau. With a value of $v \sin i = 5 \text{ km s}^{-1}$ it was found to be exceptionally low. The low projected rotation rate was later confirmed by other authors (Solano & Fernley 1997; Zima et al. 2007). As discussed in Antoci et al. (2007) such a low value may be explained by a pole-on view (with an intrinsically higher equatorial rotation rate) or by intrinsically slow rotation. Later, Zima et al. (2007) could constrain the inclination angle to $60 \pm 25^\circ$ and determined the equatorial rotation rate to be $3 \pm 2 \text{ km s}^{-1}$. Thus, 44 Tau has approximately a similar rotation rate as the sun.

A detailed review on the history of its discovery and previous observations is given in Antoci et al. (2007). This paper also contains a comprehensive frequency analysis of extensive observations with the Delta Scuti Network from 2000 to 2003. Two additional years of photometry were obtained in the seasons 2004/5 and 2005/6 and analyzed by Breger & Lenz (2008). The final frequency solution consists of 49 frequencies of which 15 are independent. The spectrum of observed independent frequencies is shown in Figure 1.6.

Mean stellar parameters

Asteroseismic analyses require knowledge of the fundamental parameters of the star. The spectral type of 44 Tau is F2 IV. From Strömgren and Geneva photometry the effective temperature can be derived with the common calibrations and by utilizing stellar atmosphere model grids. The Strömgren indices of uvby β photometry from Hauck & Mermilliod (1997) are given in Table 1.1.

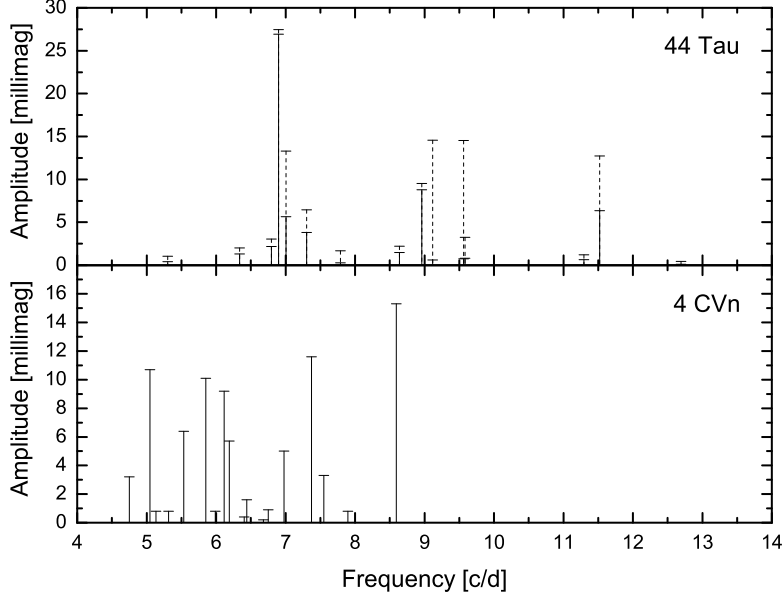


Figure 1.6: Detected independent frequencies in 44 Tau and 4 CVn. For 44 Tau the minimum and maximum annual Strömrgren y amplitudes between 2000 and 2006 are given.

V [mag]	$b - y$ [mag]	m_1 [mag]	c_1 [mag]	β
5.390	0.215	0.170	0.755	2.711
± 0.040	± 0.005	± 0.005	± 0.009	± 0.006

Table 1.1: Measured Strömrgren indices for 44 Tau.

From these values and the well known calibration rules for Strömrgren indices of F stars (Crawford 1975) no significant interstellar reddening was found. The metallicity derived with the calibration given in McNamara & Powell (1985) is close to the solar values.

Based on this metallicity estimate it is possible to utilize the Vienna NEMO grid (New Model Grid of Stellar Atmospheres, Nendwich et al. 2004, Heiter et al. 2002) to derive the effective temperature and the surface gravity as shown in Fig. 1.7. The final estimate for the effective temperature is 6900 ± 100 K. The $\log g$ value is 3.57 ± 0.10 dex. The errors of the grid correspond to the common estimates given in Garrido (2000).

The luminosity can be easily derived from the measured Hipparcos parallax of 16.72 ± 0.93 mas. The given apparent brightness and a bolometric correction of 0.034 mag from Kurucz model atmospheres (Bessell et al. 1998) lead to a luminosity of $\log L/L_{\odot} = 1.305 \pm 0.065$.

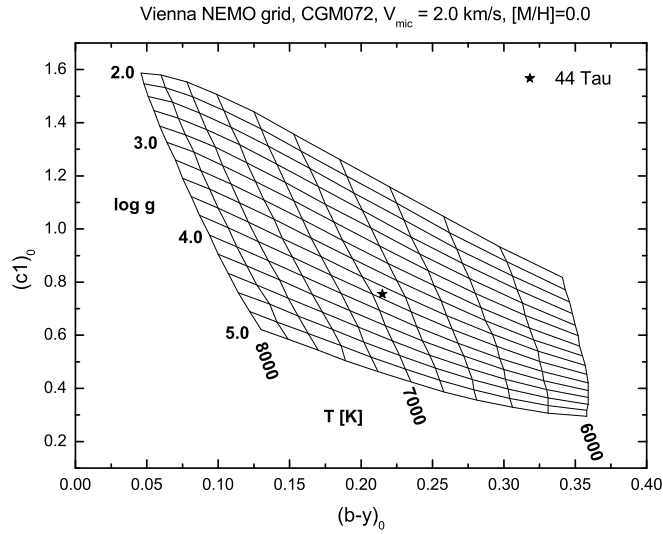


Figure 1.7: Observed position of 44 Tau in the Vienna NEMO grid. A grid with standard metallicity, $[M/H]=0.0$, and a microturbulence velocity of 2 km s^{-1} is shown.

Independent estimates of the stellar fundamental parameters were obtained from spectroscopy. By measuring equivalent widths of the spectral lines of Fe I, Fe II, Ni I and Mn I Zima et al. (2007) determined a microturbulence of $v_{\text{mic}} = 1.85 \text{ km s}^{-1}$. The estimate of this parameter from their spectrum synthesis is slightly lower, 1.30 km s^{-1} . Adopting the photometrically derived T_{eff} and $\log g$ as starting values for their abundance analysis, they iteratively derived an effective temperature of $7000 \pm 200 \text{ K}$ and a $\log g$ of 3.6 ± 0.1 , which agree well with the photometrically derived values. The element abundances were estimated from spectrum synthesis and were found to be close to the solar values. Moreover, they found no indications for a global magnetic field.

1.3.2 FG Virginis

FG Vir is a main sequence δ Scuti star of spectral type A5 V which exhibits moderate rotation. The $v \sin i$ measured by Zima et al. (2006) is $21.6 \pm 0.3 \text{ km s}^{-1}$. With a derived inclination of $19 \pm 5^\circ$ these authors could determine the equatorial rotation velocity to be $66 \pm 16 \text{ km s}^{-1}$. Currently, 79 frequencies are known of which 67 are independent. For the most dominant modes the spherical degrees and azimuthal orders were determined by Breger et al. (1999b), Daszyńska-Daszkiewicz et al. (2005b) and Zima et al. (2006) using various methods.

We do not discuss this star in too much detail because for FG Vir asteroseismic models were already computed by several other authors (see, e.g., Templeton et al. 2001; Guzik et al. 2000; Breger et al. 1999b; Viskum et al. 1998). Therefore, this star was only used to examine specific aspects in the asteroseismic analyses presented in this work. These analyses

rely on the fundamental parameters given in Breger et al. (1999b): $T_{\text{eff}} = 7500 \pm 100$ K, $\log L/L_{\odot} = 1.170 \pm 0.055$ and $\log g = 4.0 \pm 0.1$.

1.3.3 4 Canum Venaticorum

4 CVn is an evolved δ Scuti star of spectral type F3 III-IV. The $v \sin i$ values given in the literature range from 70 to 130 km s⁻¹. The most recent measurements converged to a projected rotational velocity around 120 km s⁻¹, e.g., Glebocki & Stawikowski (2000) with $v \sin i = 115 \pm 10$ km s⁻¹ or Royer et al. (2002) with 128 ± 7 km s⁻¹. Consequently, it cannot be considered to be a slow rotator.

The hitherto most extensive data analysis of 4 CVn was published by Breger et al. (1999a) who analyzed the 1996 photometric data and found 34 frequencies of which 18 are independent frequencies. The corresponding frequency spectrum is shown in the lower panel of Figure 1.6.

Mean stellar parameters

The measured Strömgren indices for 4 CVn from Hauck & Mermilliod (1997) are given in Table 1.2. Due to the lack of a sufficient number of measurements no errorbars are available for this data set. Another source of photometric indices is available from the catalog of measurements in the Geneva photometric system (Rufener 1976).

Johnson V	$b - y$	Strömgren			β	U	V	Geneva			
		m_1	c_1				B1	B2	V1	G	
6.035	0.226	0.178	0.833	2.707	1.570	0.528	0.980	1.390	1.257	1.630	
[mag]	[mag]	[mag]	[mag]		[mag]	[mag]	[mag]	[mag]	[mag]	[mag]	

Table 1.2: Measured photometric indices for 4 CVn.

The photometric calibrations of the Strömgren indices (Crawford 1975) indicate an overabundance of metals in 4 CVn. This was confirmed by the calibrations for the Geneva photometric system (Meléndez & Ramírez 2003) computed with the software TempLogg¹. The results obtained from both systems are in good agreement and the derived metallicity is $[\text{Fe}/\text{H}] = +0.20 \pm 0.15$ dex. Following the assumption that the overabundance also concerns other metals to the same extent as iron, we adopted $[\text{M}/\text{H}] = +0.20$ to determine the effective temperature and surface gravity by means of the NEMO atmosphere grid.

The fundamental parameters derived from photometry and atmosphere models are given in Table 1.3. The measured Hipparcos parallax is 9.75 ± 0.69 mas. With a bolometric correction of -0.080 mag taken from Bessell et al. (1998) the luminosity amounts to $\log L/L_{\odot} = 1.55 \pm 0.070$.

¹<http://www.univie.ac.at/asap/templogg/main.php>

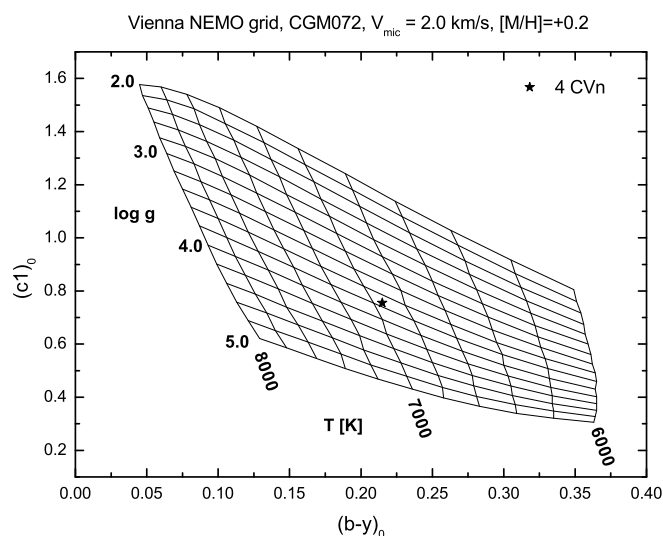


Figure 1.8: Fundamental parameters of 4 CVn derived from Strömgen photometry using the Vienna NEMO model atmosphere grid for $[M/H]=+0.20$.

	T_{eff} [K]	$\log g$	$[Fe/H]$
Strömgen + NEMO	6820 ± 100	3.34 ± 0.10	+0.25
Geneva (TempLogg)	6740 ± 50	3.33 ± 0.16	$+0.13 \pm 0.08$
Summary	6800 ± 150	3.34 ± 0.20	$+0.20 \pm 0.15$

Table 1.3: Derived fundamental parameters of 4 CVn.

The rapid rotation of 4 CVn may affect the photometric indices and, therefore, the derived values for effective temperature and luminosity. As shown by Pérez Hernández et al. (1999) the $\log L$ value generally depends on the inclination angle, i . In the case of pole-on view the value may increase up to 25%, for equator-on view a decrease of 20% is possible. Moreover, the effective temperature is also affected by projection effects. Unfortunately, the inclination angle of 4 CVn could not yet be determined. To account for these effects the error bars were increased correspondingly to obtain the final mean values of luminosity and effective temperature.

1.3.4 Position of 4 CVn, FG Vir and 44 Tau in the HR diagram

The positions of 4 CVn, 44 Tau and FG Vir in the HR diagram are shown in Figure 1.9 along with the edges of the instability strip. As can be seen all three stars are not too close

to the cold border of the instability strip where the effects of envelope convection on the instability of the modes become important.

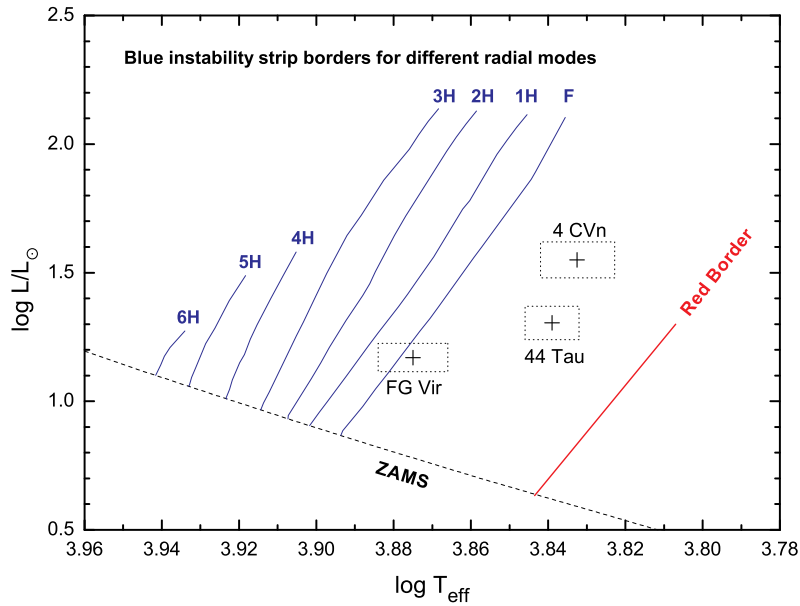


Figure 1.9: Observed positions of 44 Tau, FG Vir and 4 CVn in the Hertzsprung-Russell diagram. Blue edges of the instability strip for various radial overtones were computed with OPAL opacities, the GN93 element mixture, and a standard chemical composition with $X=0.70$, $Z=0.02$. The theoretical red edge for the radial fundamental mode was taken from Dupret et al. (2004).

Chapter 2

The computational tools to study δ Scuti stars

The computer codes used in this work were provided by asteroseismologists from the Copernicus Center in Warsaw (Poland). In the next sections a brief description of these up-to-date codes for the computation of stellar evolution and pulsation is given.

2.1 Warsaw - New Jersey stellar evolution code

The original version of this stellar evolution code was developed by B. Paczyński, R. Sienkiewicz and M. Kozłowski. The code was presented in Paczyński (1969) and some technical details are also discussed in later papers (Paczyński 1970a,b,c).

The stellar structure equations are solved with a Henyey type method (Henyey et al. 1964). Starting from a chemically homogeneous zero-age main sequence (ZAMS) model the evolution of the stellar model is computed adopting the nuclear reaction rates given in Bahcall et al. (1995). The boundary of the convective core is determined by evaluating the Schwarzschild stability criterion. Inside the convective core an adiabatic temperature gradient is used and element mixture is allowed. At the boundary of the core, convective overshooting can be assumed. The size of the overshoot layer is commonly defined by the quantity α_{ov} which is measured in units of the pressure scale height at the boundary of the convective core. In the traditional approach the adiabatic temperature gradient is used in the overshoot layer while element mixing is ignored.

Additionally a new two-parametric description of overshooting from the convective core was applied. This new approach allows to consider different profiles of the hydrogen abundance inside the partly mixed region (the overshoot layer) just above the convective core. The same approach was used by Dziembowski & Pamyatnykh (2008) in an asteroseismic study of the two β Cephei stars ν Eri and 12 Lac. The first parameter, α_{ov} , again, defines the overshooting distance above the convective core. The second parameter, w , adjusts

the profile of the hydrogen abundance between the convective core and the upper boundary of the overshooting region. Thus it characterizes the efficiency of element mixing in the overshooting region. The hydrogen profile, X , is defined as a function of fractional mass, q :

$$X = X_c + (q - q_c)^w [a + b(q - q_c)]. \quad (2.1)$$

The coefficients a and b in this equation are determined from w , α_{ov} and the requirement of a smooth transition of the hydrogen abundance (and its first derivative) at the boundaries of the overshoot layer. An infinitely high value of w corresponds to the traditional treatment for overshooting.

δ Scuti stars exhibit convection zones in the envelope. Convection takes place in the layers where the partial ionization of He II and H/He I occurs. In these outer layers the temperature gradient cannot be approximated as adiabatic because of radiative losses. To determine the temperature gradient in these regions a standard mixing-length theory (MLT, Böhm-Vitense 1958) of convection is used in the stellar evolution code.

Rotation is an important effect in stellar modeling. In the code, rotation is implemented using a rigid body rotation law and it is assumed that the star conserves its total angular momentum during its evolution. Stellar rotation reduces the effective gravity by the spherically averaged contribution of the centrifugal acceleration. Rotationally induced mixing is ignored in the code.

Moreover, the code ignores diffusion (i.e., the segregation of elements due to the slightly different impact of gravity and radiative pressure on atoms of different elements). Mass loss from the stellar surface is neglected as well.

2.2 Dziembowski's pulsation code

The eigenfrequencies of a stellar equilibrium model are computed with a modern version of Dziembowski's pulsation code (Dziembowski 1977b, 1971). This code relies on the linear theory of pulsation. For δ Scuti stars linear models are justified because the relative radius variations are sufficiently small even for high-amplitude δ Scuti stars. Linear pulsation models are well suited to compute the eigenfrequencies of stellar oscillations, but they cannot predict the amplitudes of the pulsation modes. This task remains to be solved by nonlinear pulsation theory as will be briefly discussed in Chapter 6.

In the envelope of the stellar model the full nonadiabatic equations are solved. This is necessary because the thermal time scale in the subphotospheric layers is comparable to the oscillation period. For central regions the quasi-adiabatic approximation is used when justified (see Dziembowski 1977b, for a more detailed description).

In the code the assumption of frozen convective flux during the pulsation cycle is adopted. This approximation may not be realistic for δ Scuti stars close to the red edge of the instability strip and could introduce uncertainties in mode identification or linear stability surveys. We will discuss this matter in more detail in the following chapters.

To ensure a high numerical accuracy of the frequencies integral expressions of the eigenfrequencies are evaluated and additional mesh points are included if necessary to improve the resolution of the grid. The achieved relative accuracy of the period is 10^{-4} .

2.3 Treatment of stellar rotation

The modification of the stellar structure due to rotation naturally also influences the pulsation frequencies. Rotation increases the star's volume, leading to a lower density and a change in the size of the resonant cavities. Consequently, the frequencies of acoustic modes are decreased by rotation.

Moreover, rotation lifts the degeneracy between different m -values. A very nice physical picture of this effect is given in Cox (1984). The separation between frequencies of unlike azimuthal order increases with the rotation rate. Since mixed modes are sensitive to different layers in the star the observed frequencies of rotationally split multiplets provide information about the internal rotation rate. The rotation rate, Ω , can then be inferred with the simple equation

$$\nu \approx \nu_0 + m\Omega(1 - C). \quad (2.2)$$

where ν_0 is the unperturbed frequency, C describes the Ledoux constant and m denotes the azimuthal order. This simple equation allows to estimate the equatorial rotational velocity for a slowly rotating star if at least two components of a multiplet are observed. As shown by Goupil et al. (2000) the limit of the validity of this equation is at a rotation rate of approximately 50 km s^{-1} . At higher rotation rates the rotational splittings are more asymmetric due to higher order effects of the Coriolis and centrifugal force. Therefore, the perturbation approach applied in the pulsation codes used in this work takes into account the effects of rotation up to second order following Dziembowski & Goode (1992).

Certainly, the second order theory also has its limitations. Since it relies on the perturbation approach it can only be applied to rotating stars which still can be approximated as spherically symmetric, and when the rotation rate Ω is small against the pulsation frequency. Rapid rotation forces a departure from the spherically symmetric geometry due to the centrifugal force. The oblateness of a star is described by the parameter ϵ ,

$$\epsilon = 1 - R_p/R_e \quad (2.3)$$

where R_p and R_e are the stellar radius at the pole and the equator, respectively. Fast rotation may also lead to structural instability of the star. The critical rotation rate, the so-called Keplerian break-up rate, Ω_K , is

$$\Omega_K = \sqrt{\frac{GM}{R_e^3}}. \quad (2.4)$$

Recently, Lignières et al. (2006) and Reese et al. (2006) studied the effects of rotation on acoustic modes by numerically solving the two-dimensional eigenvalue problem for a

simple model of a star. They found that if the rotation exceeds a value of approximately $\Omega/\Omega_K \approx 0.10$ the differences between their method and the second order perturbative approximation become evident (see Figure 12 in Lignières et al. 2006).

A $2.0 M_\odot$ δ Scuti model with a rotation rate of 50 km s^{-1} at the ZAMS has a Ω/Ω_K of 0.10. As shown in Figure 2.1, Ω/Ω_K increases only slightly during the main sequence phase but reaches a value of 0.13 in the post-main sequence phase. Consequently, such a model may be at the limit of the validity of the perturbative approach used in this work. These results also illustrate that Ω/Ω_K has to be checked in particular for post-main sequence models of δ Scuti stars. At $\Omega/\Omega_K \approx 0.24$ Lignières et al. (2006) found that the deviations between the frequencies predicted by their two-dimensional method and the perturbation approach is as high as 0.95 cd^{-1} . This corresponds to a δ Scuti model with a rotation rate of 100 km s^{-1} . Thus for one of the stars examined in this study, 4 CVn, which exhibits a $v \sin i$ of approximately 120 km s^{-1} , an accurate prediction of individual frequencies is not possible with the codes applied in this work.

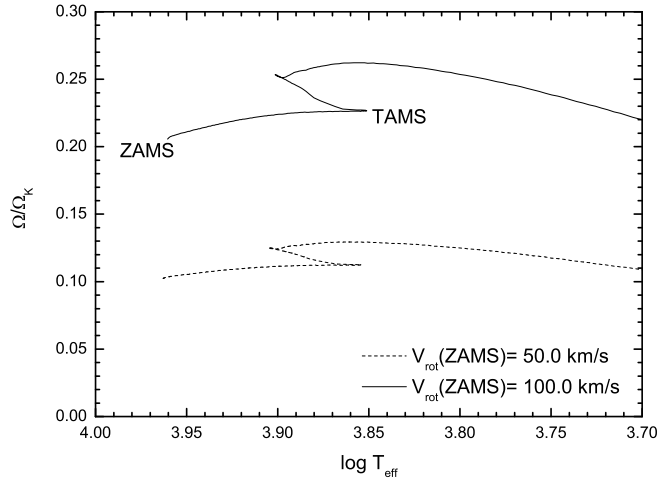


Figure 2.1: Evolution of the fraction Ω/Ω_K for a $2.0 M_\odot$ model with an initial rotation rate of 50 and 100 km s^{-1} .

2.4 Input data for the models

In stars energy is transported through radiation, convection and conduction. To model the radiation transfer inside a star the opacity in the different layers in the star is needed. In stellar models Rosseland's mean coefficient of absorption is commonly used:

$$\frac{1}{\kappa_R} = \frac{\int_0^\infty d\nu \frac{1}{\kappa(\nu)} \frac{dB_\nu}{dT}}{\int_0^\infty d\nu \frac{dB_\nu}{dT}} \quad (2.5)$$

As shown in this equation the opacity is obtained by computing a weighted average of the individual monochromatic opacity, $\kappa(\nu)$, of different chemical elements over all wavelengths. Consequently, to compute stellar opacities a chemical composition has to be assumed for the stellar model.

2.4.1 Element abundance mixtures for stellar models

For the computation of a stellar model a specific chemical composition, i.e., an abundance distribution of various elements, has to be adopted. The element mixture of a star reflects the abundances of the cloud in which the star was formed. This original element mixture is almost preserved in the stellar envelope. In the recent years photospheric abundances were measured for several δ Scuti stars (e.g., Fossati et al. 2008; Zima et al. 2007; Mittermayer & Weiss 2003, ...). These results showed that the examined abundance patterns of normal δ Scuti stars are similar to those derived for the solar system.

The abundances derived for our solar neighbourhood are much more accurately measured than those of other stars. It is often difficult to assess the abundance of important elements in distant stars. Therefore, the solar element mixture is also used for the computation of models of other stars. The chemical composition of a star is usually given in certain mass fractions, X for hydrogen, Y for helium and Z for metals. The term metals is used in the astronomical sense, denoting all elements with a higher atomic number than helium. For stars in which the metallicity is observed to be higher or lower than for the sun, the measured solar abundance mixture of metals is scaled accordingly to obtain the requested metal mass fraction, Z . This means that the relative abundances between the different metals remain unchanged.

The measured values of the solar element abundances are subject to changes and improvements because they are derived based on a theoretical atmosphere model. Thus an improvement to the atmosphere model is also reflected in the values of the abundances. The most commonly used solar element mixtures for stellar modeling are given in Table 2.1.

Abbreviation	Reference	Mass fractions for solar composition
GN93	Grevesse & Noels (1993)	$X=0.70, Z=0.02$
A04	Asplund et al. (2005)	$X=0.7392, Z=0.0122$

Table 2.1: Solar element mixtures.

The initial abundances in the solar system can be derived from meteorites and the analysis of the photospheric spectrum of the sun. Grevesse & Noels (1993) determined the solar photospheric abundances with a one-dimensional hydrostatic atmosphere model of the sun and found a good agreement with the results derived from meteoric data. Their proposed element mixture (GN93) combines the results of both sources of abundance data. This mixture has been the standard element mixture in stellar modeling for a long time.

Asplund et al. (2004) derived the solar abundances by means of a three-dimensional hydrodynamical model of the solar atmosphere using the most recent atomic physics data for atoms and molecules. Contrary to one-dimensional models the new models are successful in reproducing the shape of photospheric spectral lines and other observable parameters without assuming any free parameter (such as the microturbulence velocity, v_{mic}). The new results by Asplund et al. (2004) and Asplund et al. (2005) for the solar abundances led to a significant downward revision of the metal mass fraction. The element abundances of CNO and Ne were decreased by 40% and Fe by 20%. Since iron group elements have higher abundances in A04, a smaller metal mass fraction Z is needed to obtain the same effect. The mass fraction of heavy elements was revised to $Z = 0.0125$. This is much lower than the metal mass fraction suggested by Grevesse & Noels (1993).

This revision caused a serious problem for the theoretical models of the sun. The difference between the sound speed in the solar model and the sound speed derived from helioseismic inversions increased. The effect of the new abundances on the stellar models is mainly caused by the corresponding change of opacity. Since the new abundances have become available, several approaches to compensate for the effects of the new solar composition have been suggested. Possible solutions range from a significant increase of the abundance of elements which are difficult to assess (such as Neon) to the suggestion that opacity data still lack the contribution of a large number of elements of low abundance which could have a significant effect on the opacity.

Christensen-Dalsgaard et al. (2009) derived an intrinsic opacity modification that would be required to reproduce the sound speed structure of their solar model with the new heavy-element composition. They found that the opacity has to be modified by 30 % at the base of the solar convection zone to solve the problem. However, the question arises whether such a change is justified.

In another paper Christensen-Dalsgaard (2009) made an asymptotic analysis of the most recent data set of observed solar frequencies and found that the solar age derived with the A04 composition is inconsistent with the age derived from meteoritic analyses, while the GN93 composition is in sufficient agreement.

Obviously, the new solar abundances are still subject to discussions. In this work both element mixtures are adopted and the differences in the asteroseismic results are compared.

2.4.2 Equation of state

For different values of density and temperature the equation of state delivers the corresponding pressure, ionization degrees and thermodynamic quantities that are required to determine the stellar structure. The equation of state includes the most abundant elements in stars and is evaluated for the desired chemical composition.

A general review of various equations of states and their area of application is given in Däppen & Guzik (2000). In our work the Lawrence Livermore National Laboratory equation of state (Rogers et al. 1996) is used in its latest version (OPAL EOS2005). This equation

of state is commonly used for asteroseismic studies and is valid for stars with a mass larger than $0.8 M_{\odot}$.

Another popular equation of state which is mainly used for helioseismology is the CEFF equation of state (Christensen-Dalsgaard & Däppen 1992). Contrary to the OPAL EOS, which relies on pre-tabulated data, the CEFF EOS is an analytic equation of state. The main disadvantage of an analytic equation of state is the extremely time-consuming computation. In section 4.2.4 we briefly examine the influence of the choice of the equation of state on an asteroseismic model of 44 Tau.

2.4.3 Opacity data

Based on the chemical composition, the density and temperature of a medium, the ionization equilibrium concentrations and level populations are computed by the equation of state. These data are important to evaluate the Rosseland mean opacities. Radiative opacities were calculated and made available by two independent teams, OPAL and OP. Corresponding references and online data bases are listed in Table 2.2.

Source	Reference and link to online-database
OPAL	Iglesias & Rogers (1996) http://physci.llnl.gov/Research/OPAL/
OP (Opacity Project)	Badnell et al. (2005), Seaton (2005) http://cdsweb.u-strasbg.fr/topbase/op.html

Table 2.2: Sources of opacity data.

The references in the table are given for the most recently published updates of opacity data. The computation of monochromatic opacity tables is very complex and requires sophisticated methods and up-to-date atomic data. Both groups have a slightly different approach to compute the radiative opacities (following the 'chemical' vs. the 'physical picture', see e.g., Seaton & Badnell 2004, for details).

The comparison of Rosseland mean opacities computed from OPAL and OP tables by Badnell et al. (2005) shows an agreement within 5 to 10%. With the OP opacities the metal opacity bump is predicted at a slightly higher temperature and, therefore, deeper in the star than with OPAL data. While this is not important for the δ Scuti stars it produces more efficient driving for hybrid SPB and β Cephei pulsators which is in better agreement with observations (Miglio et al. 2007).

Opacity data have an important impact in modeling the pulsations of stars. Incomplete atomic data and uncertainties in opacity calculations may lead to differences in asteroseismic models, which may be used to pinpoint potential problems with opacity data at certain temperatures and densities.

Conductive opacities

At high densities such as the central region in δ Scuti stars, heat conduction from electrons has to be taken into account. In our code these conductive opacities are evaluated with the formulae of Yakovlev & Urpin (1980).

Low-temperature opacities

The OPAL and OP opacities do not include the contribution of molecules and dust to the radiative opacity. Their effect becomes increasingly important with decreasing temperature. In δ Scuti stars the layers close to the surface are cold enough to have a small opacity contribution by molecules.

Such molecular and grain opacities have been provided by Alexander & Ferguson (1994) (hereafter AF94). A decade later, Ferguson et al. (2005) published updated low-temperature opacities for a more extended temperature range. The new opacities were computed based on an up-to-date list of molecular and atomic lines and grain species.

As stated by Iglesias & Rogers (1996) the good agreement between atomic line opacities and the molecular AF94 opacities allows to combine these tables for the use in stellar modeling. As part of this work the Ferguson et al. (2005) low-temperature opacities were implemented into our codes and the implications on the models were tested.

2.4.4 Implementation of updated low-temperature opacities into the codes

The Rosseland mean opacities are commonly tabulated as a function of logarithms of temperature and the density parameter $R=\rho/(10^{-6} T)^3$ for a set of different mass fractions of X and Z. For the use in our codes a two-dimensional cubic spline formula is applied to transform the original opacity grid into tables for κ adopting a grid denser than the original grid. The opacity derivatives are computed from the same spline formula to ensure consistency with the opacity. This approach allows for a fast linear interpolation for required T and ρ in the tables during evolutionary computations.

Opacity database	Range in $\log T$	Step size in $\log T$
OPAL	8.70 - 3.75	0.05
AF94	4.10 - 3.00	0.05
F05	4.50 - 2.70	0.05 (0.01 between $\log T=3.5$ and 2.9)

Table 2.3: Temperature ranges of opacity data.

The upper boundary of the temperature range for the new Ferguson et al. (2005) opacities has been extended to 30000 K in contrast to 12000 K of AF94 (see Table 2.3). The preparation of a combined table of atomic line opacities (OPAL, OP) and molecular

data (AF94, F05) is done prior to the transformation to a denser grid. First the agreement of the different opacities in the overlapping temperature region has to be checked. This is done in Figure 2.2.

The large differences between F05 and AF94 at temperatures below $\log T=3.2$ are due to more complete computations of opacities (e.g., the inclusion of more grain species in the EOS). Details are discussed in Ferguson et al. (2005). However, this temperature regime is not negligible for δ Scuti stars. For the AF94 opacities a good fit to the radiative opacities is possible at $\log T = 3.95$. At this temperature the mean relative differences in R between both tables is around 2% for a hydrogen mass fraction $X > 0$. For the new F05 opacities a fit of similar quality is achieved and the same temperature was used to fit the two opacity data sets.

The effect of the implementation of new low-temperature data on the final opacities in a stellar model is small, as shown in Figure 2.3 for a δ Scuti model with $2.1 M_{\odot}$ and an effective temperature of 6800 K. Therefore, the impact of this change on evolutionary models is almost negligible. However, the implementation of updated low-temperature opacities is important for the accurate computation of theoretical amplitude ratios and phase differences between different photometric passbands. As will be discussed in more detail in the next chapter, these quantities are indicators of the spherical degree of a mode. Figure 2.4 examines the impact of the choice of molecular opacities on the predicted amplitude ratios and phase differences between the Strömgren v and y passband for the same stellar model as used in Figure 2.3. As can be seen, the differences increase with higher spherical degrees. The deviations are expected to be largest for acoustic modes with high spherical degrees, because the propagation zones of these modes do not extend into deep layers of the star and are, therefore, more sensitive to the choice of low-temperature opacities which have their main contribution in layers close to the surface. The following chapter will discuss the theoretical background of this diagram and its diagnostic value for the important task of mode identification.

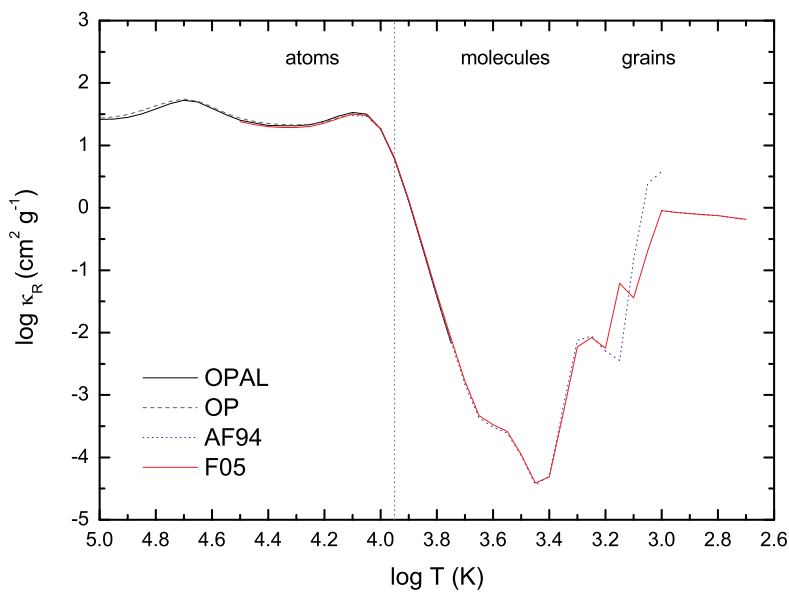
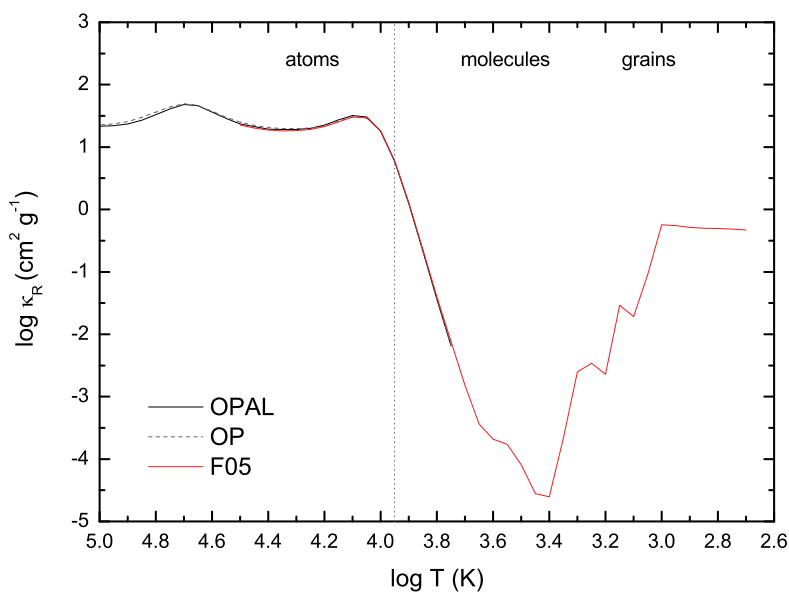
(a) GN93 element mixture with $X=0.70$, $Z=0.02$ (b) A04 element mixture with $X=0.70$, $Z=0.01$

Figure 2.2: Comparison of tabulated Rosseland mean opacities at low temperatures for $\log R=-3$. The dotted vertical line marks the temperature ($\log T=3.95$) where the OPAL and AF94 opacities are fit together. The comparison is made for both solar element mixtures.

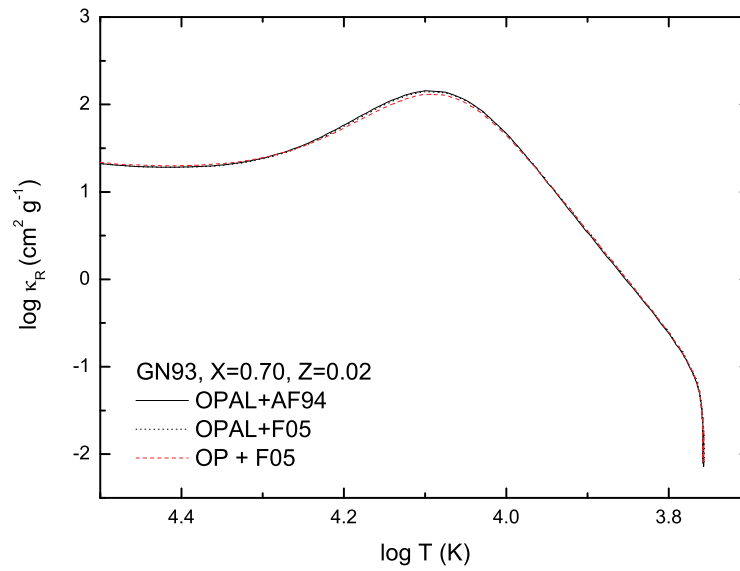


Figure 2.3: Comparison of Rosselland mean opacity, κ_R , in models constructed with different combinations of atomic and molecular opacities.

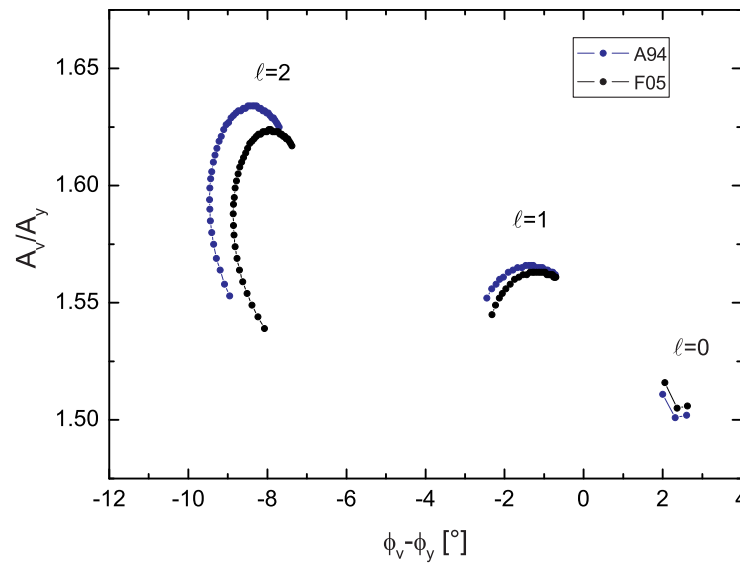


Figure 2.4: Influence of the choice of low-temperature opacities for an OPAL model with the fundamental parameters of 4 CVn and adopting $\alpha_{\text{MLT}}=0.2$.

Chapter 3

Mode identification and its diagnostic power

3.1 Mode identification techniques

The assignment of correct angular numbers (ℓ, m) to an observed pulsation mode is an essential step for successful asteroseismology. How can we infer the surface geometry of a pulsation mode? We only have a limited amount of information in the emitted light of a star. Stellar pulsation causes the brightness of a star to vary due to the change of the surface area and the variation of the temperature. On the other hand, by means of radial velocity measurements we can determine the radius variation of a star, which can be compared to the light curve.

For an adiabatic pulsation the luminosity is highest in the phase of minimum radius (i.e., maximum compression). In reality, for stars in the classical Cepheid instability strip the maximum brightness is observed close to maximum velocity. Consequently, there is a phase lag of the luminosity which corresponds to 90° which means that nonadiabatic effects are important. As shown by Castor (1968) the phase lag mainly forms in the ionization zone of neutral hydrogen. During the compression phase energy is temporarily stored due to ionization and released again in the expansion phase. As stated by Castor (1968) the hydrogen ionization zone “acts like a low-pass filter” because matter is only ionized by photons with a certain amount of energy. An illustrative representation of the formation of the theoretical phase-lag between intensity and velocity curves throughout the different layers in a star can be found in Baker & Kippenhahn (1965).

There is not only a phase-lag between the luminosity and radial velocity curve. The same effect leads to an increasing phase retardation of the light emission to longer wavelengths. Since this effect depends on the spherical degree of a mode the observed small phase differences in different passbands can be used for mode identification. For example radial modes in δ Scuti stars exhibit a small positive phase difference between the Strömgen v and y passband, while for nonradial modes the phase differences are negative.

Another important factor which is perturbed by pulsation is limb-darkening. In the central part of a stellar disc more light is emitted than near the limb, because we look into different layers of the star. Since limb-darkening depends on temperature and gravity the limb-darkening coefficients also change during a pulsation cycle. The strength of these effects depends on the spherical degree of the mode, i.e., the number of node lines on the surface.

Dziembowski (1977a) derived formulae for the periodic flux and radial velocity variations caused by nonradial pulsation based on the linear oscillation theory. He concluded that the Baade-Wesselink relation can be used to derive the ℓ values of modes if the stellar radius is known. The formula was derived for a non-rotating star. It was found by Gautschy & Saio (1996) that this approximation is justified for β Cephei and δ Scuti stars. For g mode pulsators such as SPB or γ Dor stars this theory is not valid because the Coriolis force becomes important. For these types of pulsators Townsend (2003) and Daszynska-Daszkiwicz et al. (2007) derived a more sophisticated approach to determine the spherical degrees.

The derivation given in Dziembowski (1977a) was reformulated by other authors (Balona & Stobie 1979; Watson 1988; Garrido 2000) and lead to amplitude-phase diagnostic techniques to determine the spherical degree using multicolor photometry. In this study the theoretical mode positions are computed following Daszyńska-Daszkiwicz et al. (2003). Balona & Evers (1999) noted that the theoretical mode positions in a diagnostic diagram are sensitive to the modeling of the outer envelope, in particular to the efficiency of convection in the partial ionization zones in the envelope. From the results of their study, Daszyńska-Daszkiwicz et al. (2003) concluded that the amplitude ratios and phase differences mainly depend on the value of α in the hydrogen ionization zone. The mixing-length parameter in the He II ionization zone has only a little effect. Consequently, deviations between observed and theoretical amplitude ratios and phase differences can be used to pinpoint problems in the modeling of the neutral hydrogen ionization zone.

Our computations rely on the mixing-length theory of convection and assume the frozen flux approximation for the pulsation-convection interaction. This assumption may not be appropriate for δ Scuti stars close to the red edge of the instability strip and result in uncertainties in mode identification. Montalbán & Dupret (2007) investigated the effect of different treatments of convection on the predicted phase differences and amplitudes. While the use of a time-dependent theory of convection was shown to be important for some cases, they stated that for frequencies close to that of the fundamental mode the influence of the treatment of convection on the determination of mode degree is small.

The amplitude ratios and phase differences between different passbands are independent of the intrinsic mode amplitudes, azimuthal order and inclination angle. The main problem for δ Scuti stars is that we cannot use regular frequency patterns such as the so-called large frequency spacing which is used for the identification of spherical degrees in the sun. Moreover, the majority of δ Scuti stars rotate much faster than the sun and the effects of rotation, such as the larger separation of the rotational splitting of the modes, complicate the picture. A major effort was made to develop new methods for mode identification

especially in the spectroscopic field. Currently, the most important spectroscopic mode identification techniques are the moment method (Balona 1986; Aerts 1996) and the Fourier Parameter Fit method (Zima et al. 2006). Both methods investigate the intensity variations in the line profiles caused by pulsation to model the surface velocity field and then extract the most likely azimuthal orders and spherical degrees. Their stronger sensitivity to azimuthal orders make these techniques complementary to photometric mode identification. These methods also have a higher potential to detect modes of spherical degrees higher than those accessible by earth-bound photometry.

On the other hand the radial velocity data (the first moment of the line profile variation) are affected by disc averaging effects similar to those in photometric passbands. Consequently, they are more sensitive to low degree modes than the latter methods. A powerful method to determine the spherical degree of low degree pulsation modes was presented by Daszyńska-Daszkiewicz et al. (2005b). These authors combines photometric and radial velocity data to infer the ℓ value of modes by means of a statistical test. Since we also apply this technique in our work we will discuss the theoretical background of this method in the next section.

3.1.1 A least-squares approach for three passbands (the DD-method)

In the preceding section we noted that the positions of modes in the photometric diagnostic diagrams depend on the efficiency of convection. The sensitivity for convection enters through the complex parameter f which is the ratio of the relative luminosity variation to the relative radial displacement of the surface. Daszyńska-Daszkiewicz et al. (2003) proposed a statistical approach based on three passbands to simultaneously determine ℓ and f by means of a χ^2 test

We will briefly outline their method. In an oscillating stellar photosphere the radius variation is given by

$$\frac{\delta r(R, \phi, \theta)}{R} = \text{Re}[\varepsilon Y_\ell^m e^{-i\omega t}] \quad (3.1)$$

and the variation of the bolometric flux by

$$\frac{\delta F_{\text{bol}}}{F_{\text{bol}}} = \text{Re}[f Y_\ell^m e^{-i\omega t}] \quad (3.2)$$

where the complex parameter ε describes the amplitude and phase of a mode. The spherical harmonic, Y_ℓ^m , is defined as

$$Y_\ell^m(\theta, \phi) = (-1)^{\frac{m+|m|}{2}} \sqrt{\frac{(2\ell+1)(\ell-|m|)}{(\ell+|m|)!}} P_\ell^{|m|}(\cos \theta) e^{im\phi} \quad (3.3)$$

where P_ℓ is the Legendre polynomial. Note that a non-standard normalization is adopted. For δ Scuti stars the approximation of a static plane-parallel atmosphere is valid. Relying on this approximation ε and f can be regarded as constant. Following Daszyńska-Daszkiewicz

et al. (2002, 2003) the complex amplitude of flux variation at a given passband λ can be written as

$$A^\lambda = D_\ell^\lambda(\tilde{\varepsilon}f) + E_\ell^\lambda(\tilde{\varepsilon}). \quad (3.4)$$

where

$$\tilde{\varepsilon} = \varepsilon Y_\ell^m(i, 0) \quad (3.5)$$

and

$$D_\ell^\lambda \equiv b_\ell^\lambda \frac{1}{4} \frac{\partial \log(F_\lambda |b_\ell^\lambda|)}{\partial \log T_{\text{eff}}} \quad (3.6)$$

$$E_\ell^\lambda \equiv b_\ell^\lambda \left[(2 + \ell)(1 - \ell) - \left(\frac{\omega^2 R^3}{GM} + 2 \right) \frac{\partial \log(F_\lambda |b_\ell^\lambda|)}{\partial \log g} \right] \quad (3.7)$$

b_ℓ^λ is the disc averaging factor which is defined as

$$b_\ell^\lambda = \int_0^1 h_\lambda(\mu) \mu P_\ell(\mu) d\mu \quad (3.8)$$

with the limb darkening law h_λ . The other quantities have their usual meaning. In this study the limb darkening coefficients of Claret (2000) are used. The partial flux derivatives, $F_\lambda |b_\ell^\lambda|$, are computed from the Vienna NEMO atmosphere models (Heiter et al. 2002; Nendwich et al. 2004).

The system of three complex linear equations given in Equation 3.4 contains the two unknown quantities f and $\tilde{\varepsilon}$. If observations in three passbands are available, it is possible to determine the quantities ℓ and f simultaneously by means of a least-squares technique using trial values for ℓ . Unfortunately most of the photometric studies only utilize two filters, e.g., Strömgren v and y . However, in the recent years spectroscopic measurements gained importance due to the development of new mode identification techniques. Consequently, radial velocity data have become available. Instead of a third photometric passband, the radial velocity data can be related to $\tilde{\varepsilon}$ through

$$i\omega R \left(u_\ell^\lambda + \frac{GMv_\ell^\lambda}{R^3\omega^2} \right) \tilde{\varepsilon} = A_{RV}^\lambda \quad (3.9)$$

The coefficients u_ℓ^λ and v_ℓ^λ and are given in Dziembowski (1977) for gray atmospheres. This method which utilizes two photometric passbands and radial velocity data was used by Daszyńska-Daszkiewicz et al. (2005b) to determine the spherical degree of the modes in FG Vir. This was the first application of this method to a δ Scuti star. Due to the different nature of radial velocity and photometric data the DD-method provides a much stronger constraint on the identification of ℓ compared to results solely based on multicolor photometric data. For example, Daszyńska-Daszkiewicz et al. (2005a) showed that for the β Cephei star δ Ceti the method did not lead to a clear decision between several even ℓ values from the χ^2 results obtained from the pure photometric approach. Using the radial velocity data a clear discrimination was possible.

The effects of rotation are not included in the equations 3.4 and 3.9 but they represent a good approximation for $\Omega/\omega \ll 1$.

Issues to take care of when dealing with observational data

For a correct application of the DD-method one has to check the time-dependence of the observational frequency solution. Observations are usually analyzed by fitting sinusoidal sine curves to the data adopting the equation $A_0 \sin(\omega t + \phi)$. Contrary, in theory $|A|e^{i\phi}e^{-i\omega t}$ is widely used. The conversion between theory and observations can be made with the simple relation $\phi_{\text{th}} = \frac{\pi}{2} - \phi_{\text{obs}}$.

3.2 Application to 44 Tau

In the following sections the spherical degrees of the modes observed in 44 Tau will be determined by means of the photometric amplitude-phase analysis and the DD-method utilizing two photometric passbands and radial velocity data.

3.2.1 Photometric mode identification

Observational amplitude ratios and phase differences

The data used in this study were obtained during several seasons. Table 3.1 below lists the amount of Strömgren v photometry that has been gathered by the Delta Scuti Network.

Season	Observations	Observatories
2000/1	259 h during 42 nights	APT 0.75m, OSN 0.90m
2001/2	143 h during 31 nights	APT 0.75m
2002/3	70 h during 17 nights	APT 0.75m
2004/5	143 h during 26 nights	APT 0.75m
2005/6	173 h during 26 nights	APT 0.75m

Table 3.1: Observing log 2000-2006. APT denotes the Automatic Photoelectric Telescope in Arizona (USA) and OSN the Observatorio de Sierra Nevada (Spain).

The frequency analysis of the total data set was published in Breger & Lenz (2008). Michel Breger extracted a total number of 49 significant frequencies, of which 15 are independent. The remaining 34 frequencies are combinations or harmonics of these frequencies. Table 3.2 lists the frequencies and amplitudes in the Strömgren v and y passband according to the latest frequency solution by Breger & Lenz (2008).

For f_{12} to f_{15} only the amplitudes of the combined y and scaled v data are given. Due to possible phase shifts between the different years the amplitude ratios and phase differences between the v and y filter were determined for each season separately. The results are listed in Table 3.3 and 3.4.

The amplitude ratio and phase difference of f_6 is affected by the near zero amplitude in the season 2004/5. The uncertainties of some of the low-amplitude modes are also very high. From these single year solutions one can find a mean solution by weighting the annual solution with the corresponding SNR of each frequency. This step ensures that observing seasons with more data and lower noise contribute to the average value with a higher weight than shorter observing runs. Table 3.5 lists the final mean values for the amplitude ratio, A_v/A_y , and the phase difference, $\phi_v - \phi_y$ of all observed modes. Fig. 3.1 presents these results in a corresponding diagram with labels for each mode.

ID	Frequency cd^{-1}	Amplitude [mmag]									
		2000/1		2001/2		2002/3		2004/5		2005/6	
		ν	y	ν	y	ν	y	ν	y	ν	y
f_1	6.8980	39.64	27.37	39.41	27.46	39.32	26.94	39.23	27.42	39.53	27.40
f_2	7.0060	19.11	13.30	16.80	11.86	13.86	9.19	10.00	6.92	8.29	5.64
f_3	9.1174	16.76	11.48	21.09	14.56	17.62	11.91	4.87	3.37	0.81	0.61
f_4	11.5196	18.16	12.73	16.53	11.65	16.72	11.70	10.25	7.21	8.78	6.36
f_5	8.9606	13.81	9.53	13.75	9.24	12.82	8.78	13.58	9.49	13.77	9.51
f_6	9.5611	10.68	7.28	18.95	12.87	21.31*	14.54*	0.61	0.75	10.45	7.07
$f_7 \nu$	7.3031	6.67	4.54	6.11	3.98	7.43	4.91	9.00	6.45	5.71	3.82
$f_8 \nu$	6.7955	3.16	2.31	4.46	3.02	2.55	2.17	3.56	2.37	4.00	3.05
$f_9 \nu$	9.5828	2.08	1.34	4.04	2.36	4.70*	3.23*	2.13	1.47	0.93	0.79
f_{10}	6.3390	2.34	1.70	2.15	1.61	3.34	1.85	1.93	1.30	2.74	2.00
f_{11}	8.6391	2.17	1.60	1.89	1.46	2.34	1.66	3.24	2.19	2.91	2.00
f_{12}	11.2947		0.62		1.00		1.21		1.11		1.19
f_{13}	12.6915		0.43		0.32		0.41		0.09		0.13
f_{14}	5.3047		0.59		0.73		1.04		0.75		0.41
f_{15}	7.7897		0.50		0.77		1.67		0.28		1.03

Table 3.2: Frequencies and amplitudes in the Strömgren ν and y filters. Values taken from Breger & Lenz (2008). Amplitudes marked with an asterisk are uncertain.

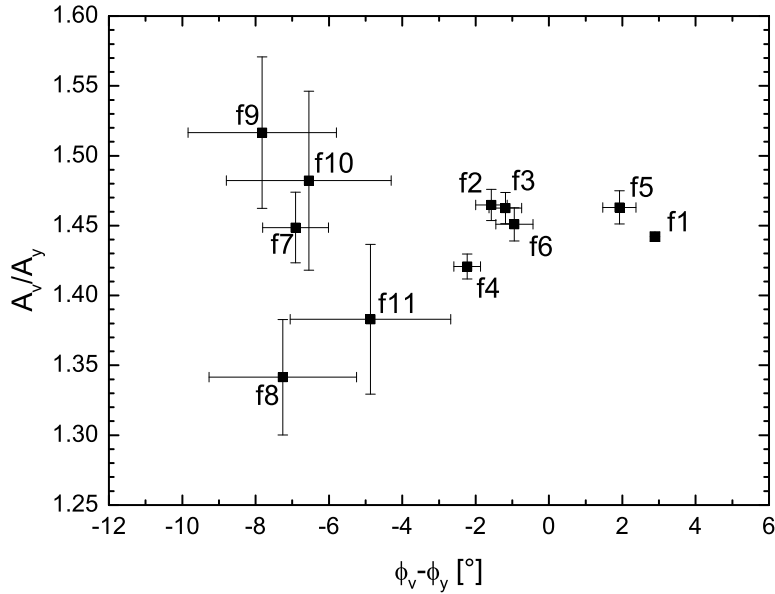


Figure 3.1: Observed amplitude ratios and phase differences for the Strömgren ν and y passbands. Only detected frequencies with sufficiently small error bars are considered.

Computation of theoretical amplitude ratios and phase differences

To compute the positions of modes of different spherical degree in the diagnostic diagrams a stellar model with an appropriate effective temperature and luminosity is required. Esti-

Frequency		A_v/A_y				
ID	$[\text{cd}^{-1}]$	2000/1	2001/2	2002/3	2004/5	2005/6
f ₁	6.8980	1.448 ± 0.004	1.436 ± 0.010	1.455 ± 0.012	1.430 ± 0.005	1.442 ± 0.006
f ₂	7.0060	1.438 ± 0.009	1.413 ± 0.023	1.560 ± 0.041	1.447 ± 0.022	1.478 ± 0.028
f ₃	9.1174	1.457 ± 0.010	1.449 ± 0.019	1.485 ± 0.022	1.442 ± 0.043	1.431 ± 0.295
f ₄	11.5196	1.426 ± 0.009	1.433 ± 0.022	1.422 ± 0.026	1.428 ± 0.020	1.383 ± 0.022
f ₅	8.9606	1.447 ± 0.012	1.478 ± 0.032	1.522 ± 0.044	1.432 ± 0.016	1.445 ± 0.018
f ₆	9.5611	1.472 ± 0.017	1.465 ± 0.023	1.455 ± 0.022	0.799 ± 0.139	1.470 ± 0.023
f ₇	7.3031	1.486 ± 0.029	1.514 ± 0.074	1.425 ± 0.097	1.425 ± 0.025	1.427 ± 0.043
f ₈	6.7955	1.364 ± 0.062	1.483 ± 0.091	1.024 ± 0.154	1.387 ± 0.092	1.374 ± 0.067
f ₉	9.5828	1.567 ± 0.096	1.705 ± 0.157	1.441 ± 0.083	1.537 ± 0.125	1.250 ± 0.180
f ₁₀	6.3390	1.389 ± 0.071	1.412 ± 0.175	1.811 ± 0.213	1.414 ± 0.105	1.312 ± 0.072
f ₁₁	8.6391	1.341 ± 0.070	1.301 ± 0.192	1.321 ± 0.195	1.471 ± 0.071	1.386 ± 0.079
f ₁₂	11.2947	1.536 ± 0.200	1.219 ± 0.206	1.234 ± 0.183	1.469 ± 0.129	1.380 ± 0.116
f ₁₃	12.6915	1.484 ± 0.281	1.144 ± 0.577	2.236 ± 1.048	1.524 ± 1.735	1.015 ± 0.689
f ₁₄	5.3047	1.364 ± 0.191	2.313 ± 0.398	1.511 ± 0.210	1.444 ± 0.287	0.976 ± 0.325
f ₁₅	7.7897	1.303 ± 0.248	1.314 ± 0.325	1.074 ± 0.216	2.800 ± 2.252	1.129 ± 0.153

Table 3.3: Observed amplitude ratios A_v/A_y .

Frequency		$\phi_v - \phi_y$ [°]				
ID	$[\text{cd}^{-1}]$	2000/1	2001/2	2002/3	2004/5	2005/6
f ₁	6.8980	2.81 ± 0.18	3.25 ± 0.38	2.71 ± 0.44	3.12 ± 0.21	2.62 ± 0.23
f ₂	7.0060	-1.62 ± 0.35	-1.00 ± 0.98	-0.99 ± 1.53	-1.53 ± 0.83	-3.38 ± 1.08
f ₃	9.1174	-1.89 ± 0.40	-0.73 ± 0.76	-1.00 ± 0.91	-1.93 ± 1.72	6.66 ± 10.83
f ₄	11.5196	-1.98 ± 0.36	-1.78 ± 0.89	-2.26 ± 1.04	-2.20 ± 0.80	-3.29 ± 0.97
f ₅	8.9606	2.07 ± 0.48	1.40 ± 1.18	0.14 ± 1.65	2.92 ± 0.63	2.82 ± 0.73
f ₆	9.5611	-1.17 ± 0.68	1.18 ± 0.93	-1.45 ± 0.92	-20.34 ± 9.90	-0.11 ± 0.90
f ₇	7.3031	-7.17 ± 1.11	-5.97 ± 2.84	-10.70 ± 3.22	-5.31 ± 0.99	-5.36 ± 1.78
f ₈	6.7955	-4.83 ± 2.67	-4.58 ± 3.70	-26.04 ± 9.38	-4.17 ± 3.88	-2.03 ± 2.66
f ₉	9.5828	-7.26 ± 3.54	-11.90 ± 5.20	-7.40 ± 3.29	-1.28 ± 4.72	-18.52 ± 7.75
f ₁₀	6.3390	-1.21 ± 2.92	4.91 ± 7.22	-19.55 ± 6.72	-2.41 ± 4.23	-7.63 ± 3.05
f ₁₁	8.6391	-8.22 ± 3.01	-18.14 ± 8.42	4.36 ± 7.87	-6.95 ± 2.75	-1.20 ± 3.37
f ₁₂	11.2947	-10.40 ± 7.51	-2.33 ± 9.45	6.19 ± 8.17	-3.32 ± 5.09	-1.08 ± 4.99
f ₁₃	12.6915	10.26 ± 10.79	-58.93 ± 28.91	15.47 ± 25.68	-333.23 ± 65.10	-42.39 ± 31.16
f ₁₄	5.3047	-8.25 ± 7.92	-10.75 ± 22.02	-12.98 ± 16.91	15.61 ± 8.49	16.02 ± 12.81
f ₁₅	7.7897	-13.87 ± 10.82	-14.62 ± 18.37	19.55 ± 11.11	45.20 ± 45.64	-23.27 ± 13.16

Table 3.4: Observed phase differences $\phi_v - \phi_y$.

mates of the fundamental parameters of 44 Tau were derived in section 1.3.1. We computed evolutionary models for a range of masses relying on the standard recipe (OPAL opacities, GN93 element mixture, normal chemical composition with $X=0.70$, $Z=0.02$). An evolutionary track for $1.82 M_{\odot}$ reproduces a model in the center of the photometric box as shown in Figure 3.2.

For the model in the middle of the photometric error box ($T_{\text{eff}} = 6900$ K and $\log L/L_{\odot} = 1.305$) the theoretical amplitude ratios and phase differences were computed. An underlying

	Frequency [cd^{-1}]	A_v/A_y	$\phi_v-\phi_y$ [$^\circ$]
f_1	6.8980	1.442 ± 0.003	$+2.89 \pm 0.13$
f_2	7.0060	1.465 ± 0.011	-1.57 ± 0.43
f_3	9.1174	1.463 ± 0.011	-1.19 ± 0.45
f_4	11.5196	1.421 ± 0.009	-2.23 ± 0.36
f_5	8.9606	1.463 ± 0.012	$+1.92 \pm 0.45$
f_6	9.5611	1.451 ± 0.012	-0.94 ± 0.51
f_7	7.3031	1.449 ± 0.025	-6.91 ± 0.90
f_8	6.7955	1.342 ± 0.041	-7.26 ± 2.01
f_9	9.5828	1.517 ± 0.054	-7.82 ± 2.02
f_{10}	6.3390	1.482 ± 0.064	-6.55 ± 2.24
f_{11}	8.6391	1.383 ± 0.054	-4.87 ± 2.19
f_{12}	11.2947	1.368 ± 0.072	-1.28 ± 3.08
f_{13}	12.6915	1.611 ± 0.381	-30.70 ± 11.55
f_{14}	5.3047	1.521 ± 0.189	-1.28 ± 6.69
f_{15}	7.7897	1.292 ± 0.215	$+2.59 \pm 7.31$

Table 3.5: Mean observed amplitude ratios and phase differences obtained by weighting with the annual SNR of the frequency.

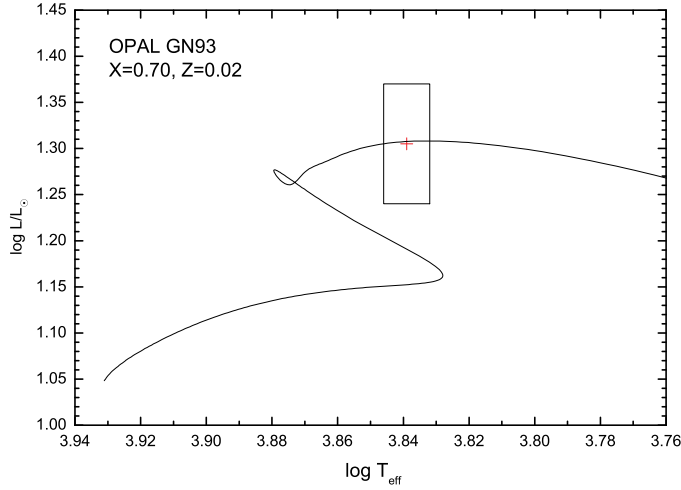


Figure 3.2: Evolutionary track of a nonrotating model with $1.82 M_\odot$.

atmosphere model with $[M/H]=0.0$ and a microturbulence velocity, v_{mic} , of 2 km s^{-1} was chosen. The adopted value for v_{mic} is close to the measurements of Zima et al. (2007) who derived 1.85 km s^{-1} from the equivalent widths and 1.30 km s^{-1} from a line synthesis.

The selected model is a post-main sequence model. The actual evolutionary stage only has a minor effect on the mode identification. The theoretical amplitude ratios and

phase differences are sensitive to the conditions in the outer envelope while the evolutionary changes are mainly in the deep interior of the star. As mentioned before, the results are very sensitive to convection in the envelope. In this study the standard mixing-length theory of convection is used which parametrizes the efficiency of convection by the mixing-length parameter, α_{MLT} . α_{MLT} describes the travel distance of convective elements in units of pressure scale heights. Hence the efficiency of energy transport due to convection increases as α_{MLT} increases.

In Figure 3.3 the computed amplitude ratios and phase differences for different values of the mixing-length parameter, α_{MLT} , are compared to the observed values. In the diagram only predicted modes inside the observed frequency range are shown. For $\alpha_{\text{MLT}}=0.4$ there is no good agreement between observed and theoretical mode positions. Instead, the mixing-length parameter can be restricted to $\alpha \lesssim 0.2$. This means that envelope convection is not very efficient in 44 Tau.

Two observed modes, f_1 and f_5 , have positive phase shifts, which indicates that they are radial modes. The position of the modes f_2 , f_3 , f_4 and f_6 in the diagram are in good agreement with the theoretical amplitude ratios and phase differences of $\ell=1$ modes. The error bars of the remaining observed modes are already considerably larger. However, the most likely spherical degree of some of these modes (f_7 , f_9 , f_{10}) is $\ell=2$. The theoretical positions of $\ell=3$ and 4 modes are outside the scale of this diagram.

It is also important to test the influence of other parameters on the theoretical amplitude ratios and phase differences. Differences in the modeling of the outer envelope of a δ Scuti star may also arise from the choice of opacity data, because deviations in the radiative opacities lead, e.g., to more extended convection zones. In particular we tested the choice of low-temperature opacities on the predicted mode positions in the diagnostic diagrams. We computed evolutionary tracks through the center of the photometric box using the OPAL and OP opacities extended with the AF94 or F05 low-temperature opacities. Both the GN93 and the A04 element mixtures were adopted. The results are given in Figure 3.4. It can be seen that the choice of opacity data does not pose a severe problem for the spherical degree identification in 44 Tau. The error bars of the observations are too large to favor a specific configuration of opacities.

As already mentioned, the influence of the evolutionary stage on mode identification is expected to be negligible. Figure 3.5 compares the results for the post-main sequence model with a main sequence model constructed with an overshooting parameter of $\alpha_{\text{ov}}=0.3$, a mass of $1.940 M_{\odot}$ and, otherwise, the same input parameters as the post-MS model. As can be seen in the diagram the mode positions are almost the same.

In Figure 3.6 the influence of the uncertainties in luminosity and temperature on the theoretical mode positions is presented. The impact on the predicted amplitude ratios and phase differences is too small to change the derived mode identifications.

The photometric spherical degree identification is indeed definitive for many modes in 44 Tau. Moreover, due to the slow rotation mode coupling (Daszyńska-Daszkiewicz et al. 2002) which may influence the amplitude and phase of a mode is not important for 44 Tau

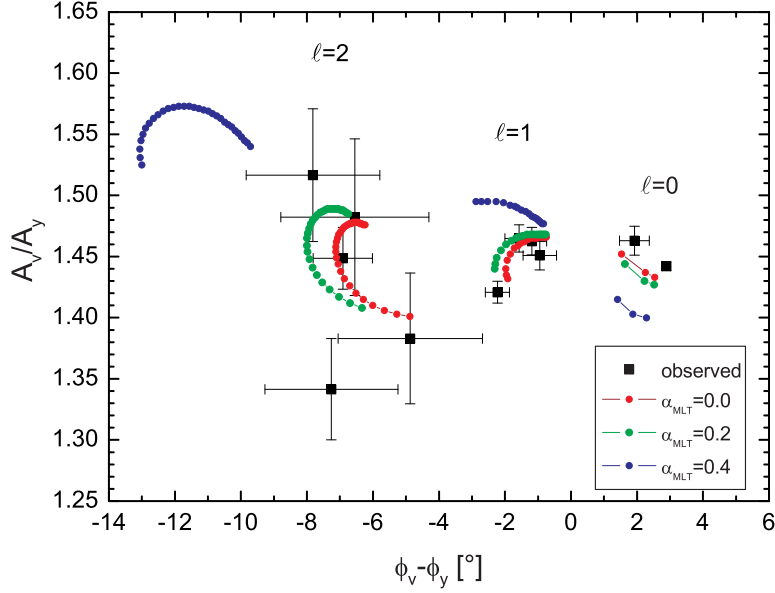


Figure 3.3: Predicted amplitude ratios and phase differences for different mixing-length parameters α_{MLT} . Theoretical mode positions are given with points connected by lines. Only the observed frequency range of 44 Tau ($5.30\text{--}12.70 \text{ cd}^{-1}$) was considered. See Fig. 3.1 for the labels of observed modes.

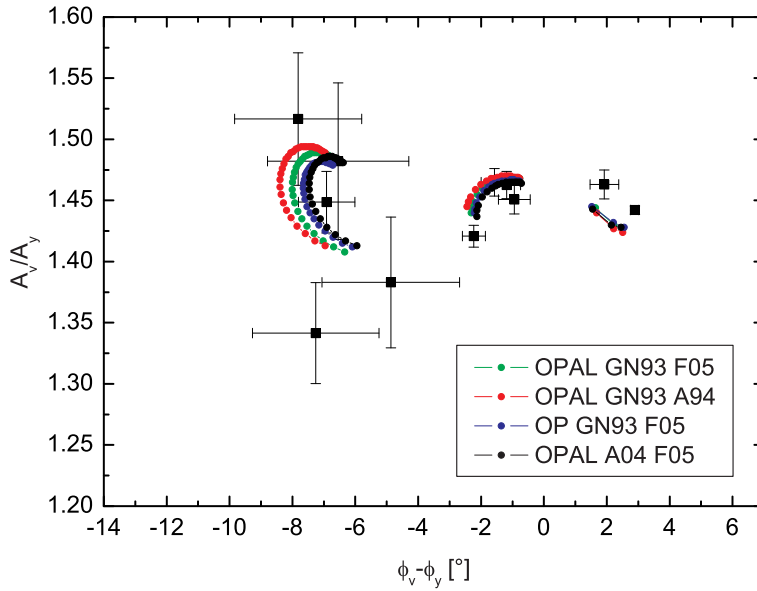


Figure 3.4: Influence of opacity data and element mixtures on the results. Each underlying model is situated at the center of the photometric box. See Fig. 3.1 for the labels of observed modes.

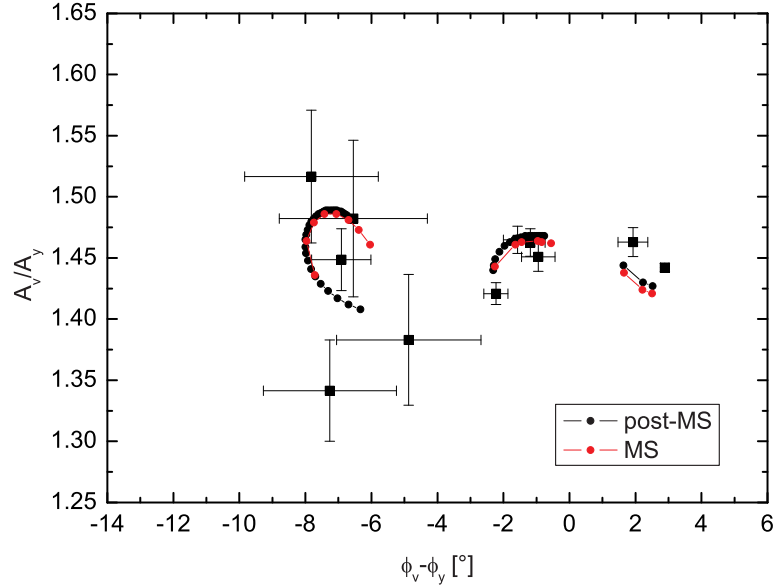


Figure 3.5: Predicted amplitude ratios and phase differences for a post-main sequence and a main sequence model which are both situated at the center of the photometric box in the HR diagram. See Fig. 3.1 for the labels of observed modes.

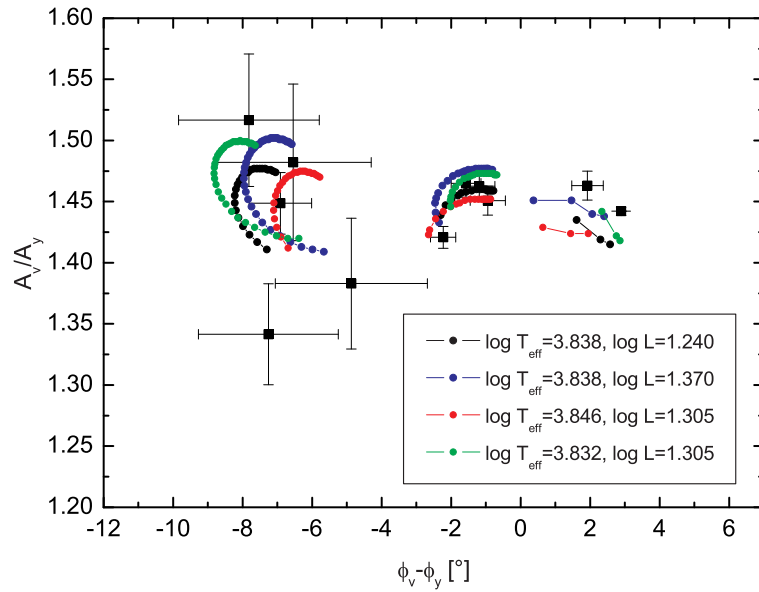


Figure 3.6: Theoretical mode positions for models at the edges of the photometric error box in the HR diagram. See Fig. 3.1 for labels of observed modes.

and can, therefore, be neglected. The spherical degree identification based on the upper diagrams is listed in Table 3.7.

3.2.2 Spectroscopic mode identification

Summary of the LPV analysis of Zima et al. (2007)

Since 44 Tau rotates very slowly, spectroscopic mode identification methods that rely on the Doppler broadening of absorption lines, such as the FPF method, cannot be used. Therefore, only the Moment method could be applied to 44 Tau. Table 3.6 lists the identified azimuthal orders, m , for the observed modes.

	Frequency [cd^{-1}]	m	$A_{\langle v^1 \rangle}$ [km s^{-1}]	$\text{SNR}_{\langle v^1 \rangle}$
f_1	6.8980	0	2.22	100.5
f_2	7.0060	1	0.46	21.2
f_3	9.1175	1	0.44	24.3
f_4	11.5196	0	0.73	40.6
f_5	8.9606	0	1.03	55.6
f_6	9.5613	-	0.30	15.9
f_7	7.3034	0	0.70	33.1
f_8	6.7953	0	0.28	12.6
f_9	9.5801	-	0.12	6.4
f_{10}	6.3390	-	0.21	8.5
f_{11}	8.6394	0	0.32	17.1
f_{12}	11.2946	-	0.11	5.8

Table 3.6: Results of Zima et al. (2007).

The close frequency pair, f_6 (9.56 cd^{-1}) and f_9 (9.58 cd^{-1}), is not sufficiently resolved in the spectroscopic data set. According to the criterion by Loumos & Deeming (1978) the given short time baseline corresponds to a frequency resolution of 0.05 cd^{-1} which is larger than the observed frequency spacing between the two modes. However, Zima et al. (2007) argue that after the prewhitening of one peak another significant close signal is present, which can only be removed after prewhitening the second frequency. Consequently, they conclude that both signals exist.

Most of the modes were found to be axisymmetric, which already points to a high inclination (that is equator-on view). From the two non-axisymmetric prograde modes f_2 and f_3 Zima et al. (2007) constrained the possible range for the inclination angle to $35 - 85^\circ$. Thus they concluded from their measured $v \sin i$ value of $2 \pm 1 \text{ km s}^{-1}$ that the equatorial rotational velocity of 44 Tau amounts to $1\text{-}5 \text{ km s}^{-1}$.

3.2.3 Mode identification with the DD-method

Before applying the DD-method to the photometric two-color data and the radial velocities a potential source of error has to be removed. The time stamp of observational data is usually given in the heliocentric Julian date. If the full Julian date is used, the zero point is far in the past and due to missing decimal places in the frequency values and round-off errors the accuracy of the phases is degraded. To decrease such errors, we have subtracted 245 3200 from the Julian date of all data points prior to computing the frequency solution.

Due to the longer time baseline, the frequencies are more accurately determined from the photometric data. Therefore, the photometric frequency values were used for the prewhitening of the radial velocity data. It is crucial to use exactly the same frequency values for both the photometry and radial velocity data.

The 12 dominant frequencies in photometry could also be detected in the radial velocity data. Wolfgang Zima kindly provided the accurate values of the frequency solution for the radial velocity data for the chosen time zeropoint. The uncertainties of amplitudes and phases were computed by Period04 by means of Monte Carlo simulations. In the present analysis we did not consider the close pair f_6 and f_9 because the amplitudes and phases in the radial velocity data are only poorly determined because they are not well resolved. It is, therefore, safer to determine the spherical degree of these modes with the photometric data only, as has been done in the previous section.

Figure 3.7 presents the results of the DD-method obtained for the same atmosphere model as was used for the photometric mode identification. The diagrams not only show the results for a model in the center of the photometric box (points connected with a line) but also the result of models with different effective temperatures (mean $T_{\text{eff}} \pm 1\sigma$) and luminosities (mean $\log L \pm 1\sigma$). As can be seen, the uncertainties in temperature and luminosity do not cause ambiguities in the mode identifications in 44 Tau. For a reliable mode identification a clear minimum in χ^2 is required. f_1 and f_5 are clearly identified as radial modes. f_2 , f_3 , f_4 are identified as $\ell=1$ modes with a high probability. f_7 is definitely an $\ell=2$ mode, for f_8 and f_{10} the χ^2 values are not as strongly distinguished as for f_7 , but are still clearly seen as $\ell = 2$ modes. For f_{11} $\ell=2$ or 1 are most likely and for f_{12} one cannot discriminate between $\ell=2,1$ or 0 from the computed χ^2 values.

3.2.4 Summary of mode identification for 44 Tau

Table 3.7 summarizes the mode identifications for 44 Tau. The results obtained with different methods are in excellent agreement. For six modes both the spherical degree and the azimuthal number are unambiguously determined. No candidate modes to directly measure the rotational splitting from multiple components could be found.

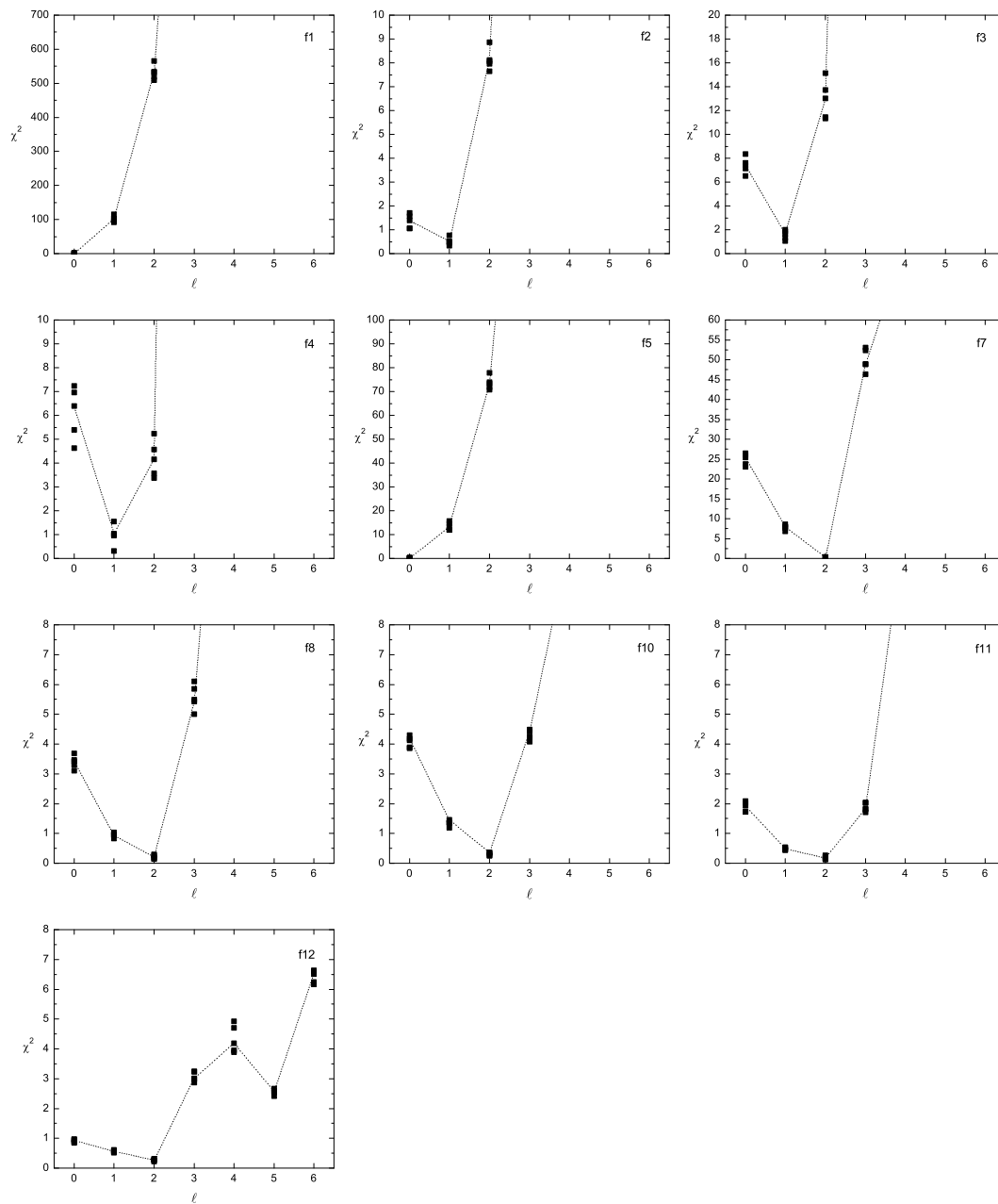


Figure 3.7: Determination of the spherical degree of the modes in 44 Tau with the DD-method. The results for a model in the center of the photometric box in the HRD are connected with a line. Results for models with 1σ changes in effective temperature and luminosity are also shown. The lowest minima in χ^2 indicate the most probable identification. Note the different scales in χ^2 .

Method:	photometric MI	DD-method	Moment method
Data sets:	vy photometry 2000-2006	vy photometry spectroscopy (RV) 2004	spectroscopy (LPV) 2004
Reference:	this work	this work	Zima et al. (2007)
Frequency [cd^{-1}]	ℓ	ℓ	m
f_1	6.8980	0	0
f_2	7.0060	1	1
f_3	9.1174	1	1
f_4	11.5196	1	0
f_5	8.9606	0	0
f_6	9.5611	1	-
f_7	7.3031	2	0
f_8	6.7955	-	0
f_9	9.5828	2	-
f_{10}	6.3390	2	-
f_{11}	8.6391	-	0
f_{12}	11.2947	-	-
f_{13}	12.6915	-	-
f_{14}	5.3047	-	-
f_{15}	7.7897	-	-

Table 3.7: Summary of mode identifications for 44 Tau.

3.3 Application to 4 CVn

3.3.1 Photometric mode identification

A comprehensive analysis of the frequency content of 4 CVn was made by Breger et al. (1999b). The authors reported 18 independent frequencies in the photometric data from 1996. After a break of several years new extensive photometric data were gathered with the Automatic Photoelectric Telescope in Arizona starting from 2005. Table 3.8 illustrates the observational effort from 2005 to 2008.

Season	Observations	Observatories
2005	278 h during 62 nights	APT 0.75m
2006	291 h during 63 nights	APT 0.75m
2007	400 h during 86 nights	APT 0.75m
2008	379 h during 87 nights	APT 0.75m

Table 3.8: Observing log for 4 CVn from 2005 to 2008.

Since the main aim of this long-term campaign is the investigation of the strong am-

	Frequency [cd^{-1}]	A_v/A_y				Mean A_v/A_y	Sigma
		2005	2006	2007	2008		
f_1	8.59427	1.486	1.458	1.468	1.467	1.470	0.006
f_2	5.04795	1.553	1.537	1.547	1.539	1.544	0.004
f_3	5.85074	1.455	1.464	1.463	1.469	1.463	0.003
f_4	6.97644	1.530	1.544	1.555	1.552	1.545	0.006
f_5	5.53239	1.477	1.476	1.491	1.509	1.488	0.008
f_6	7.37511	1.533	1.486	1.493	1.511	1.506	0.011
f_7	7.55149	1.458	1.470	1.472	1.464	1.466	0.003

	Frequency [cd^{-1}]	$\phi_v - \phi_y$ [$^\circ$]				Mean $\phi_v - \phi_y$ [$^\circ$]	Sigma [$^\circ$]
		2005	2006	2007	2008		
f_1	8.59427	-2.852	-2.495	-2.289	-2.664	-2.575	0.120
f_2	5.04795	-2.270	-2.058	-2.124	-2.528	-2.245	0.104
f_3	5.85074	-6.002	-7.102	-6.270	-7.045	-6.605	0.276
f_4	6.97644	0.841	-0.081	0.194	0.697	0.413	0.215
f_5	5.53239	-5.622	-6.693	-6.032	-4.695	-5.760	0.418
f_6	7.37511	-2.732	-2.504	-2.746	-1.942	-2.481	0.188
f_7	7.55149	-2.624	-3.424	-1.918	-2.637	-2.651	0.308

Table 3.9: Observed amplitude ratios and phase differences in 4 CVn. The formal uncertainties of the mean values were obtained by error propagation from the annual uncertainties.

plitude variability of 4 CVn more observations are still retrieved. Thus the data are not yet published. In this work only the data obtained during the four years from 2005 to 2008 are considered.

Observational amplitude ratios and phase differences

The mean observational amplitude ratios and phase differences between the Strömgren v and y passband were determined by Michel Breger. A complicating fact in this task is the strong amplitude modulation of the pulsation modes in 4 CVn which is discussed in detail in Breger (2000). Therefore, annual frequency solutions have to be made to determine the amplitudes and phases. This can only be done in a reasonable way for modes which exhibit a sufficient signal to noise in the annual solutions. Therefore, for the 2005-2008 data set only seven frequencies are considered at the present stage. Some of the dominant frequencies in the 1996 data set, such as the modes at 6.117 and 6.190 cd^{-1} , have much smaller amplitudes in the more recent 2005-2008 data sets and, therefore, could not be included. The results are provided in Table 3.9.

The uncertainties of the mean amplitude ratios and phase differences were determined in the same way as for 44 Tau. Due to the extensive data base the uncertainties of the frequencies are lower than $1 \cdot 10^{-5} \text{ cd}^{-1}$. It is remarkable that despite the strong amplitude variability of 4 CVn the amplitude ratios of the modes remain quite stable throughout

the different years. This means that mode identification is not affected by amplitude modulation. Figure 3.8 shows the position of the examined seven modes in an amplitude ratios vs. phase differences diagram. As for 44 Tau, distinct groups in the distribution of the phase differences can be found.

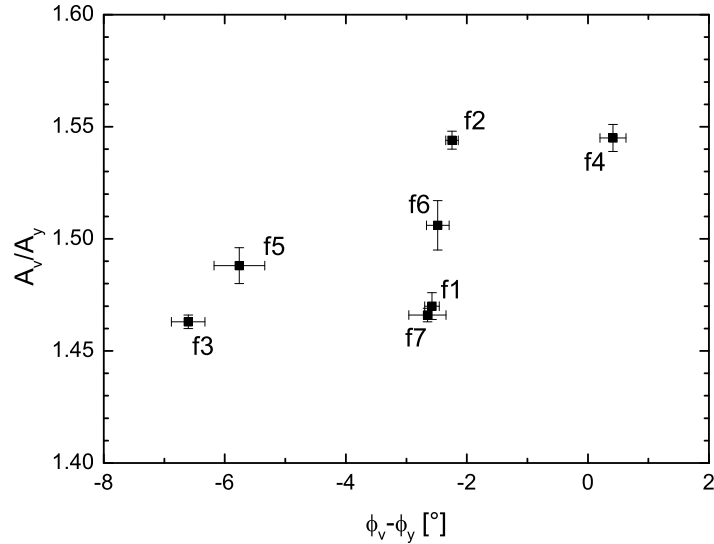


Figure 3.8: Observed amplitude ratios and phase differences between the Strömgren v and y passbands for the seven dominant modes in 4 CVn.

Comparison with theoretical amplitude ratios and phase differences

As mentioned in section 1.3.3 the photometric calibrations indicate an overabundance of metals in the outer envelope of 4 CVn. The photometrically derived metallicity, $[M/H]$, is $+0.20 \pm 0.15$ dex. Unfortunately, a detailed analysis of the photospheric elements (as has been done for 44 Tau) is not yet available. Regarding the high uncertainties in $[M/H]$, the possibility of a normal (solar) metallicity was not excluded in our analyses. In the calculations of theoretical amplitude ratios and phase differences the metallicity can be adjusted by changing the metallicity of the evolutionary models and, independently, by changing the metallicity of the stellar atmosphere models. For example, this allows for assuming solar composition in the stellar interior and overabundant metals in the atmosphere. The strongest impact on the mode positions in the diagnostic diagrams is imposed by the choice of metallicity of the atmosphere model. The variation of the metallicity of the evolutionary model has a much smaller effect, which is mainly due to the change in the surface gravity.

To find a representative model in the center of the photometric error box in the HR diagram we constructed a sequence of models adopting the OPAL opacities and the GN93 element mixture. The observed projected rotational velocity is around 120 km s^{-1} . However, this value is currently not well constrained. To obtain models inside the photometric

box at this lower limit of the equatorial rotation rate, an initial rotation rate of 150 km s^{-1} was adopted. Convective overshooting was neglected. Different mixing-length parameters and two different metal mass fractions ($Z=0.02$ and $Z=0.025$) were used. Note that $Z=0.025$ corresponds to a metallicity which is slightly lower than $[M/H]=+0.20$. When a standard chemical composition is assumed, a model with $2.10 M_{\odot}$ matches the position in the center of the HR diagram. For the model with a higher metallicity, $Z=0.025$, the mass has to be increased to $2.18 M_{\odot}$ to fit approximately the same position in the HR diagram. The evolutionary tracks of both models are shown in Figure 3.9.

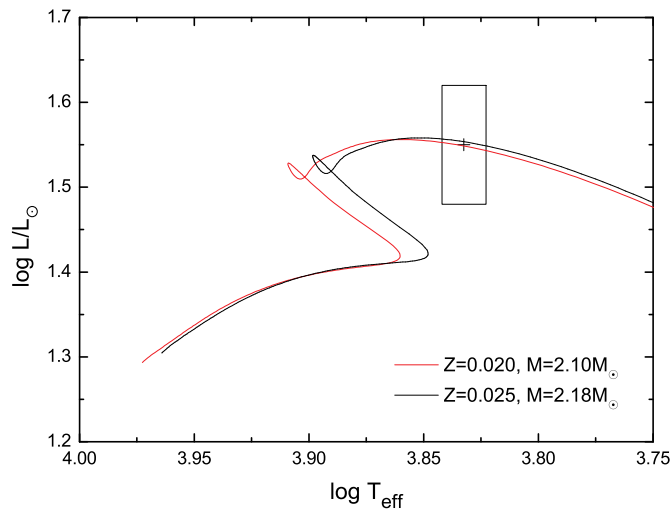


Figure 3.9: The evolutionary tracks of two reference models used for mode identification in 4 CVn.

A first comparison between the theoretical amplitude ratios and phase differences computed for these models and the observed values is given in Figure 3.10. The diagram shows the results for the evolutionary model with $Z=0.025$ and a model atmosphere with $[M/H]=+0.20$ and a microturbulence velocity of 4 km s^{-1} . If not stated otherwise the same value for the microturbulence velocity was adopted in all subsequent models. The differences to the mode positions obtained for the evolutionary model with $Z=0.02$ is very small. Therefore, it can be concluded that the metallicity adopted in the evolutionary model is not an important factor in this analysis.

It is obvious that the agreement between theory and observations is not as good as for 44 Tau. The formal uncertainties of the observed amplitude ratios and phase differences may underestimate the true errors. On the other hand adopting larger uncertainties did not improve the agreement significantly. Consequently, possible uncertainty factors in the theoretical predictions have to be considered in more detail. For the previously examined star, 44 Tau, Figure 3.6 already illustrated the temperature and luminosity dependence of the mode positions in the diagnostic diagram. Due to the larger uncertainties in the derived fundamental parameters of 4 CVn the effects may be larger for this star.

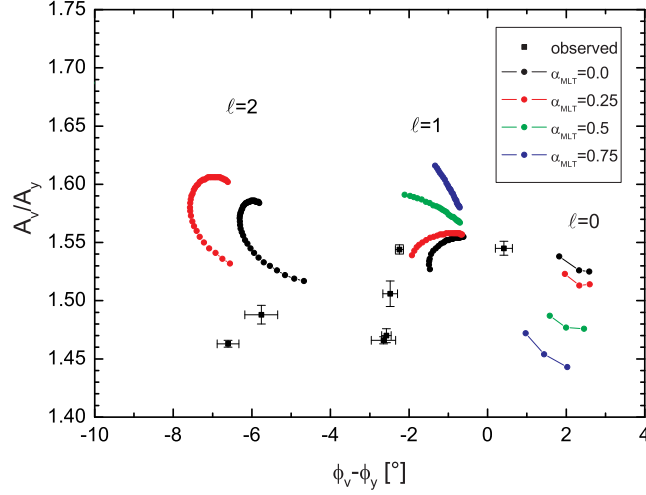


Figure 3.10: Comparison between observed amplitude ratios and phase differences with theoretical models using different values of α_{MLT} and a model atmosphere with $[M/H] = +0.20$ and $v_{\text{mic}} = 4 \text{ km s}^{-1}$.

We computed an extensive model grid that covers the complete photometric box in the HR diagram with models of different masses. The adopted masses change in steps of $0.02 M_{\odot}$. Moreover, α_{MLT} was varied in steps of 0.1 to examine different efficiencies of convection. Otherwise the same parameters as in the previously mentioned 4 CVn models were used. For all models inside the photometric box the corresponding amplitude ratios and phase differences were computed. Atmosphere models with different metallicities were adopted to study the effect of the poorly constrained metallicity.

Figure 3.11 shows the result of these computations for different values of the mixing-length parameter for an atmosphere model with $[M/H] = +0.20$. The spread of the results due to different temperatures and luminosities is not very large. A perfect fit between theory and observation is not achieved. This concerns the amplitude ratios in particular. The effect of adopting different metallicity values in the stellar atmosphere model are shown in Figure 3.12. In this diagram the mixing-length parameter of convection was fixed to $\alpha_{\text{MLT}} = 0.3$. The variation of the metallicity mainly affects the amplitude ratios, but the quality of the results is not good enough to determine a preferred value. While the modes with negative phase differences are in better agreement with metallicities close to solar values, the mode with the positive phase difference prefers a higher metallicity. It may, however, be possible that the neglect of the interaction between pulsation and convection is responsible for the poor agreement.

Nevertheless, some conclusions are possible. The results shown in Figure 3.11 indicate an upper limit for the mixing-length parameter of $\alpha_{\text{MLT}} \approx 0.4$. For $\alpha_{\text{MLT}} \approx 0.0$ some modes with phase differences typical for $\ell=1$ modes are identified as $\ell=2$. The best fit of modes with $\ell=0$ and $\ell=2$ -like phase differences is obtained with $\alpha_{\text{MLT}} \approx 0.0$ while the best

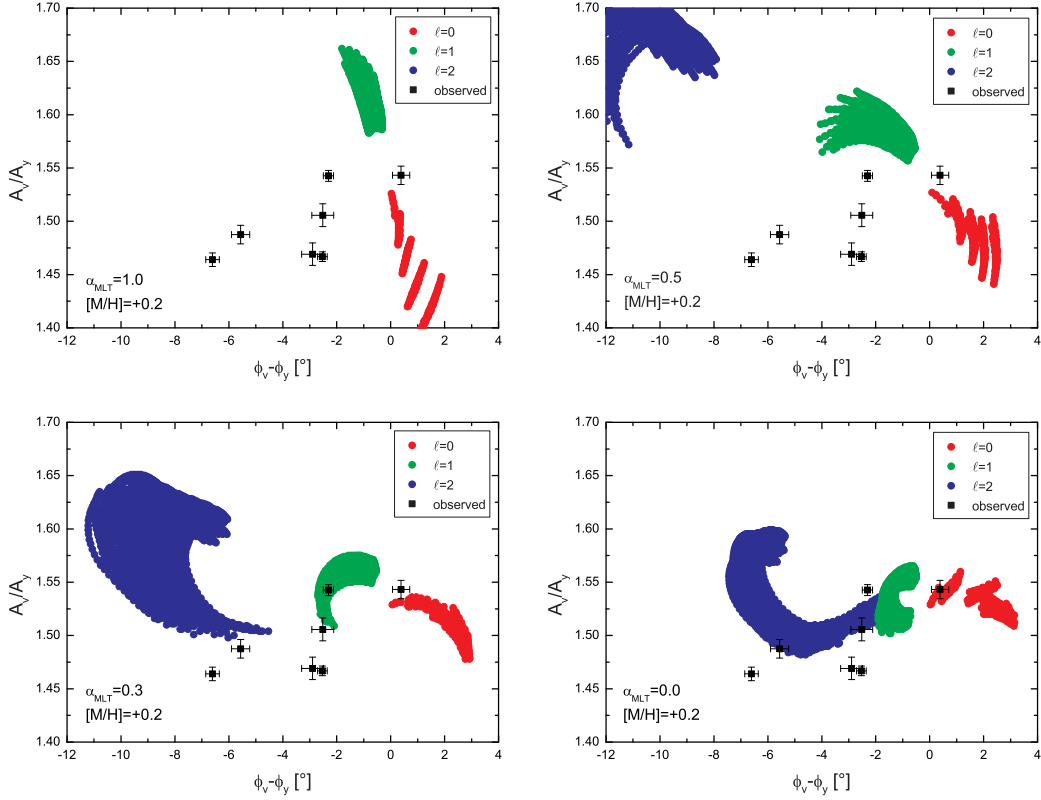


Figure 3.11: Theoretical mode positions for different values of the mixing-length parameter. The results of all models inside the photometric error box are shown. For $\alpha > 0.5$ the $\ell=2$ mode positions are predicted to be outside the scales of the given diagrams.

fit of modes with $\ell=1$ -like phase differences occurs at $\alpha_{\text{MLT}} \approx 0.3$

Caution is needed not to put too much focus on the position of a single mode in the diagnostic diagrams. It was shown by Daszyńska-Daszkiewicz et al. (2002) that for rotating stars mode coupling may significantly affect the amplitude ratio and phase difference. We examined possible shifts of modes due to rotational mode coupling for various models. However, the results strongly depend on the individual frequencies in the pulsation model. Unfortunately, the models examined here do not reproduce the individual frequencies in the observed frequency spectra well enough, so no general conclusions can be made at the moment. However, in some models the mode f_4 (6.976 cd^{-1}) is a radial mode which is coupled to an $\ell=2$, $m=0$ mode of nearly the same frequency. In such a configuration of a coupled pair the radial mode tends to look more like an $\ell=1$ mode than an uncoupled $\ell=0$ mode. However, the strength of this effect depends on the efficiency of the coupling which is strongly dependent on the model. This would explain why the observed phase shift of f_4 , 0.41 cd^{-1} , is closest to the value predicted for the fourth radial overtone which does not agree well with the fundamental parameters of the star. As we will see later the

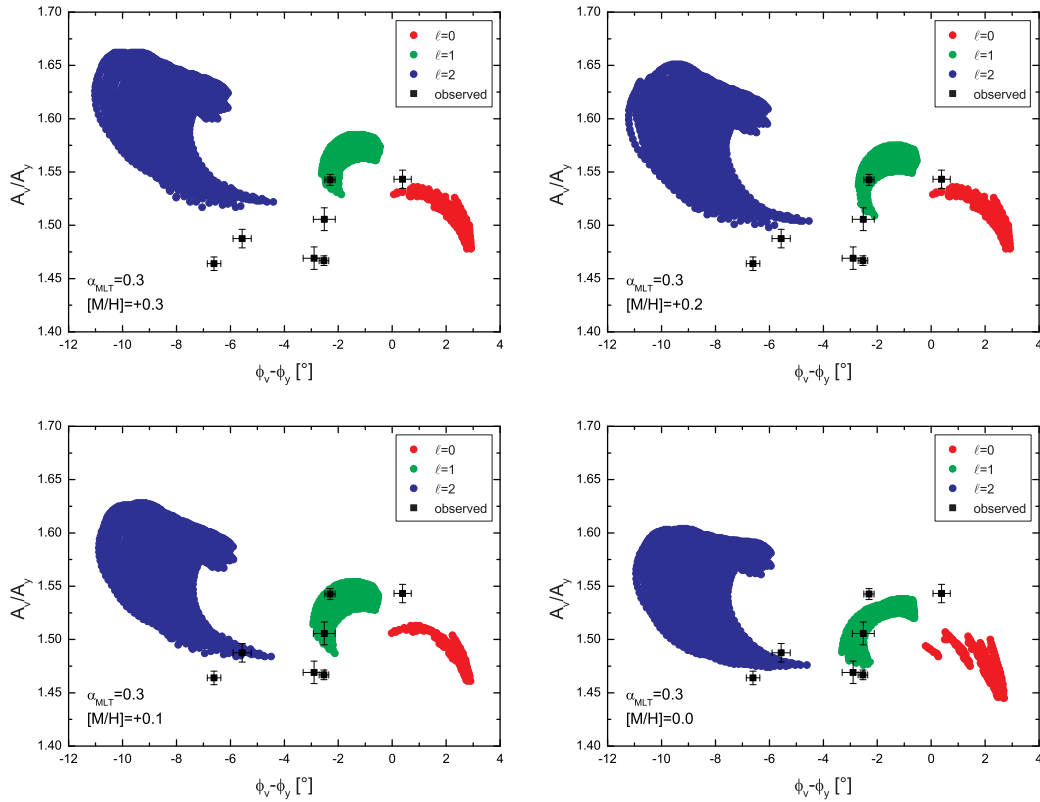


Figure 3.12: Effect of different metallicity on the theoretical mode positions. The underlying evolutionary model was computed with $\alpha_{\text{MLT}} = 0.3$.

asteroseismic models indicate a lower radial order for f_4 which is predicted to have a phase difference higher than 1° .

3.3.2 Spectroscopic mode identification

Summary of the LPV analysis of Castanheira et al. (2008)

In early 2008, 4 CVn was observed for 38 nights at the 2.1m telescope at McDonald Observatory. Based on the line profile variations of the two unblended Fe II lines at 4508.29 and 4549.48 Ångström Castanheira et al. (2008) determined the azimuthal numbers for the five dominant modes utilizing the Fourier Parameter Fit method. They identify f_1 and f_3 as prograde modes with $m = 1$, f_2 and f_6 as retrograde modes with $m = -1$, and f_4 as an axisymmetric mode. It should be noted that their results are preliminary. Currently the spectroscopy members of the Vienna TOPS group are rereducing the spectroscopic data utilizing a better treatment for the determination of the spectral continuum. Moreover, more spectral lines will be used for the line-profile analyses. Therefore, more mode

identification results may be expected in the near future.

3.3.3 Application of the DD-method

The availability of spectroscopic and photometric data in 2008 suggests the application of the DD-method. Our spectroscopy group kindly provided me with the preliminary reduced spectroscopic data. By means of the FAMIAS software (Zima 2008) we extracted the radial velocities for the same two Fe II spectral lines that were used in the analysis of Castanheira et al. (2008). This was done following the recommended procedure according to FAMIAS.

The frequency analysis of the averaged radial velocity curve from the two Fe II lines was done with Period04 (Lenz & Breger 2005). Once a frequency is detected in the radial velocity data the more accurate frequency value of the photometric counterpart is adopted. 12 frequencies were found above the signal to noise criterion of $\text{SNR}=4.0$ (Breger et al. 1993). Another frequency at 5.13 cd^{-1} with a SNR of 3.90 is found close to this limit. As this frequency was already proved to exist in the photometric data with a sufficient SNR (f_{15} in Breger et al. 1999b) we also accepted this detection. The preliminary results are given in Table 3.10. Due to the fact that the spectroscopic data are not final these results should only be considered as preliminary.

	Frequency [cd^{-1}]	m	$A_{\langle v^1 \rangle}$ [km s^{-1}]	$\text{SNR}_{\langle v^1 \rangle}$	SNR_{v_y}
f_1	8.594	1	1.05	9.6	123.5
f_2	5.048	-1	1.75	13.6	89.5
f_3	5.851	1	0.69	5.6	67.4
f_4	6.976	0	0.81	7.0	54.9
f_5	5.532		1.01	7.9	53.2
f_6	7.375	-1	1.55	13.5	31.5
f_7	7.552		0.47	4.1	48.9
f_8	6.118		0.53	4.4	5.1
f_9	6.681		0.69	5.7	4.2
f_{10}	4.748		0.62	4.7	
f_{11}	6.439		0.49	4.1	
f_{12}	6.191		0.57	4.8	
f_{13}	5.139		0.50	3.9	

Table 3.10: Results from the PPF method and the analysis of the radial velocity curve.

In the extensive 2008 photometric data nine frequencies exhibit a $\text{SNR} > 4.0$. Since these nine frequencies are also significant in the radial velocity data, their spherical mode degree can be investigated by means of the DD-method. The uncertainties of the amplitudes and phases in the photometric passbands and the radial velocities were determined by means of Monte Carlo simulations in Period04. As for 44 Tau, the DD-method was applied for a model in the center of the HR diagram and for models at the edges of the photometric

error box (defined by one standard deviation in effective temperature and luminosity). The results are shown in Figure 3.13.

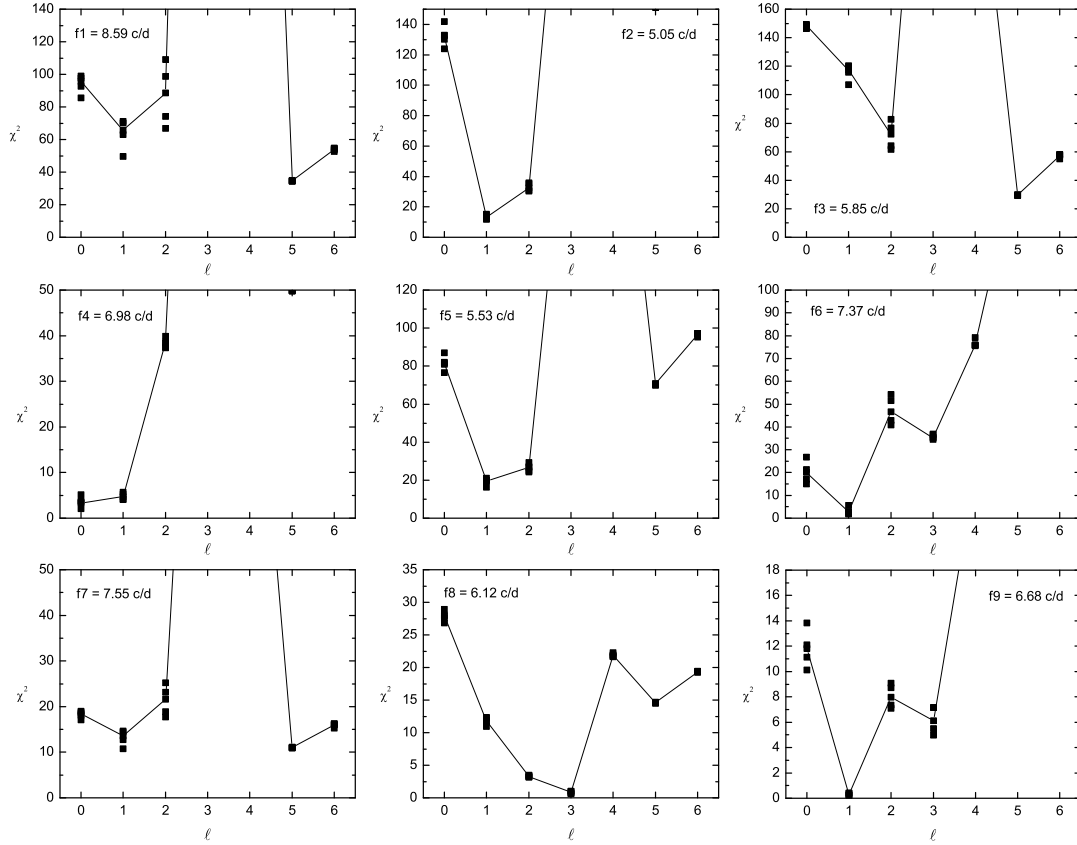


Figure 3.13: Dependence of χ^2 on the spherical degree for the nine dominant modes in 4 CVn. The results of the DD-method for different models at the edges of the photometric error box are shown.

The diagrams show that there is no reliable mode identification for most of the modes. The χ^2 values are much too high and also have unlikely minima at $\ell=5$ and 6 for some pulsation modes. The disc averaging effects for such spherical degrees are large and the photometric amplitudes of such modes are expected to be much smaller than the observed amplitudes of the specific modes. The reason for the poor results is very likely due to the fast rotation of 4 CVn since the equations 3.4 and 3.9 assume a nonrotating case. The rotation rate of 4 CVn is approximately 0.5 cd^{-1} for an equator-on view and higher for other inclinations. This corresponds to Ω/ω of at least 0.1 for the lowest frequencies. Therefore, these results should be taken with caution. For the mode f_4 at 6.98 cd^{-1} photometry indicates $\ell = 0$ due to the clearly positive phase shift. The DD-method finds the lowest χ^2 values at $\ell=0$ and 1 and, unfortunately, does not provide a clear preference. The radial velocity measurements are more strongly affected by rotation than brightness measurements due to the direct influence on the line profiles. Since the results of the DD-method may not

be very reliable in the case of 4 CVn it is safer to rely solely on the results from photometric mode identification which are less affected by rotation.

3.3.4 Summary of mode identification for 4 CVn

Table 3.11 summarizes the mode identification results for 4 CVn. Due to considerable uncertainties in the determination of the spherical degrees, these results should be taken with caution. The identifications from the various methods list the ℓ value with the highest probability first, then the other possible values. The frequency separation between the two quadrupole modes f_3 (5.85 cd^{-1}) and f_5 (5.53 cd^{-1}) is in good agreement with the measured projected rotation velocity, which means that these modes may be components of a rotational splitting. f_3 could be identified as a prograde mode with $m=1$, but unfortunately no azimuthal order could be determined yet for f_5 .

Method:	photometric MI	DD method	FPF method	
Data sets:	vy photometry 2005-2008	vy photometry, spectroscopy (RV) 2008	spectroscopy (LPV) 2008	
Reference:	this work	this work	Castanheira et al. (2008)	
Frequency [cd^{-1}]	ℓ	ℓ	ℓ	m
f_1 8.59	1 (2?)		2, 1	1
f_2 5.04	1	(1,2)	1, 2	-1
f_3 5.85	2		1, 2	1
f_4 6.98	0	(0,1)	2,0,1	0
f_5 5.53	2	(1,2)		
f_6 7.37	1 (2?)	(1)	2, 1	-1
f_7 7.55	1 (2?)			
f_8 6.11		(3,2)		
f_9 4.74				
f_{10} 6.19				
f_{11} 6.44				
f_{12} 6.68		(1)		

Table 3.11: Summary of mode identifications for 4 CVn. The results of the DD-method should be taken with great caution (see discussion in Section 3.3.3).

Chapter 4

Asteroseismic modeling of 44 Tau

During the life of a δ Scuti star on the main sequence it transforms hydrogen into helium in its core. The central nuclear reactions slowly change the stellar structure which causes the star to expand slowly while the surface gravity decreases. Towards the end of this phase the amount of hydrogen in the core gets very low. To keep the energy production from hydrogen burning efficient, the star increases its central temperature by an overall contraction. This leads to an increase in the effective temperature and the surface gravity. At some stage the hydrogen in the core is finally depleted and a hydrogen-burning shell becomes the dominant source of nuclear energy. This causes the stellar envelope to expand again leading to a decrease in the effective temperature and surface gravity.

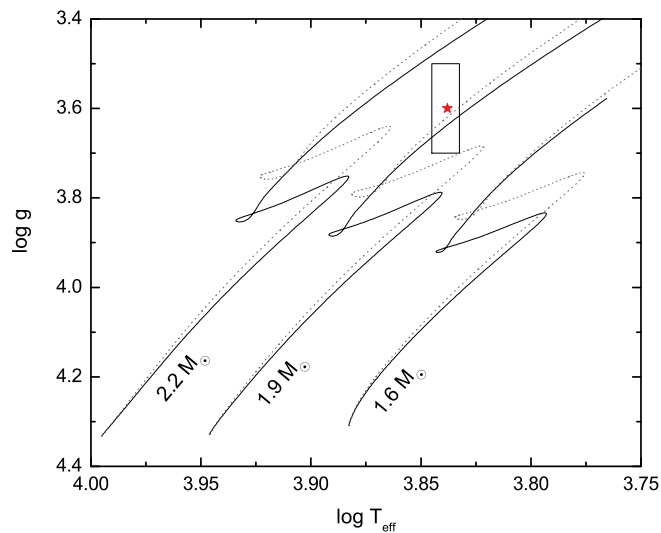


Figure 4.1: Observed position of 44 Tau in a surface gravity versus effective temperature diagram. Evolutionary tracks for stellar models constructed without convective overshooting (solid lines) and with an overshooting parameter of $\alpha_{ov} = 0.2$ (dashed lines) are given.

The close relation between the surface gravity and stellar evolution is often used to determine the evolutionary stage of a star. Figure 4.1 shows evolutionary tracks of stellar models with different masses in a gravity vs. effective temperature diagram. In the first model sequence convective overshooting was neglected, in the second sequence an overshooting parameter of $\alpha_{ov}=0.2$ was assumed. Overshooting increases the amount of hydrogen available for the nuclear reactions in the core and, therefore, increases the life time on the main sequence. The extent of convective overshooting is still subject to uncertainty in δ Scuti stars.

The spectroscopically determined $\log g$ value of 44 Tau is 3.6 ± 0.1 . This puts the star in a region in which an unambiguous identification of its evolutionary stage is not possible. Hence we have to consider the main sequence as well as post-main sequence phases in our asteroseismic modeling.

4.1 The choice of the element mixture

For 44 Tau Zima et al. (2007) obtained the photospheric abundances for several elements from a spectrum synthesis. Table 4.1 compares the measured element abundances in 44 Tau to the GN93 mixture and the more recent A04 solar abundances.

Element	Abundance ($\log N$)			$\Delta(44 \text{ Tau} - \text{Sun})$	
	44 Tau	Sun (GN93)	Sun (A04)	GN93	A04
O	8.63	8.87	8.66	-0.24	-0.03
Mg	7.72	7.58	7.53	0.14	0.19
Ca	6.51	6.36	6.31	0.15	0.20
Sc	2.80	3.17	3.05	-0.37	-0.25
Ti	4.99	5.02	4.90	-0.03	0.09
V	4.06	4.00	4.00	0.06	0.06
Cr	5.79	5.67	5.64	0.12	0.15
Mn	5.60	5.39	5.39	0.21	0.21
Fe	7.59	7.50	7.45	0.09	0.14
Co	5.21	4.92	4.92	0.29	0.29
Ni	6.24	6.25	6.23	-0.01	0.01
Uncertainties	≤ 0.14	≤ 0.10	≤ 0.10		

Table 4.1: Comparison between the abundances of 44 Tau and the Sun.

As can be seen in Table 4.1 and in Figure 4.2, the element abundances of 44 Tau are generally close to those of the Sun. Some elements in 44 Tau are slightly under- or overabundant, though. However, the differences are not much larger than the given uncertainties. Moreover, the abundance pattern of 44 Tau does not show a clear preference for the GN93 or A04 element mixture.

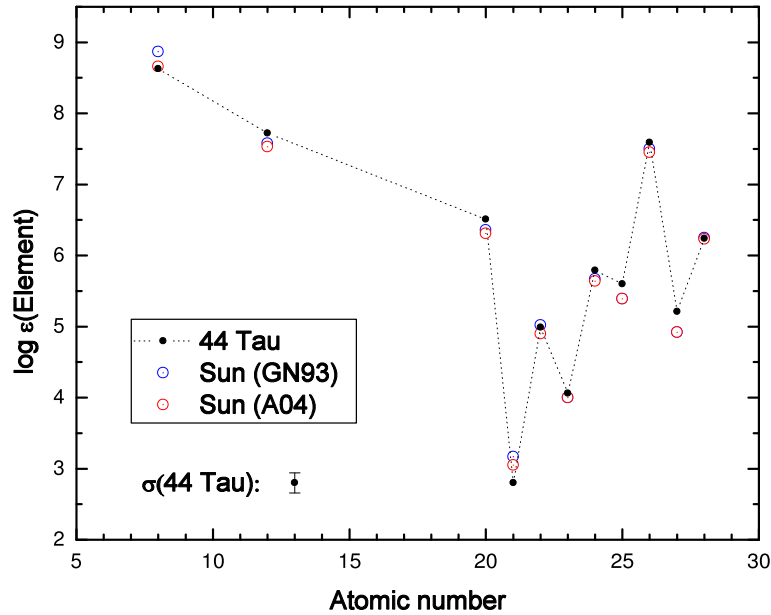


Figure 4.2: Photospheric element abundances of 44 Tau compared to the solar abundances of GN93 and A04.

The web interface of the OPAL project¹ allows for computing OPAL opacities for a user-defined element mixture. Unfortunately, the abundances of important elements such as C and N were not determined in 44 Tau. Therefore, we did not utilize a special element mix, but constructed asteroseismic models of 44 Tau utilizing both solar element mixtures.

4.2 Inferences from the observed radial modes

Radial modes are a good probe for the global parameters of a star. While the frequency of one radial mode is sufficient to determine the mean density of a star, a second radial mode additionally provides a mass constraint. Therefore, the identification of two radial modes in 44 Tau poses an important constraint to the pulsation models. Considering the measured fundamental parameters, the observed spacing of 2.06 cd^{-1} between the two radial modes allows to conclude that the radial order of these modes only differs by one. A difference of two radial orders would be incompatible with the measured fundamental parameters of 44 Tau.

In a Hertzsprung-Russell diagram or a $\log g$ vs. $\log T_{\text{eff}}$ diagram the models which fit the first radial overtone are situated on a line which is slightly inclined to the line of models that fit the radial fundamental mode. This can be clearly seen in Figure 4.3 which shows this situation for post-main sequence models. The model that fits both radial modes

¹<http://adg.lnl.gov/Research/OPAL/new.html>

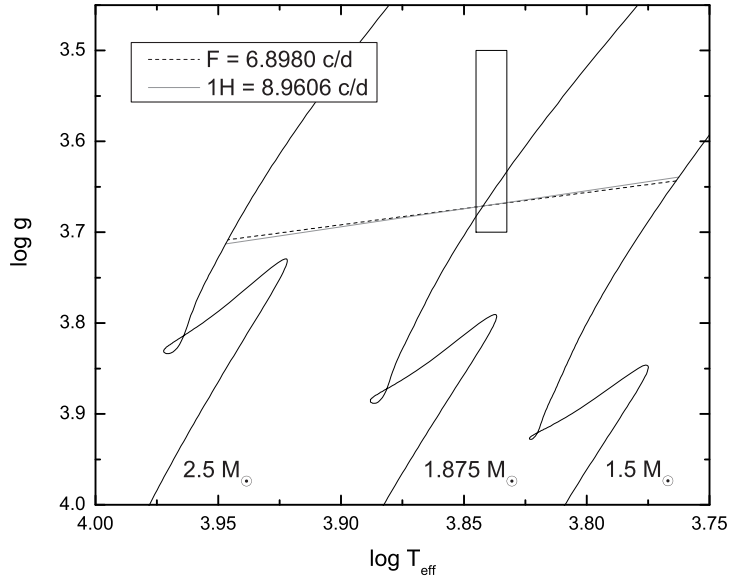


Figure 4.3: $\log g$ vs. $\log T_{\text{eff}}$ diagram. Models with the radial fundamental mode at 6.8980 cd^{-1} are connected by a dashed line and models with the first overtone at 8.9606 cd^{-1} by a solid grey line. The photometric error box is in good agreement with the model at the intersection of the two lines.

simultaneously is situated at the intersection of the two lines, which constrains the mass of the model. For this reason, two identified radial modes restrict the number of possible models significantly.

4.2.1 Petersen diagrams

A convenient tool to find models that fit the observed radial frequencies is the Petersen diagram (Petersen & Jørgensen 1972). In a Petersen diagram the period ratio between two consecutive radial modes is plotted against the period of the mode with lower frequency.

In Figure 4.4 a Petersen diagram is presented for representative models in all possible evolutionary stages for 44 Tau. The observed period ratio between the two radial modes f_1 and f_5 is 0.769815 ± 0.000002 . The low uncertainty is due to the excellent accuracy of the observed periods with a formal uncertainty of only $1.4 \cdot 10^{-5} \text{ d}$. As shown for the post-main sequence expansion case in Figure 4.4 the observed period ratio can be fitted by adjusting the mass of the stellar model. However, the period ratio depends not only on the mass of a star but is also sensitive to changes in metallicity and rotation rate which both modify the stellar density and the surface gravity (Suárez et al. 2006).

Figure 4.5 shows the effect of rotation on the evolutionary track of a model in the Petersen diagram. For 44 Tau the measured rotation rate is $3 \pm 2 \text{ km s}^{-1}$ and, therefore,

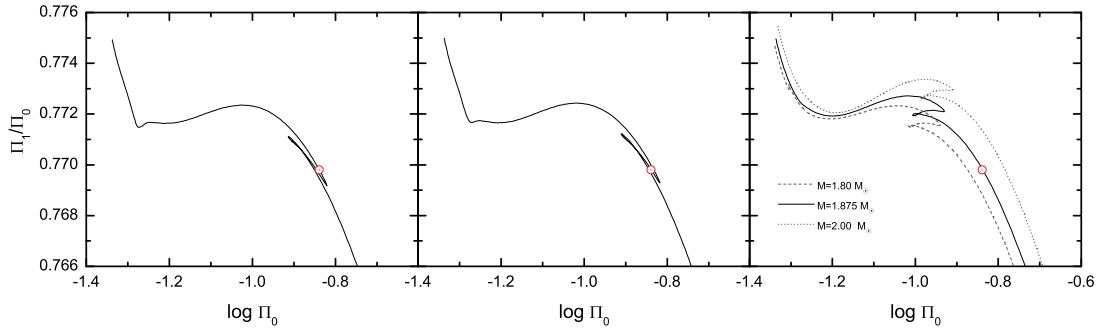


Figure 4.4: Petersen diagrams in which the observed radial period ratio is fit by a main sequence model (left panel), a post-MS contraction model and a post-MS expansion model (right panel). The red circle marks the observed period ratio. The observational uncertainties are smaller than the size of the symbol.

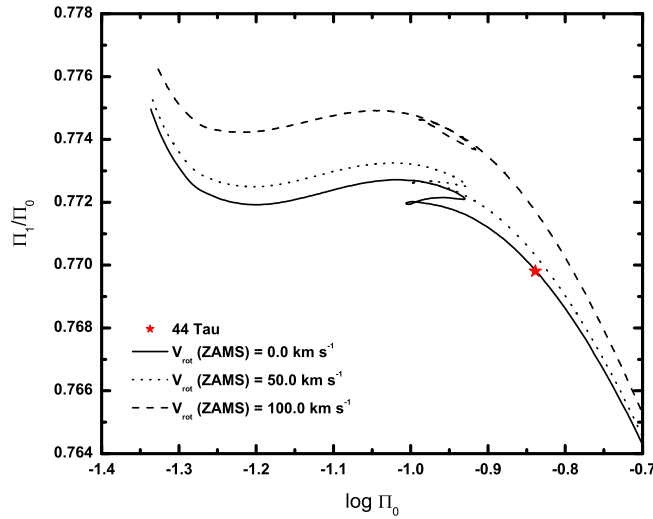


Figure 4.5: Effect of rotation on the radial period ratio.

essentially has a negligible effect. Since the surface abundances in 44 Tau are close to solar, one may also assume normal metallicity for the whole star. Moreover, the effects of different opacity tables and element mixtures are also important, as will be shown later. The dip in the period ratio at the beginning of the main sequence phase is due to the contraction of the convective core and has been discussed in more detail by Templeton et al. (2002).

The fundamental parameters of the three representative models, in Figure 4.4 are given in Table 4.2. The models were computed with OPAL opacities, the GN93 element mixture and assuming no rotation. As can be seen the $\log g$ values is alike in all models despite the three different evolutionary stages.

	X	Z	α_{MLT}	α_{ov}	M/M_{\odot}	$\log T_{\text{eff}}$	$\log L/L_{\odot}$	$\log g$
MS	0.70	0.02	0.2	0.3	1.847	3.8088	1.2205	3.6702
post-MS contraction	0.70	0.02	0.2	0.0	1.862	3.8118	1.2353	3.6713
post-MS expansion	0.70	0.02	0.2	0.0	1.875	3.8422	1.3601	3.6712

Table 4.2: Parameters of the representative models. For all models OPAL opacities and the GN93 element mixture were adopted.

For a more quantitative investigation we constructed a grid of stellar models adopting different chemical compositions, mixing-length and overshooting parameters. As for the representative models the OPAL opacities and the GN93 element mixture were used and only nonrotating models were constructed. Table 4.3 lists the wide range of the chosen input parameters (with the initial standard values for 44 Tau given in bold face).

Parameter	Range of values
X	0.65, 0.70 , 0.75
Z	0.015, 0.02 , 0.025, 0.03, 0.04
α_{MLT}	0.0, 0.2 , 0.5
α_{ov}	0.0 , 0.1, 0.2, 0.3, 0.4

Table 4.3: Parameter range for the model grid.

Along each evolutionary track in this model grid, the corresponding radial modes were computed. By means of Petersen diagrams the stellar mass of the model that fits both observed radial modes for the given input parameters was determined. Figure 4.6 shows the position of these models in a HR diagram separately for each evolutionary stage.

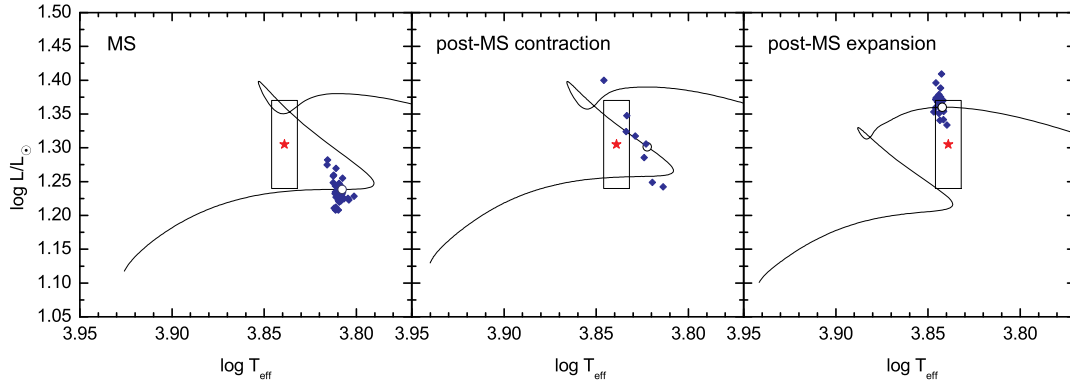


Figure 4.6: Position of models that fit the observed radial modes in a Hertzsprung-Russell diagram. The leftmost diagram shows MS models, the diagram in the middle models in the post-MS contraction phase and the rightmost diagram models in the post-MS expansion phase. A representative evolutionary track is shown for each evolutionary stage. The photometric error box is given.

Even though a wide range of input parameters was used, the models are restricted to three distinct small regions in the HR diagram. While most of the models in the post-main sequence expansion phase are located inside the photometric error box, main sequence models fit the radial modes at significantly lower effective temperatures. Post-main sequence models in the contraction phase are more widespread in the diagram.

After this rather quantitative examination we will now restrict our investigations to the standard chemical composition of $X=0.70$ and $Z=0.02$. Since the rotation rate as well as abundances of 44 Tau are known, this star represents a good testing object to evaluate the impact of the choice of different element mixtures or opacity tables. As these effects are similar in every possible evolutionary stage, the impact will be examined only for the case of a post-MS model in the expansion phase.

4.2.2 Effect of different solar element mixtures on the radial period ratio

As discussed in section 4.1 the abundance pattern of 44 Tau does not show a preference for the GN93 or A04 element mixtures. Hence it is interesting to test whether the asteroseismic models of 44 Tau point to a favored element mixture.

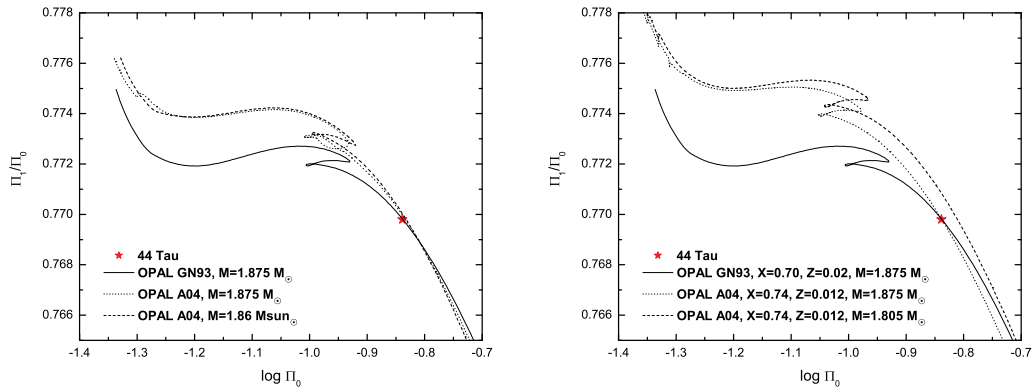


Figure 4.7: Effect of different element mixtures on the radial period ratio. Left panel: comparison of the results obtained with the GN93 and A04 mixture for constant metallicity ($Z=0.02$). Right panel: comparison of the results using the suggested solar value of Z for each mixture.

The Petersen diagrams in Figure 4.7 present the results considering two cases: in the left panel the period ratios computed with the GN93 and A04 element mixture are compared for the same metallicity of $Z=0.02$. The effect shown here is only the effect of changing the abundance mixture. With A04 the period ratio during the main sequence stage is predicted to be higher but it decreases more strongly during the post-main sequence evolution. A slightly lower mass is needed to fit the observed radial period ratio of 44 Tau.

However, $Z=0.02$ for the A04 mixture corresponds to a metal overabundance in comparison to the Sun. For the A04 element mixture the solar chemical composition was

determined to be $X=0.74$ and $Z=0.012$. In the right panel of Figure 4.7 the results obtained with the suggested solar composition for each mixture are given. The effect is larger as in the previous case. To fit the observed periods the mass has to be decreased from 1.875 to $1.805 M_{\odot}$. Figure 4.8 shows how this change affects the position of the models that fits the observed radial modes in the HR diagram. Both models are in satisfactory agreement with the photometric error box. The parameters of the models obtained in this section are given in Table 4.4.

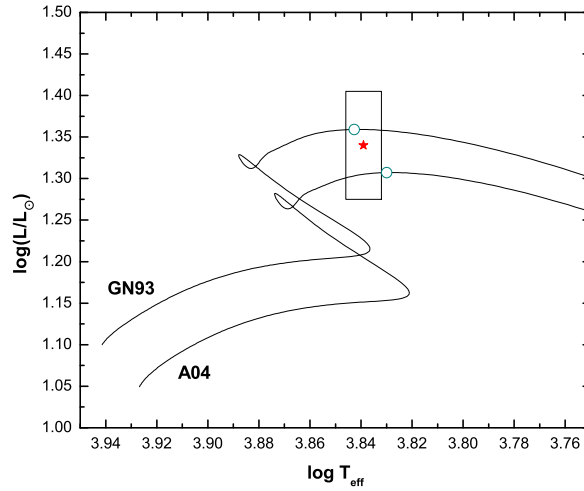


Figure 4.8: Comparison of evolutionary tracks obtained with the GN93 element mixture using $X=0.70$, $Z=0.02$ and the A04 mixture adopting $X=0.74$ and $Z=0.012$.

Opacity	Element mixture	X	Z	M/M_{\odot}	$\log T_{\text{eff}}$	$\log L/L_{\odot}$	$\log g$	Age [Myr]
OPAL	GN93	0.70	0.02	1.875	3.8422	1.3601	3.6712	1120
OPAL	A04	0.70	0.02	1.860	3.8313	1.3070	3.6767	1250
OPAL	A04	0.74	0.012	1.805	3.8303	1.3035	3.6635	1330

Table 4.4: Comparison of the parameters of models obtained with different element mixtures.

For all models rather inefficient convection ($\alpha_{\text{MLT}} = 0.2$) and no overshooting from the convective core were assumed. The main effect of changing the element mixtures is a small modification of the opacities in the model. The results given in this section were obtained with the OPAL opacities. Using a different source of opacity data may, therefore, also have an influence on the period ratio. This will be tested in the next section.

4.2.3 Effect of different opacity data on the radial period ratio

As shown in section 2.4.3, the Rosseland-mean opacities given by the Lawrence Livermore Laboratory and the Opacity Project team exhibit small differences. Since opacity data are very important for asteroseismic studies we tested the effect of using different opacity sources on the predicted radial period ratio. As can be seen in Figure 4.9 the results are striking.

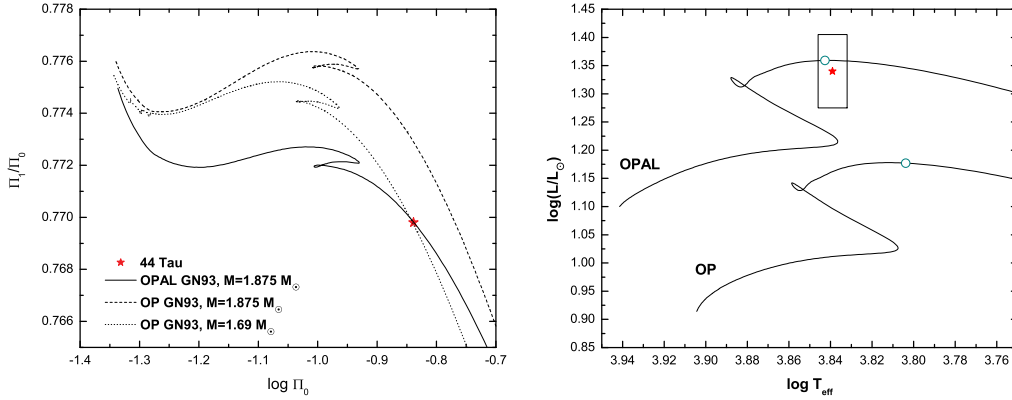


Figure 4.9: Comparison between results obtained from OPAL and OP opacities. Left panel: the influence of opacity tables in the Petersen diagram. Right Panel: Position of models that fit the radial period ratio in the HR diagram.

With OP opacities the predicted radial period ratio is much higher compared to that in the OPAL case. The differences in the opacity lead to a different sound speed in the stellar model. The periods of the pulsation modes are, therefore, also modified. To fit the observed radial modes in 44 Tau the mass has to be reduced from 1.875 to 1.69 M_\odot . Due to this low mass, the model that fits both radial modes is situated far outside the photometric error box. The fundamental parameter of the OPAL and the OP model are given in Table 4.5.

Opacity	Element mixture	X	Z	M/M_\odot	$\log T_{\text{eff}}$	$\log L/L_\odot$	$\log g$	Age [Myr]
OPAL	GN93	0.70	0.02	1.875	3.8422	1.3601	3.6712	1120
OP	GN93	0.70	0.02	1.695	3.8052	1.1822	3.6571	1520

Table 4.5: Comparison of the parameters of models calculated with different opacity data.

It is necessary to examine these results in more detail. Figure 4.10 shows the Rosseland mean opacity for the OPAL model given in the Table 4.5. Moreover, for the temperature structure of the OPAL model, the OP opacities are evaluated to allow a direct comparison of the differences in opacity. It can be seen that the relative differences are below 15%.

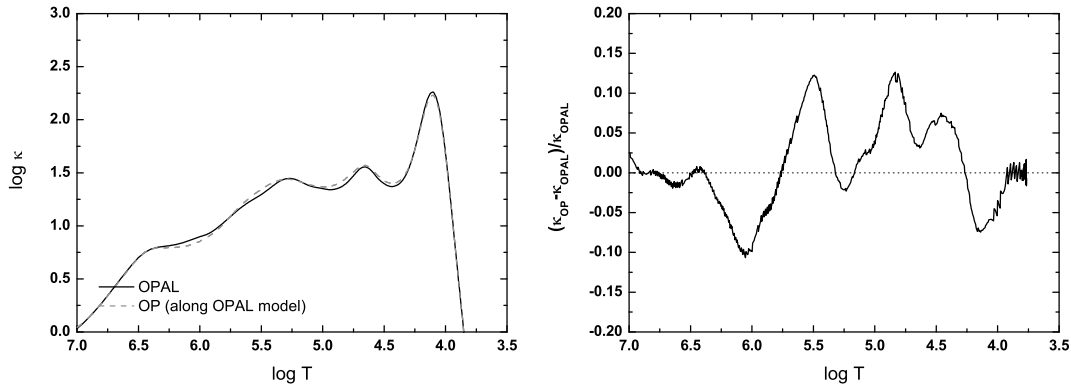


Figure 4.10: Left panel: Rosseland mean opacity for the OPAL model compared to the OP opacities evaluated for the temperature structure of the OPAL model. Right panel: relative differences between the two opacity data.

Due to the differences between the opacities the radial modes do not fit the observed period ratio if the OP model is evaluated for the structure of a model originally computed with OPAL opacities. Let us now compare the OPAL model with an OP model that actually fits the radial modes. As shown in Figure 4.11 the differences between the opacities in the $1.875 M_{\odot}$ OPAL model and the $1.695 M_{\odot}$ OP model very large.

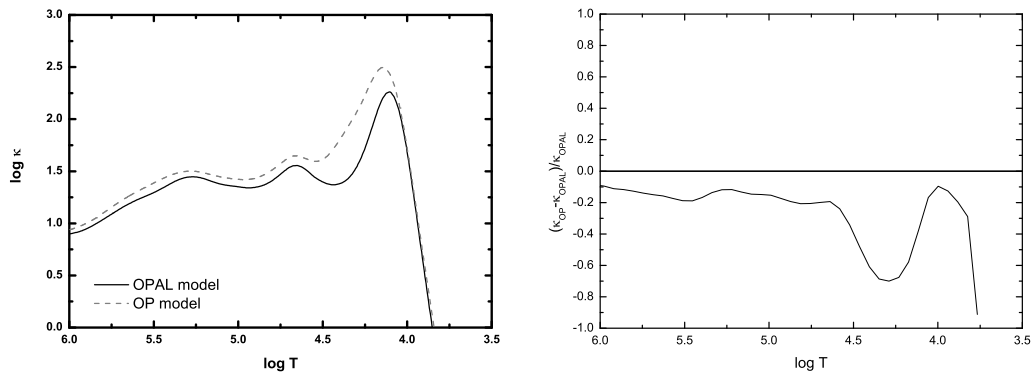


Figure 4.11: Rosseland mean opacity for the OPAL and OP model that fit the radial modes (left panel). Right panel: relative differences between the two opacity data.

We examined the differences between the opacities to find the reason for the large differences when fitting the radial fundamental and the first overtone. In particular the question arises whether the differences are created due to opacity deviations in a restricted range in temperature or not.

We computed Rosseland mean opacities for OPAL and OP data for a chemical composition with $X=0.70$, $Z=0.02$ using the GN93 element mixture. Figure 4.12 shows the

comparison between the two data sets. The mean opacities are in general very similar and at certain temperatures the values are even equal. In the diagram these temperatures ($\log T=4.263, 4.625, 5.146, 5.308, 5.725, 6.332, 6.745$ [K]) are marked with vertical lines. The relative differences in opacity are similar as in Figure 4.10.

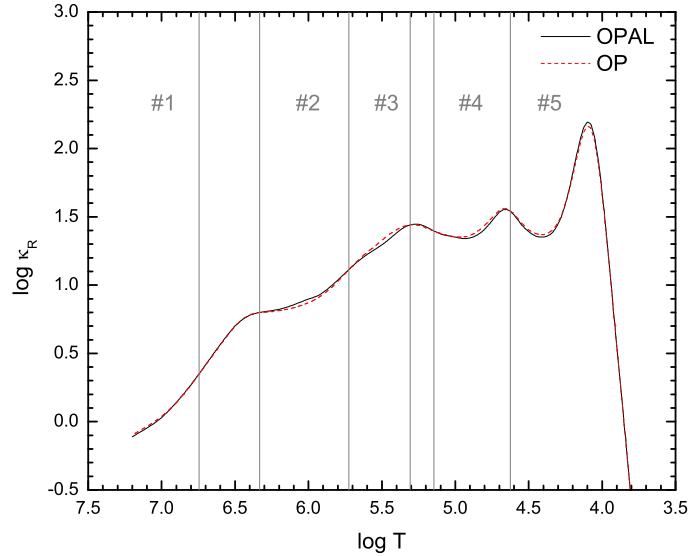


Figure 4.12: OPAL and OP mean opacities for $X=0.70$, $Z=0.02$. Vertical lines mark some of the temperatures at which the OPAL and OP opacities are equal. Different temperature regions are marked with labels.

For testing purposes, it is feasible to exchange opacity data between equal-opacity temperatures and to create an artificial opacity set which is a mixture between the OPAL and the OP opacities. In this context it is crucial to make sure that the resulting $\log \kappa$ and its derivative have no discontinuities. The influence on the models that fit the radial fundamental and first overtone in the HR diagram is then examined.

As we know from history, radiative opacities were increased step-by-step. Hence in the first test the maximum value of $\log \kappa_{\text{OPAL}}$ or $\log \kappa_{\text{OP}}$ was used to create the new opacity data set with its corresponding derivatives. Then we tested how these new opacity data influence the fit of the observed radial modes. As can be seen in the left panel of Figure 4.13, using only the highest opacity values from both sources results in a model in-between the pure OPAL or OP case. Similar results are found when only the smallest opacity values are considered (the corresponding model is denoted as 'min' in Figure 4.13). Since these results do not fully explain the differences between the OPAL and OP results a more detailed investigation is necessary.

The next test was to examine whether specific temperature regions are responsible for the difference between the OPAL and OP models. The chosen method was to exchange the opacity data in-between the opacity-equality points for each of the temperature regions

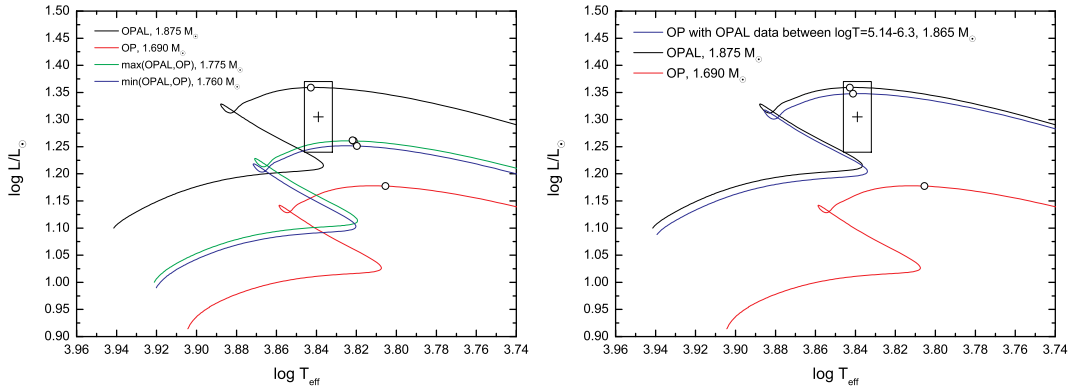


Figure 4.13: HR diagram showing the influence of the adopted artificial opacity data on the models which fit the observed radial modes in 44 Tau. See text for details.

labeled in Figure 4.12. The results of this test are that the opacity in the temperature regions #2 and #3 have the main responsibility for the different results between OPAL and OP in the case of 44 Tau. Thus if the OP opacities are replaced with OPAL data in the temperature region between $\log T = 5.15$ and 6.33 , the radial fundamental and the first overtone can be fit at a similar position in the HR diagram as in the pure OPAL case (see right panel in Figure 4.13). The mass of this model is $1.865 M_{\odot}$, which is only slightly lower as for the pure OPAL case.

The difference of OPAL and OP opacity in the temperature region $\log T = 5.15$ and 6.33 is therefore important for the period ratio between the radial fundamental and first overtone. This is in agreement with Petersen & Jørgensen (1972) who stated that the fundamental mode has the highest weight around $x=r/R=0.7$ which corresponds to the same temperature region considered here. Figure 4.14 shows the kinetic energy density of the radial fundamental and first overtone mode inside the star. Pulsation modes are sensitive to the conditions in temperature regions in which the kinetic energy density is high. Due to the position of its node the radial first overtone mode probes the temperature region between $\log T = 4.5$ and 7.0 with different weights than the radial fundamental mode. This explains our findings above.

As shown in the third panel in Figure 4.14 the OP opacities are lower by approximately 10% around $\log T = 6.05$ in comparison with OPAL. This is the main reason for the different results between OP and OPAL and was also noted by Montalbán & Miglio (2008). These authors artificially increased the OPAL opacities by 5% around $\log T \sim 6.25$ and could fit the observed period ratio with a main sequence model with 1.9 solar masses and $\alpha_{ov} = 0.3$ using the standard chemical composition of $X=0.70$, $Z=0.02$ (see Figure 5 in that paper). Consequently, this may indicate that the OP data underestimate the true opacity in the temperature region around $\log T = 6.05$.

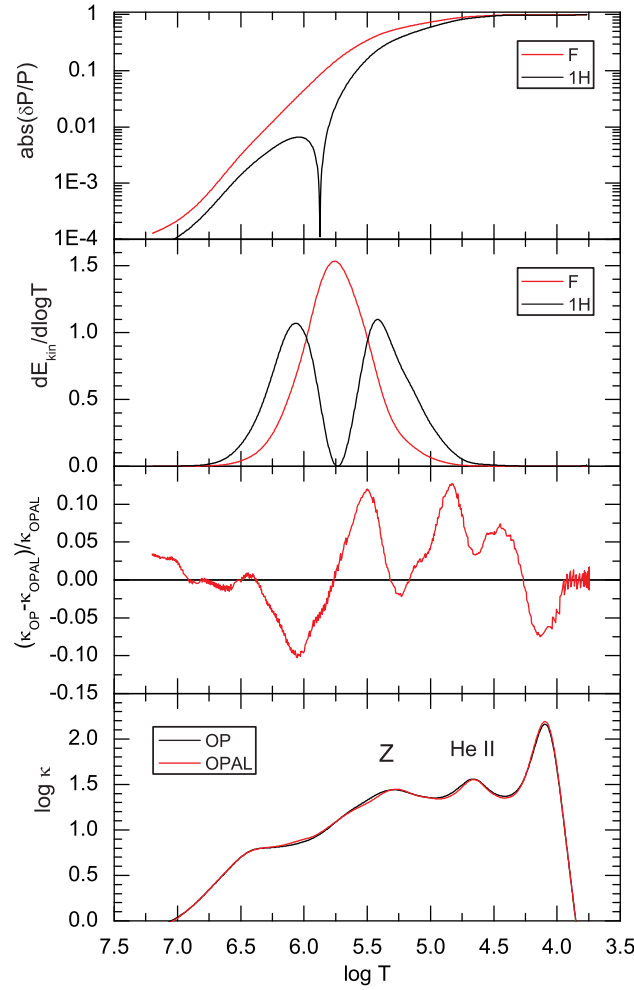


Figure 4.14: The radial fundamental and first overtone mode as a probe for opacity data. Uppermost panel: relative Lagrangian pressure variation. Second panel: kinetic energy density inside the star. Third panel: comparison between OPAL and OP opacities for the same model. Lowest panel: absolute values of Rosseland mean opacities from OPAL and OP data.

4.2.4 Effect of the CEFF equation of state on the period ratio

To check for the influence of the equation of state on the models and the period ratio we performed additional tests with the CEFF equation of state (Christensen-Dalsgaard & Däppen 1992). Since the conditions in the interior of post-MS expansion models are partly outside the parameters of the CEFF equation of state, these tests were only performed for an MS model of 44 Tau.

The reference model was constructed with the OPAL opacities, the GN93 element mixture and a standard chemical composition ($X=0.70$, $Z=0.02$). The mixing-length parameter

of convection was set to $\alpha_{\text{MLT}}=0.2$ and a convective overshooting parameter of $\alpha_{\text{ov}}=0.4$ was used. With such a configuration a nonrotating model with $1.850 M_{\odot}$ reproduces the observed period ratio.

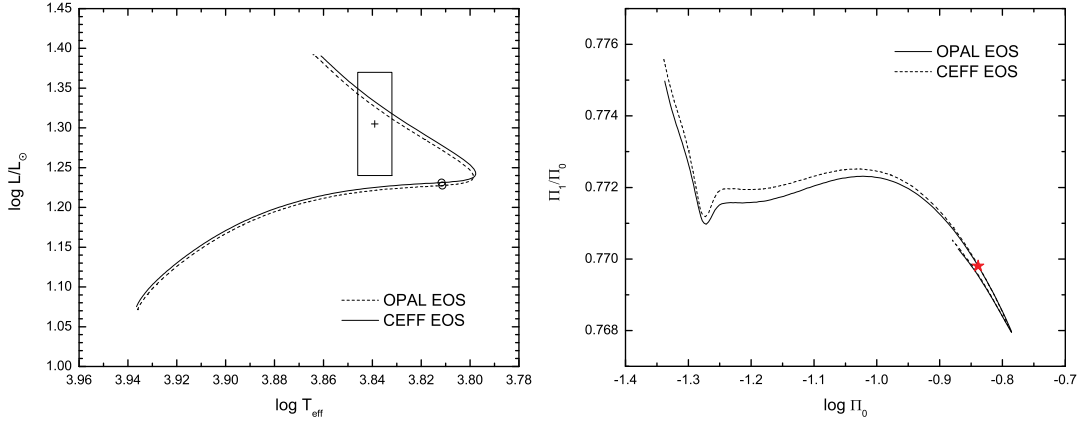


Figure 4.15: Comparison between the results obtained with the CEFF and OPAL equation of state in the HR diagram (left panel) and the Petersen diagram (right panel). See text for model parameters.

With the same input parameters a model with the CEFF equation of state was computed. Figure 4.15 compares the results for the OPAL and the CEFF models. As can be seen in the HR diagram, the differences in effective temperatures and luminosities are small. The effect on the radial period ratio is slightly larger, especially in the early phases of main sequence evolution. Close to the TAMS the differences between the period ratios diminish. Since the observed radial periods put 44 Tau near the TAMS, the choice of the equation of state appears to be of less importance. As the computation of models with the CEFF equation of state is very time consuming, we rely on the OPAL equation of state in the remaining parts of this work.

4.3 Main sequence models

In section 4.2.3 we showed that OPAL opacities reproduce the observed fundamental parameters of 44 Tau much better than the OP opacities. We will now examine the OPAL models in more detail. In Figure 4.6 the location of main sequence models in the HR diagram was already shown.

One of the general arguments in favor of main sequence models is that the time spent to cross the photometric box is approximately 5 times larger compared to a post-main sequence model which also fits both radial modes. It is therefore more likely that we observe the star in the core hydrogen burning phase.

Main sequence models which fit the period ratio of 44 Tau can only be obtained if one assumes overshooting from the convective core. Otherwise the hydrogen in the core is

depleted before the overall density and correspondingly the predicted frequencies decrease to sufficiently low values to fit the radial modes to the observed values.

Since a change of metallicity shifts the position of the evolutionary track in the HR diagram due to the change of mean opacity, the minimum size of the overshoot layer depends on metallicity. Table 4.6 lists the minimum overshooting parameter α_{ov} for different adopted metallicities:

Z	$\alpha_{ov,min}$	Mass [M_{\odot}]
0.015	0.38	1.737
0.019	0.28	1.828
0.020	0.25	1.849
0.021	0.23	1.867
0.025	0.16	1.935

Table 4.6: Minimum overshooting parameter to fit f_1 and f_5 as radial modes.

The mass given in this table results from fitting both radial modes. The adopted hydrogen mass fraction was $X=0.70$. For a few main sequence models the hydrogen content was changed to $X=0.75$ and 0.65 for testing purposes. This adjustment shifts the position of the evolutionary tracks in the HR diagram to higher or lower luminosity, respectively. High values for the hydrogen mass fraction are favorable to reduce the discrepancy in luminosity between theoretical models and the photometric box. However, the large offset in effective temperature remains.

Hitherto we only discussed the fit of radial modes, which are sensitive to the global parameters of the star. Nonradial modes probe different layers of the star and, therefore, are an important asteroseismic diagnostic. For the family of models that reproduce the observed radial period ratio, the corresponding $\ell=1$ and $\ell=2$ modes were computed and compared to the observations. The frequency separation between the two observed dipole modes at 9.11 cd^{-1} and 9.56 cd^{-1} is closer than the common spacing between pure acoustic $\ell=1$ modes. Consequently, an avoided crossing between an acoustic and a gravity mode is observed (Aizenman et al. 1977).

The phenomenon of avoided crossings is also known as mode bumping. The reason for this term becomes more clear when the evolution of the frequencies from the ZAMS to the TAMS is examined. Figure 4.16 shows the change of the theoretical frequencies due to evolutionary structural changes for dipole and quadrupole modes. Since the gravity modes are sensitive to the conditions in the stellar core the occurrence of an avoided crossing critically depends on the overshooting assumed in the model. This poses an additional strong constraint to the pulsation model. By changing the overshooting parameter, α_{ov} , the fit of the $\ell=1$ modes that undergo an avoided crossing can be optimized for a given metallicity, Z.

As shown in Figure 4.17 a good fit of the observed dipole modes can be achieved. The parameters of this model are given in Table 4.7. Comprehensive additional model

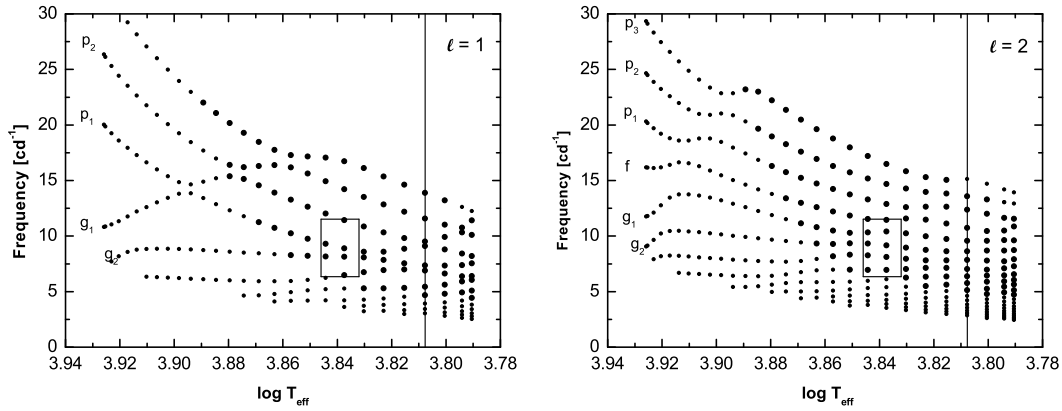


Figure 4.16: Change of dipole and quadrupole mode frequencies during the evolution from the ZAMS to the TAMS in a main sequence model. The observed temperature and frequency domain are indicated with a box. The vertical line marks the effective temperature which allows the fit of the observed avoided crossing of dipole modes.

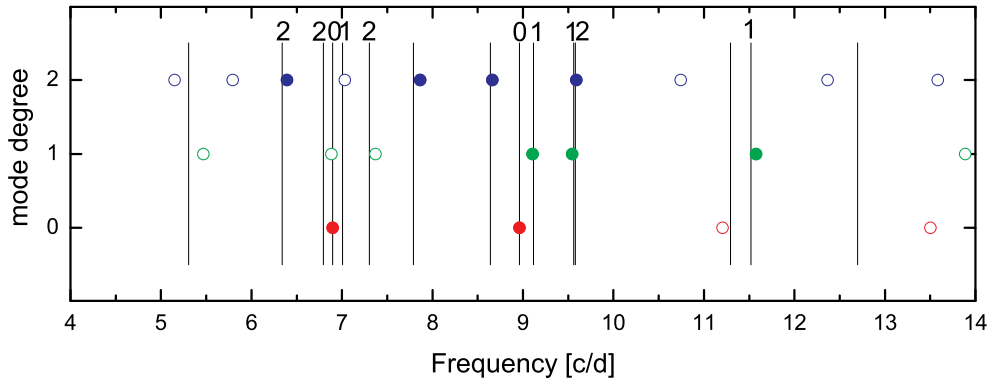


Figure 4.17: Comparison between observed frequencies (vertical lines) and predicted unstable frequencies (circles) for a main sequence model. If predicted frequencies match observed frequencies they are marked as filled circles. The numbers on top of the vertical lines indicate measured spherical degrees of the modes.

computations using a wide range of input parameters were performed to improve the fit of the quadrupole modes. However, a model that simultaneously provides a good fit of both $\ell=1$ and $\ell=2$ modes could not be found. The pulsation model with the best fit was constructed with a metallicity of $Z=0.03$, which is significantly higher than the metal content indicated from photospheric element abundances.

Another important seismic constraint is the comparison between the theoretical range of unstable modes with the observed frequency range. Whether a mode is unstable or

	X	Z	α_{MLT}	α_{ov}	M/M_{\odot}	$\log T_{\text{eff}}$	$\log L/L_{\odot}$	$\log g$	Age [Myr]
MS	0.70	0.03	0.2	0.25	2.010	3.8077	1.2385	3.6848	1150

Table 4.7: Parameters of the MS model with the best fit of the observed frequencies.

stable is determined by evaluating the instability parameter η (see Section 1.1.3). $\eta = -1$ corresponds to full damping and $\eta = +1$ to full driving. The behavior of η as a function of frequency is shown in Figure 4.18 for all modes with $\ell \leq 2$ in the best main sequence model. There is excellent agreement between observations and the theoretical prediction of this model.

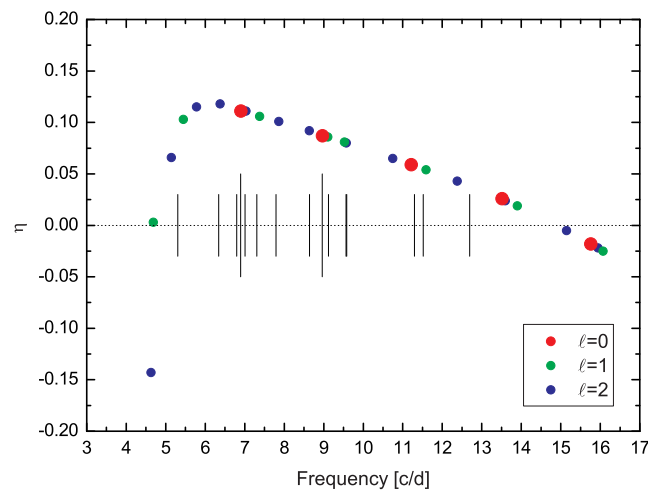


Figure 4.18: Normalized growth rate, η , as a function of mode frequency for the main-sequence model of 44 Tau. η is positive for unstable modes. The vertical lines mark the position of observed modes (with longer vertical lines for the two observed radial modes).

The predicted mode instability for a model in an advanced phase of core hydrogen burning is convincing. Is the poor fit of $\ell=2$ modes an indication that the stellar layers which are probed by the quadrupole modes are not sufficiently described by our models? And what is the reason for the discrepancy between observations and theory concerning the location of the model in the HR diagram? Before we answer these questions we should also investigate the other evolutionary stages which are possible for this star.

4.4 Post-main sequence expansion models

Seismic models that fit the observed period ratio in the post-main sequence expansion phase were already shown in Figure 4.6. Many of these models are located inside the photometric error box in the HR diagram. Despite the lower probability of observing a star in this evolutionary stage it cannot be excluded that 44 Tau is observed in just this phase of its evolution. The model parameters of the post-MS model with the best fit of the observed frequencies are shown in Table 4.8.

	X	Z	α_{MLT}	α_{ov}	M/M_{\odot}	$\log T_{\text{eff}}$	$\log L/L_{\odot}$	$\log g$	Age [Myr]
post-MS exp.	0.70	0.02	0.2	0.0	1.875	3.8422	1.3601	3.6711	1120

Table 4.8: Parameters of the post-MS model with the best fit of the observed frequencies.

Since the convective core vanishes after the end of hydrogen core burning the Brunt-Väisälä frequency increases in the center and many more g modes populate the domain of the acoustic modes. The predicted frequency spectrum of models in this phase is much denser than observed, as can be seen in Figure 4.19. This problem for evolved δ Scuti stars was already noticed by Dziembowski & Krolikowska (1990). Obviously, a mechanism is active which excites specific modes to observable amplitudes, while others remain at a low-amplitude level and may only be accessed by satellite measurements.

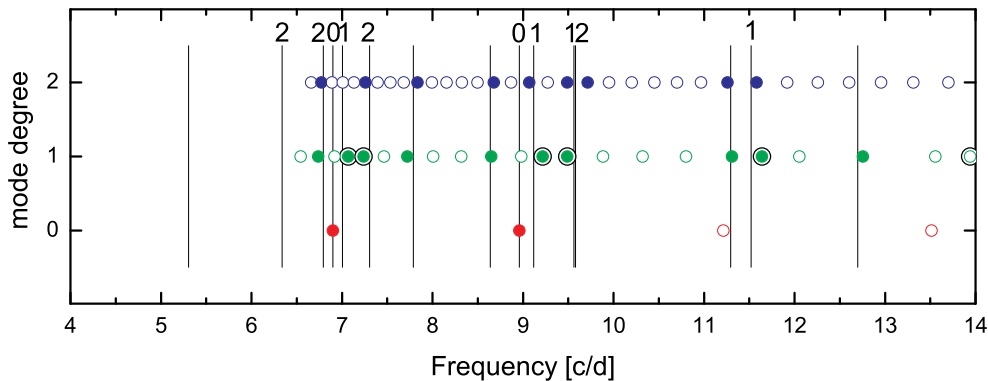


Figure 4.19: Similar to Figure 4.17 but for a model in the post-MS expansion phase. Trapped $\ell=1$ modes are surrounded with black concentric circles.

4.4.1 Mode trapping as a mechanism of mode selection

Dziembowski & Krolikowska (1990) proposed that partial trapping of modes in the stellar envelope may be a selection rule which excites specific pulsation modes to high amplitudes in δ Scuti stars. Due to a resonance effect some modes are trapped in the acoustic cavity.

The major fraction of the kinetic energy of trapped modes is concentrated in the envelope, where the density is low. As stated by Dziembowski & Krolikowska (1990) the total kinetic energy of trapped modes is lower than that of other modes. Thus they may have a higher probability to grow to observable amplitudes.

In Figure 4.20 the kinetic energy density along the stellar radius of two trapped dipole modes and one mode which is not trapped are compared. The difference is striking and clearly shows that for trapped modes more kinetic energy is confined in the envelope.

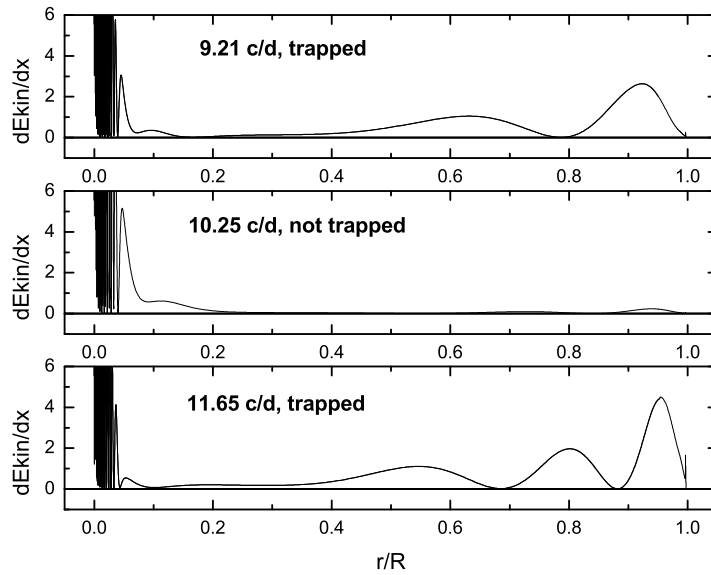


Figure 4.20: Kinetic energy density of the three $\ell = 1$ modes at 9.21, 10.25 and 11.65 cd^{-1} . Two of the modes are trapped; the third mode (middle panel) is not trapped (see Figure 4.21).

Figure 4.21 presents the fraction of kinetic energy confined in the gravitational cavity, E_g , to the total kinetic energy, E_k . Modes that are partially trapped in the envelope are located at minima in this diagram. The comparison to the observed distribution of frequencies shows a good agreement with the location of trapped dipole modes. In the theoretical frequency spectrum in Figure 4.19 the trapped $\ell=1$ modes are marked with black concentric circles.

However, Figure 4.21 also shows that mode trapping for quadrupole modes is considerably weaker than that of the $\ell=1$ and 3 modes. The observed $\ell = 2$ modes are situated at 6.34, 6.79 and 7.30 cd^{-1} . At these frequencies theory predicts no effective mode trapping while at higher frequencies the trapping of quadrupole modes is slightly more effective.

To examine the reason for the ineffective mode trapping for $\ell = 2$ modes in more detail the Brunt-Väisälä and Lamb frequencies were inspected (see Figure 4.22). The Brunt-Väisälä frequency and the Lamb frequency define the regions in a star in which a mode oscillates. As discussed in Section 1.1.2, the propagation zone for p modes is located in the

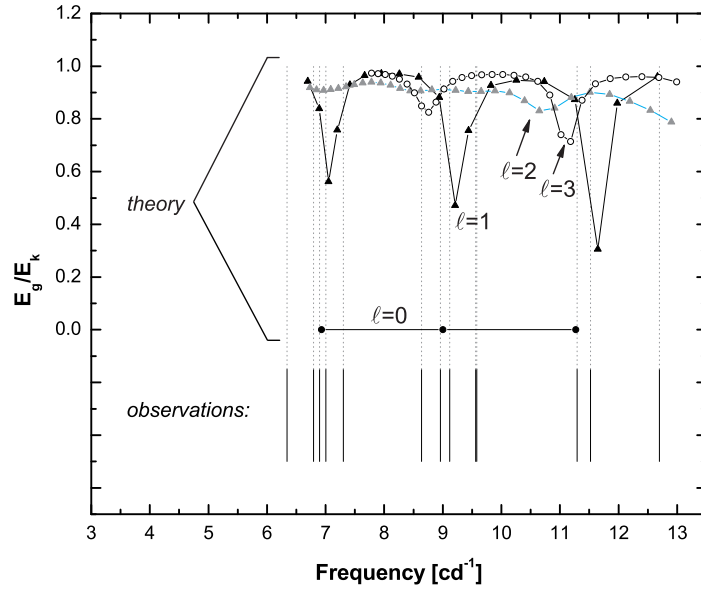


Figure 4.21: Fraction of the kinetic energy of a pulsation mode that is confined in the g mode cavity. Vertical lines indicate the position of observed modes. Modes at minima in E_g/E_k are partially trapped in the envelope.

envelope ($N^2 > \omega^2$, $L_\ell^2 > \omega^2$) and the g mode cavity in the interior ($N^2 < \omega^2$, $L_\ell^2 < \omega^2$). In between these mode cavities there is an evanescent zone in which the oscillations are damped.

The size of the evanescent zone depends on the spherical degree of the mode. For $\ell=2$ modes this zone is much smaller than for $\ell=1$ or 3 modes. The location of the observed $\ell=2$ frequencies is close to the region where essentially no evanescent zone is expected. Consequently, there is no effective trapping in the envelope for these modes.

4.4.2 Mode instability

The predicted frequency range of unstable nonradial modes for the post-main sequence expansion scenario is shown in Figure 4.23. For this model the lowest two observed frequencies (5.30 and 6.33 cd^{-1}) are predicted to be stable.

The boundaries of the instability range depend on convection. In Figure 4.24 the predicted range of unstable quadrupole modes is shown for different mixing-length parameters of convection. In the case of 44 Tau convection only has a small effect on the low-frequency boundary of the instability range but a strong effect on the high-frequency boundary. The value of the highest unstable frequency is not only sensitive to the efficiency of convection but also to the treatment of the interaction between convection and pulsation (Montalbán & Dupret 2007). Since our code relies on the simplest frozen convection assumption, it

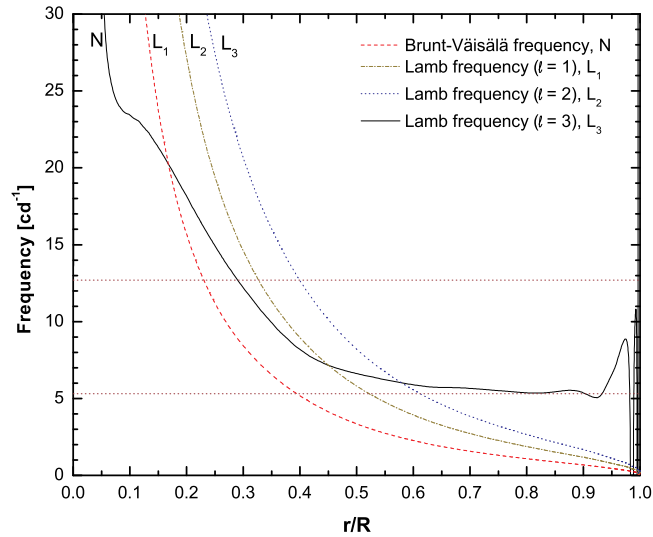


Figure 4.22: Brunt-Väisälä frequency and Lamb frequencies for different spherical degrees in a post-MS model of 44 Tau in the expansion phase. The two horizontal lines mark the lowest and highest observed frequency (6.3 and 12.7 cd^{-1}).

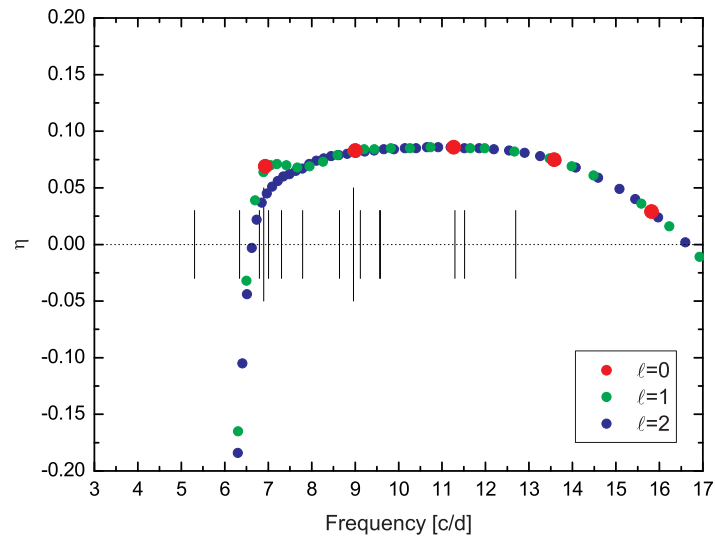


Figure 4.23: Predicted mode instability for the post-main sequence expansion case. Vertical lines mark the position of observed frequencies. Positive values for η correspond to unstable modes.

may not be suitable to accurately predict the upper limit of the frequency instability range for 44 Tau.

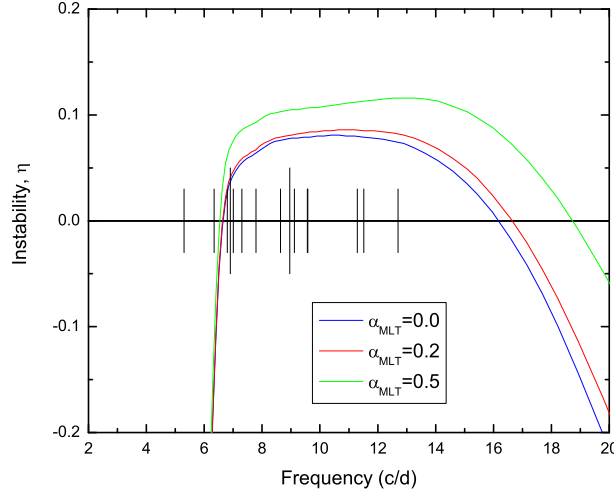


Figure 4.24: Predicted instability of $\ell=2$ modes computed for different mixing-length parameters.

Changing other input parameters of the model within reasonable amounts does not suffice to shift the predicted range to lower frequencies. One may also argue that the mode at 5.30 cd^{-1} may have a spherical degree higher than 2. However, the low-frequency boundary is similar for spherical degrees of 3 or 4. Moreover, pulsation modes with higher ℓ -values are less likely to be observed, because of cancellation effects in the integrated light curve.

Another uncertainty of the boundaries of the frequency range of unstable modes may originate from uncertainties in opacity data. Adjustments in the opacity can also lead to instability for modes at lower frequencies, however, the required changes may be too big to be physically meaningful.

Consequently, despite the good fit of the fundamental parameters, pulsation models in the post-main sequence expansion phase do not sufficiently explain the observed frequency spectrum and mode instability.

4.5 Post-MS contraction models

In this section we will examine models in the overall contraction phase after the TAMS. The evolution during the contraction phase is approximately 10 times faster compared to the main sequence evolution of the same model in the same range of effective temperatures.

Similar to the main sequence case the observed avoided crossing of dipole modes puts strong constraints on the models and in particular on convective overshooting. A first model was computed with standard chemical composition, OPAL opacities and GN93 element

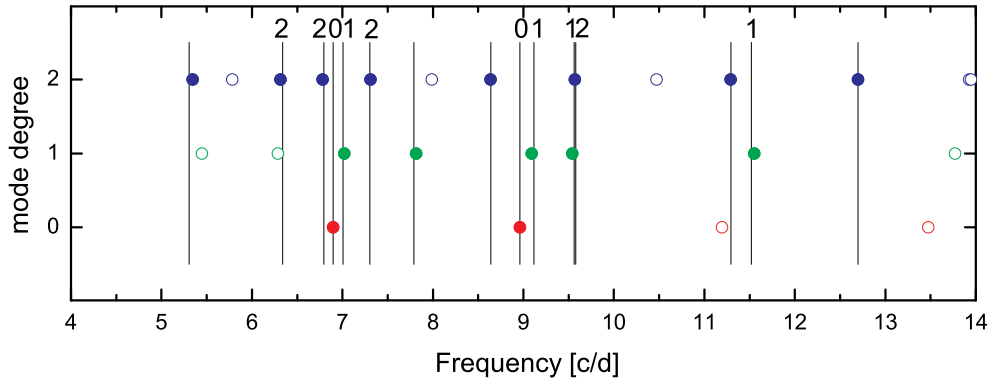


Figure 4.25: Comparison between observed frequencies (vertical lines) and predicted unstable frequencies (circles) for a post-MS contraction model (Model 1). If predicted frequencies match observed frequencies they are marked as filled circles. The numbers on top of the vertical lines indicate the measured spherical degrees of the modes.

abundances. The overshooting parameter was adjusted to fit the observed avoided crossing of dipole modes. The model which provided a good fit of the two radial modes and all four dipole modes, also exhibited a good agreement between observed and predicted quadrupole modes. By adjusting the hydrogen mass fraction to a higher value of $X=0.75$ an even better fit of the avoided crossing could be achieved.

A comparison between the observed and the predicted frequency spectrum for this model is shown in Figure 4.25. It can be seen that there is an excellent fit between observed and predicted modes and that the pulsation model explains all observed modes with $\ell \leq 2$. In a few cases $\ell = 3, 4$ frequencies are also close to observed values but photometric cancellation effects clearly favor low degree modes. The parameters of this model can be found in Table 4.9 (Model 1).

The theoretical frequency range of unstable modes is also in good agreement with the observed frequency range as shown in Figure 4.26. The model also predicts mode instability between 13 and 18 cd^{-1} . However, this is not a serious problem as this may be due to an overestimation of mode instability in this frequency region by our codes, as discussed in Section 4.4.2. Due to our use of the frozen convective flux approximation the high-frequency border between unstable and stable modes is subject to uncertainty.

As shown in Figure 4.27 the predicted effective temperature of this post-main sequence contraction model is cooler than the value derived from photometry. However, the standard deviation of the measured effective temperature is 100 K which may be optimistic. The predicted luminosity is in excellent agreement with the values derived from Hipparcos.

The excellent fit of the individual frequencies, the instability range and the good agreement of the fundamental parameters allow us to conclude that 44 Tau is in the overall contraction phase after the main sequence phase.

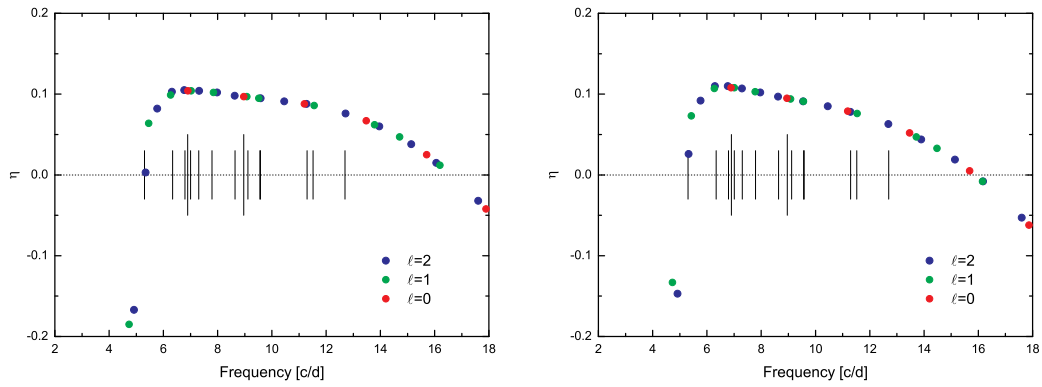


Figure 4.26: Instability parameter, η , for Model 1 (left panel) and Model 3 (right panel). Positive values indicate mode driving, modes with negative η are damped.

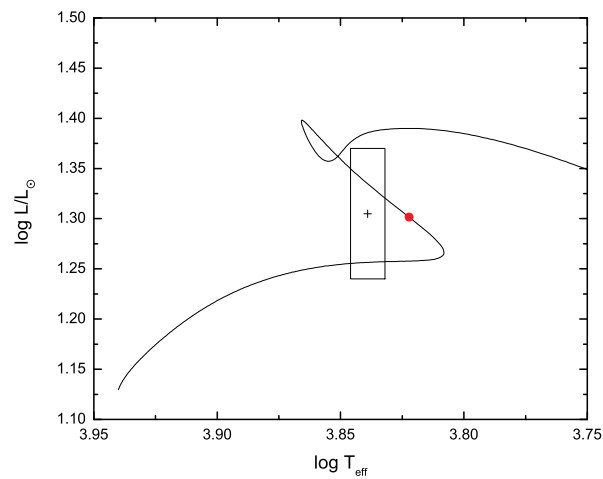


Figure 4.27: Position of Model 1 in Table 4.9 in the HR diagram.

4.6 Mixed modes as probes of the stellar core region

The partial mixing processes at the convective core boundary are still not fully understood. During the hydrogen core burning we expect a region around the convective core that is partially mixed due to several mechanisms: (i) overshooting from the convective core, (ii) rotationally induced mixing (the core rotates faster than the envelope leading to additional mixing, and (iii) higher opacity close to the boundary of convective core (leading to a larger convective core).

Unfortunately, until now no rotational splittings could be detected in 44 Tau. Therefore, we cannot derive the profile of differential rotation which would be necessary to disentangle the effects of rotation in element mixing.

An excellent probe of the size of the overshoot layer is the g_1 mode for $\ell > 0$ as stated by Dziembowski & Pamyatnykh (1991). This mode is partially trapped in the overshoot region and, therefore, its frequency is of high diagnostic value. In 44 Tau models in the contraction phase after the TAMS this mode already moved to higher frequencies outside the observed frequency range. However, the frequencies of mixed acoustic and gravity modes are also expected to be sensitive to the conditions in the stellar core and can be used to examine the partially mixed region above the convective core.

Aside from the traditional description of overshooting from the convective core we also applied a new two-parametric description that allows for partial element mixing in the overshooting region (Dziembowski & Pamyatnykh 2008). It allows us to consider different profiles of the hydrogen abundance inside the partly mixed region just above the convective core. To find the optimum fit for the nonradial modes a series of computations with different overshooting distances, α_{ov} , and w was made. Since the predicted frequencies also depend on the hydrogen content available for mixing we also tested different values for the initial hydrogen mass fraction, X . The best pulsation models for the GN93 and A04 element mixtures are given in Table 4.9. Again, an increased initial hydrogen mass fraction produces better fits to the observed frequencies.

The positions of the models listed in Table 4.9 in the HR diagram is shown in Figure 4.28 for the models computed with the GN93 element mixture and in Figure 4.29 for models with the A04 mixture. The effective temperatures of the pulsation models are generally cooler than photometric and spectroscopic measurements indicate.

The pulsation models obtained with A04 are closer to the TAMS than the models computed with GN93. A 15-frequency fit with $w=2.0$ is not possible, because the required overshooting distance should be smaller than possible for post-MS models. The main reason for the differences between pulsation models obtained with the GN93 vs. A04 mixture is the different opacity in the overshooting region which affects the size of the convective core. The uncertainties in the element abundances in 44 Tau therefore lead to an uncertainty in the determination of the overshooting distance α_{ov} .

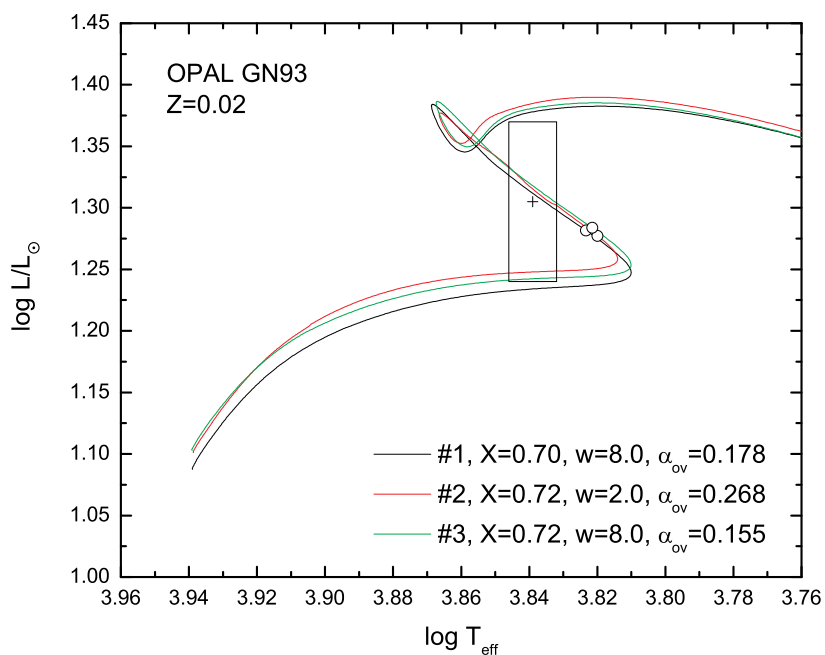


Figure 4.28: HR diagram with evolutionary tracks for models with a good fit of the 15 observed modes, constructed with OPAL opacities and the GN93 element mixture.

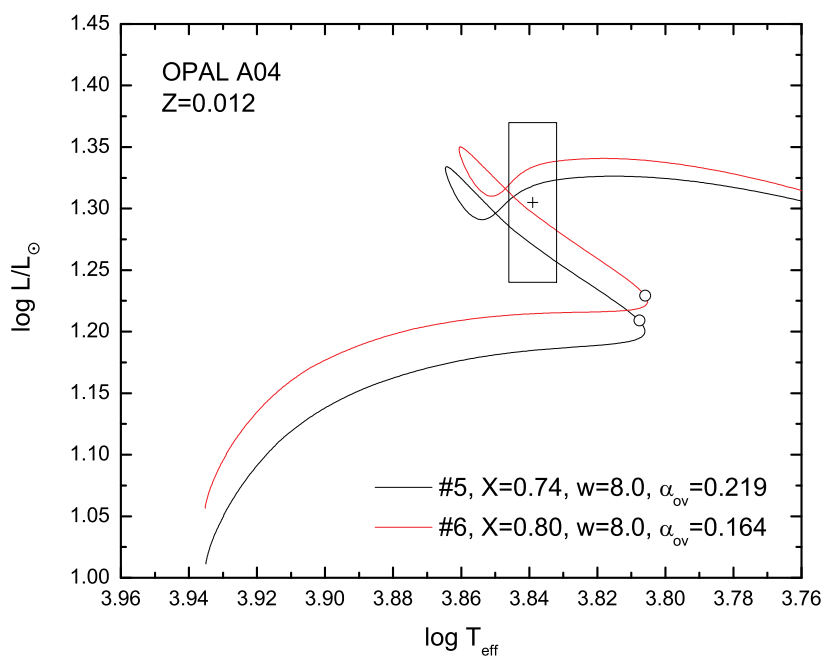


Figure 4.29: HR diagram with evolutionary tracks for models with a good fit of the 15 observed modes, constructed with OPAL opacities and the A04 element mixture.

No.	Opacity	El. mixture	X	Z	M [M_{\odot}]	w	α_{ov}	$\log T_{eff}$	$\log L/L_{\odot}$	$\lg g_{eff}$
1	OPAL	GN93	0.75	0.02	2.021	-	0.195	3.8220	1.3016	3.6823
2	OPAL	GN93	0.72	0.02	1.920	2.0	0.268	3.8200	1.2773	3.6753
3	OPAL	GN93	0.72	0.02	1.922	8.0	0.155	3.8215	1.2839	3.6749
4	OPAL	GN93	0.70	0.02	1.860	8.0	0.178	3.8225	1.2777	3.6707
5	OPAL	A04	0.74	0.012	1.783	8.0	0.219	3.8077	1.2091	3.6621
6	OPAL	A04	0.80	0.012	1.958	8.0	0.164	3.8060	1.2292	3.6760
7	OP	GN93	0.70	0.02	1.678	8.0	0.212	3.7784	1.0711	3.6561
8	OP	GN93	0.75	0.02	1.800	8.0	0.166	3.7740	1.0745	3.6660

Table 4.9: Parameters for post-MS contraction models with a good fit of the 15 frequencies observed in 44 Tau. All models were computed for a mixing-length parameter, $\alpha_{MLT}=0.2$. Starting with an initial rotation rate of 3.5 km s^{-1} and assuming uniform rotation the tabulated evolved models exhibit rotation rates close to 3 km s^{-1} . Model 1 was computed with the traditional description of overshooting.

Theoretical frequencies and other properties of unstable modes predicted by Model 3 are listed in Table 4.10. The differences between observed and calculated frequencies are given. If the azimuthal order of an observed mode is unknown the frequency difference to the theoretical $m=0$ modes is given and the corresponding value is enclosed by brackets. The uncertainty in frequency due to unknown azimuthal order may be as high as 0.05 cd^{-1} for $\ell = 2$ modes.

We observe many mixed modes in 44 Tau which are also sensitive to the conditions in the chemically inhomogeneous overshoot layer above the convective core. Table 4.10 lists the fraction of oscillation kinetic energy confined in the g mode cavity for all predicted unstable modes in Model 3. Since the given values are very similar for the different OPAL and OP models they can be considered representative for all post-MS contraction models.

The mixed $\ell=1$ mode at 7.79 cd^{-1} has strong g mode characteristics. Almost 87% of its kinetic energy is confined in the g mode cavity in the stellar interior. This also explains why the observed amplitude of this mode is significantly smaller than that of other dipole modes in 44 Tau. Consequently, this and other mixed modes are sensitive to the shape of the hydrogen profile in the partially mixed layer above the convective core.

In Figure 4.30 we compare the predicted frequency spectra for Model 2 and Model 3 (obtained with $w=2.0$ and $w=8.0$, respectively). As can be seen, modes with dominant gravity behavior have slightly different frequencies in these models. The frequency of the g_4 mode at 7.79 cd^{-1} shifts most significantly. The results shown in Figure 4.30 suggest preference for more efficient mixing in a small partially mixed region ($w=8.0$) over less efficient mixing in a larger partially mixed region ($w=2.0$).

The profile of the hydrogen mass fraction for the fitted pulsation model is given in the upper panel of Figure 4.31. In the middle panel the corresponding Brunt-Väisälä frequency in the core region is shown. In the lower panel the eigenfunction of the relative Lagrangian pressure variation is given for the mixed $\ell = 1$ modes: g_4 at 7.79 cd^{-1} and p_1 at 7.01 cd^{-1} .

Mode ℓ	ID	ν_{model} cd^{-1}	ν_{observed} cd^{-1}	$\nu_{\text{observed}} - \nu_{\text{model}}$ cd^{-1}	E_g/E_k
0	F	6.8980	6.8980	0.0000	0.0
0	1H	8.9607	8.9606	-0.0001	0.0
0	2H	11.20	-	-	0.0
0	3H	13.48	-	-	0.0
1	g ₆	5.44	-	-	0.96
1	g ₅	6.29	-	-	0.92
1	p ₁	7.0342	7.0060	-0.0282	0.13
1	g ₄	7.7915	7.7897	(-0.0018)	0.87
1	p ₂	9.1099	9.1174	0.0075	0.35
1	g ₃	9.5748	9.5611	(-0.0137)	0.61
1	p ₃	11.5526	11.5196	-0.0330	0.04
1	p ₄	13.74	-	-	0.19
1	g ₂	14.51	-	-	0.75
2	g ₁₀	5.3375	5.3047	(-0.0328)	0.96
2	g ₉	5.78	-	-	0.93
2	g ₈	6.3076	6.3390	(0.0314)	0.83
2	g ₇	6.7795	6.7955	0.0160	0.68
2	f	7.3023	7.3031	0.0008	0.67
2	g ₆	7.98	-	-	0.74
2	p ₁	8.6401	8.6391	-0.0010	0.64
2	g ₅	9.5584	9.5828	(0.0244)	0.62
2	p ₂	10.47	-	-	0.57
2	g ₄	11.3129	11.2947	(-0.0182)	0.60
2	p ₃	12.7043	12.6915	(-0.0128)	0.34
2	g ₃	13.92	-	-	0.04
2	p ₄	15.17	-	-	0.35

Table 4.10: Theoretical frequencies of $m=0$ modes predicted by Model 3 listed in Table 4.9.

Due to its larger eigenfunction in the partially mixed region the gravity mode is more sensitive to the conditions in this region.

4.7 Predictions of the post-MS contraction model

Post-MS contraction models of 44 Tau predict a few additional dipole and quadrupole modes which are currently not observed. After fitting the observed 15 modes, the frequencies of the remaining modes no longer strongly depend on the input parameters. However, small deviations may be found especially for g modes which will provide additional constraints on mixing in the overshoot layer. The expected frequencies of hitherto not observed modes can be found in Table 4.9. The detection of these modes would help to refine our models.

A reexamination of our photometric data indeed shows a prominent peak at the predicted position of the second radial overtone (11.198 cd^{-1}). This peak has a SNR below the significance limit 4.0 but may be confirmed with additional data. A reexamination of radial

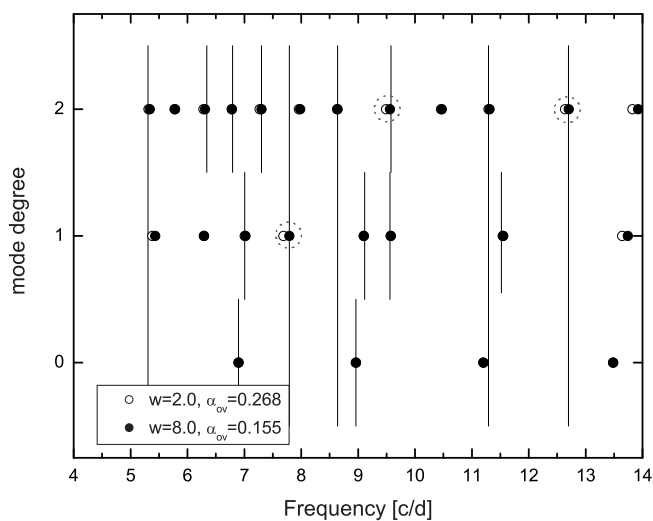


Figure 4.30: Theoretical mode frequencies of two models with different hydrogen-profile modeling, $w=8.0$ and $w=2.0$, are compared. Vertical lines indicate observed modes. The position of these lines corresponds to the detected spherical degree of the given modes. Modes sensitive to the different modeling of the partially mixed layer above the convective core are surrounded with dotted circles.

velocity data by Wolfgang Zima did not show reliable prominent peaks at the predicted positions of modes (private communication). Many of the predicted modes which lack an observational counterpart are gravity modes for which we expect only low amplitudes. Therefore, more accurate data are needed to extract these frequencies.

Moreover, the model predicts the spherical degree of some of the observed modes: $\ell = 1$ for 7.79 cd^{-1} and $\ell = 2$ for $5.30, 8.64, 11.30, 12.69 \text{ cd}^{-1}$. These predictions also need to be confirmed by high-resolution spectroscopic data.

In the contraction phase the frequencies of the modes change faster than in the main sequence phase. The computed evolutionary period changes, $(1/P)dP/dt$, are approximately $1 \cdot 10^{-8} \text{ yr}^{-1}$. Such changes are too small to be measured with the five-year time-base of our data.

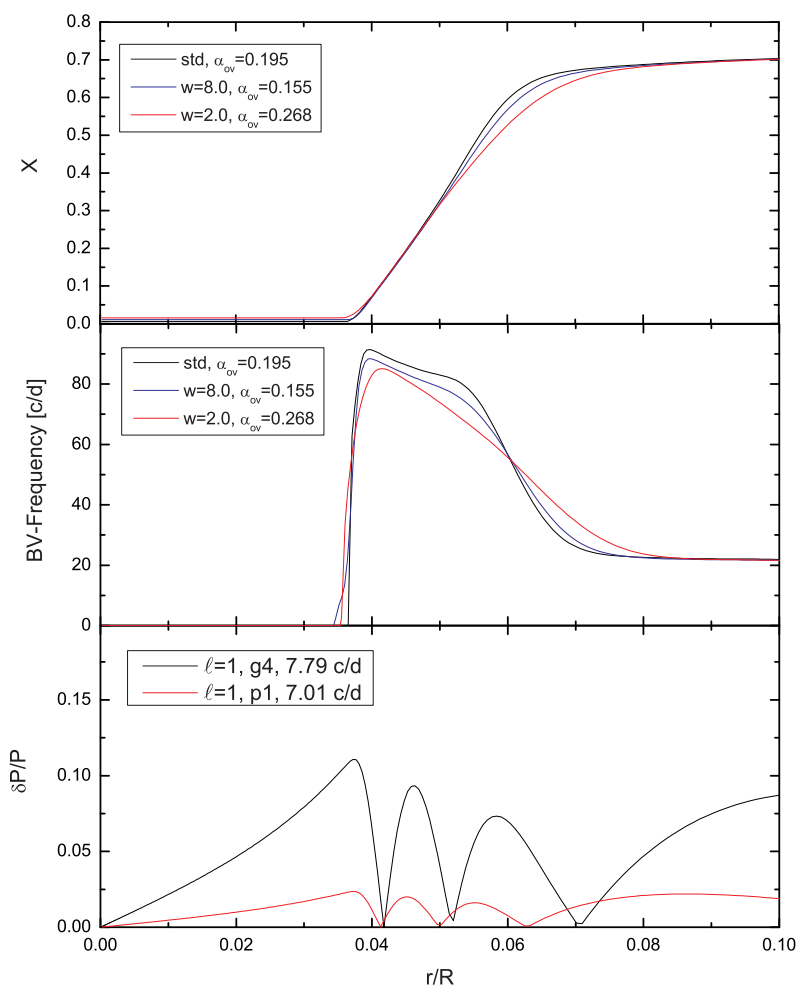


Figure 4.31: Comparison of the effects for different hydrogen mixing profiles. Upper panel: profile of the hydrogen mass fraction in the stellar core. Middle panel: Brunt-Väisälä frequency. Lower panel: relative Lagrangian pressure perturbation for two mixed $\ell=1$ modes, the mode at 7.01 cd^{-1} with strong acoustic character, and the mode at 7.79 cd^{-1} with strong gravity character.

4.8 Variability of photometric mode amplitudes

As mentioned earlier, 44 Tau was observed during several seasons from 2000 to 2006. Annual least-squares fits were made by Michel Breger to check the long term behavior of the amplitudes of the observed modes. Figure 4.32 presents the amplitudes of the annual solutions for the dominant modes with known spherical degree. The formal errors are very small and generally smaller than the size of the symbols. The radial modes exhibit essentially constant amplitudes. The $\ell = 1$ modes, however, feature strong amplitude variability, with a decrease of the amplitudes of f_2 , f_3 and f_4 during most of the observed period. The most significant changes are observed for f_6 . The $\ell = 2$ modes change their amplitudes on smaller scales.

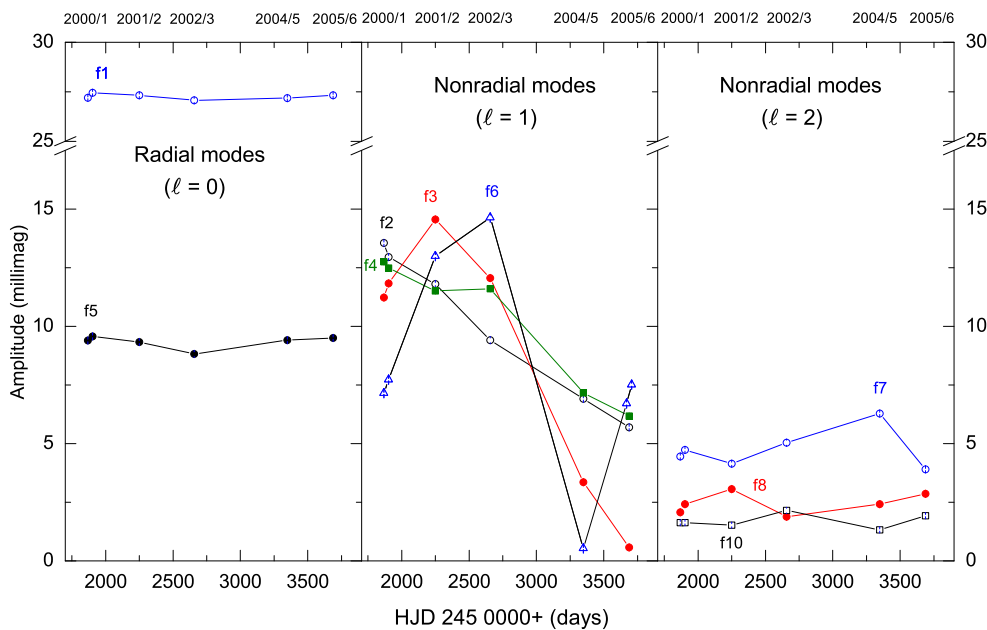


Figure 4.32: Observed amplitude variability of $\ell=0,1$ and 2 modes in the Strömgren y passband. The given error bars are very small and partly obscured by the symbols. This figure was created by Michel Breger for publication in Breger & Lenz (2008).

In the two seasons 2000/1 and 2005/6 the most extensive photometric data sets were obtained with a total of 259 h and 173 h, respectively. To test whether the variations within one season are consistent with the long-term trend these data sets were divided into two parts and analyzed. As can be seen in Figure 4.32 the amplitude variability on a short time scale are indeed in agreement with the general amplitude modulation. In other words, there are no indications of rapid amplitude variability within one season.

With the current data set we cannot decide whether the amplitude modulation is periodic

or not. However, since the observed variability appears to follow a rule and not to depend on a chaotic process, the question about the cause arises. Amplitude changes may be produced by various effects: (i) variable mode visibility due to geometrical causes, (ii) artifacts of unresolved modes in the frequency analysis, and (iii) changes of the intrinsic mode amplitudes due to resonance effects. These three hypotheses which will be examined in the next sections do not exclude other explanations. Therefore this list should not be seen as complete.

4.8.1 A geometrical explanation: precession of the pulsation axis

In a star that undergoes nonradial pulsation some parts of the surface move outwards while other parts move inwards. The amount of the light variation due to pulsation that arrives the observer depends on the inclination of the stellar pulsation axis and the surface geometry of the mode, i.e., the position of node lines on the surface. Since we only observe the integrated light over the stellar disc the light contribution from expanding and contracting parts of the surface is partly compensated. This effect is called geometrical light cancellation. For example the light variation of a zonal dipole mode is completely averaged out in an equator-on view (inclination angle $i=90^\circ$), while a sectoral mode (a running wave) causes clear light variations in the integrated light. Therefore, the stellar inclination, the spherical degree and the azimuthal order of a pulsation mode determine the visibility of a mode.

Figure 4.33 shows the photometric amplitudes in the Strömngren y band for axisymmetric and non-axisymmetric dipole and quadrupole modes computed for different inclination angles. The same intrinsic mode amplitude, $\delta r/R$, was assumed for all modes to examine only the geometrical aspect of the problem. The value of the intrinsic amplitude, ε , which was assumed to be the same for all modes, was determined by scaling the resulting photometric amplitudes to observed values. The Strömngren y amplitudes were computed following Daszyńska-Daszkiewicz et al. (2003)

$$A^y(i) = \varepsilon Y_\ell^m(i, 0) T_\ell^y \quad (4.1)$$

where T is derived from an atmosphere model for the given spherical degree of the mode.

Figure 4.33 clearly shows the effects discussed above. It also shows that light cancellation is more efficient for quadrupole modes. Their net light variations are smaller because more node lines are on the surface which results in more effective light cancellation. The photometric amplitudes of radial modes are not shown because they are the same for all inclinations.

The observed photometric mode amplitudes depend on the geometrical visibility and on the intrinsic mode amplitudes, $\delta r/R$. Let us assume that the observed amplitude variability in 44 Tau is solely due to a change of the geometrical mode visibility. The only quantity that may be considered variable is the stellar inclination angle. This leads to the hypothesis that the pulsation axis executes a precession.

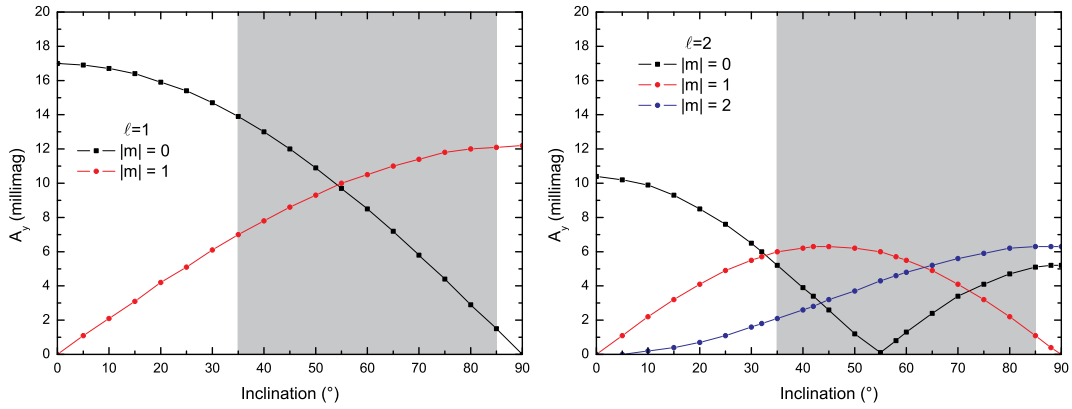


Figure 4.33: Photometric Strömgren y amplitudes of axisymmetric and nonaxisymmetric modes as a function of stellar inclination. The left diagram shows the case for dipole modes, the right diagram for quadrupole modes. The shaded area marks the range of uncertainty for the measured inclination of 44 Tau derived by Zima et al. (2007).

The symmetry axis for stellar pulsation is not chosen arbitrarily. Pulsation is commonly aligned to natural symmetry axes such as the rotational or magnetic axis. A well known example for stars in which the pulsation axis is aligned to the magnetic axis, while the rotation axis is inclined, are the roAp stars. It has been shown, e.g., by Kurtz (1982) that such a configuration explains the observed amplitude variability in this stars. These stars have strong magnetic fields which makes the magnetic axis the dominant symmetry axis. However, for 44 Tau Zima et al. (2007) did not find a strong magnetic field. As the rotation rate is very small one may assume that a dominant symmetry axis is not well defined in 44 Tau. On the other hand, for the Sun which has a similar equatorial rotation rate as 44 Tau the pulsation axis is in good agreement with the rotation axis.

Let us, nonetheless, assume that the pulsation axis undergoes precession due to an unknown reason. The inclination changes periodically with time. Since the cancellation effects of radial modes do not depend on inclination the visibility of radial modes remains the same, as observed.

Spectroscopic mode identification revealed that the dipole modes f_2 and f_3 are prograde modes ($m=1$) while f_4 is a zonal mode ($m=0$). The azimuthal order of the fourth $\ell = 1$ mode, f_6 could not be derived because it is not well resolved from the nearby mode f_9 in the spectroscopic data. The measured inclination angle of the pulsation axis in 2004 was $60 \pm 25^\circ$.

Let us assume that inclination axis changes between 30 - 90° due to precession as shown in the lower panel of Figure 4.34. The resulting photometric amplitudes for an axisymmetric and a nonaxisymmetric dipole mode is given in the upper panel of the diagram. The computed amplitude modulation for the axisymmetric mode mimics the observed change of f_6 . This may indicate that this mode is axisymmetric. The low amplitude of f_6 in 2004 would suggest an inclination of 85° which is at the upper limit given by Zima et al. (2007).

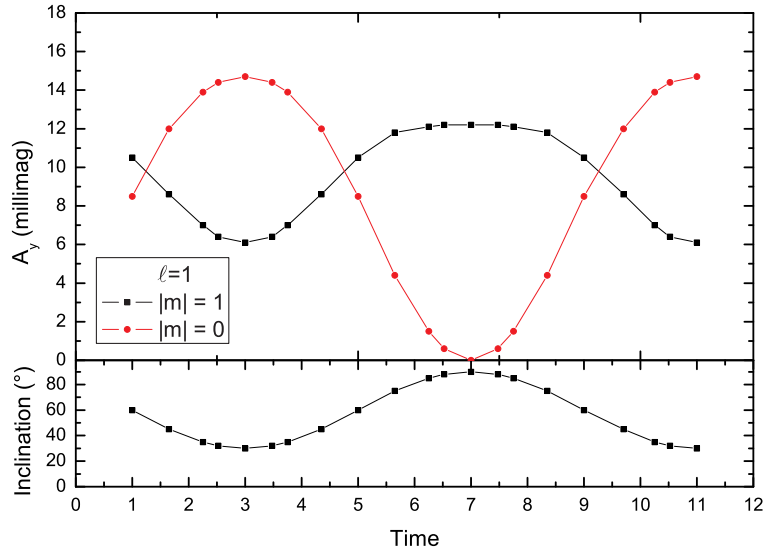


Figure 4.34: Influence of a precession of the pulsation symmetry axis on Strömgren y amplitudes. The inclination varies between 30° and 90° as given in the lower panel. The corresponding photometric amplitudes for a $(\ell, m)=(1, 0)$ mode and a $(\ell, m)=(1, 1)$ mode are given in the upper panel. The time is in arbitrary units.

However, the axisymmetric mode f_4 does not show a similar amplitude modulation and does not reach zero amplitude simultaneously with f_6 . Moreover, the prograde modes f_2 and f_3 clearly behave different, than what we would expect if the hypothesis of precession of the pulsation axis is true.

If we assume that the intrinsic mode amplitudes do not change strongly enough to compensate for the effects of a varying aspect view due to precession of the pulsation axis we have to conclude that this does not explain the observed amplitude variability in 44 Tau.

4.8.2 Beating between close frequencies

Beating between two modes with almost similar frequencies is a common phenomenon in δ Scuti stars because of their dense frequency spectrum. This effect was studied in detail for BI CMi by Breger & Bischof (2002) and FG Vir by Breger & Pamyatnykh (2006a). The authors show that close frequencies which are not resolved in a data set exhibit amplitude and phase modulation when prewhitened as a single mode. According to the rules of frequency beating (for frequencies with equal amplitudes) the resulting frequency is centered between f_1 and f_2 , $f_r = \frac{1}{2}(f_1 + f_2)$. The period of the amplitude modulation is $P_{\text{beat}} = 1/|f_1 - f_2|$.

Hence the beat period allows to draw a conclusion on the frequency spacing between the two pulsation modes generating this effect. Another important fact which can be used

as a proof for beating is the occurrence of a phase jump of 0.5 at the time of minimum amplitude (assuming the ideal case of equal amplitudes). However, if the amplitudes of the two beating modes are not equal, the effects described above are still present in a modified way.

In the case of 44 Tau special attention has to be given to the fact that the star rotates very slowly and rotationally split multiplets may not be resolved. Hence the observed amplitude variability of the dipole modes may be caused by three very close frequencies.

While the amplitude and phase modulation is well known for two-mode beating it may look different for three-mode beating. To examine the expected amplitude and phase variability for beating between the components of a rotational split multiplet artificial datasets were created and analyzed with the software Period04.

Depending on the actual inclination angle the components of a rotational splitting have different cancellation factors and hence different photometric amplitudes (assuming that the intrinsic mode amplitudes are equal). I examined impact for the two limits of the inclination, 35 and 85°. The rotationally split frequencies were computed for an equatorial rotation of 3 km s⁻¹ using a second order perturbation approach. At such low rotation rates the frequency splitting is almost equidistant (with a frequency separation of 0.011 cd⁻¹). Artificial data sets were created using:

- (i) the frequency values of the rotationally split components of the predicted dipole mode at the observed frequency of f_6 ,
- (ii) the photometric amplitudes for different inclinations were computed for each data set using the same approach as in the previous section, and finally
- (iii) arbitrary phases were chosen.

These artificial data sets were analyzed with Period04 assuming a single frequency hypothesis centered at the axisymmetric mode. The data set was divided into subsets and a least squares fit was performed allowing the amplitudes and phases to vary. The results are shown in Figure 4.35 for the two limits in the inclination.

At 35° the period of the amplitude modulation is $P_{\text{mod}} = 1/\Delta\nu_{0,\pm 1}$, where $\Delta\nu_{0,\pm 1}$ is the frequency separation between rotationally split components of a pulsation mode. The limit of 85° is very close to an equator-on view. At such inclinations the zonal mode at the center of the rotational splitting is almost canceled out as can be seen in Figure 4.33. The situation is nearly the same as in the case of beating between the frequencies of only two close modes with $P_{\text{mod}} = 1/\Delta\nu_{+1,-1}$. Therefore, frequency beating between components of a dipole triplet essentially occurs between the two sectoral modes of a dipole mode at such high inclinations.

An important proof of the presence of beating between two modes is the occurrence of a phase change at minimum amplitude. The only dipole mode for which a minimum is observed is f_6 . However, due to annual gaps in the data the exact time of the minimum is not known. No clear phase change can be seen (private communication with Michel Breger). The phase test is, therefore, only applicable for beating on shorter time scales than those seen in 44 Tau. So far amplitude variability due to beating was only confirmed

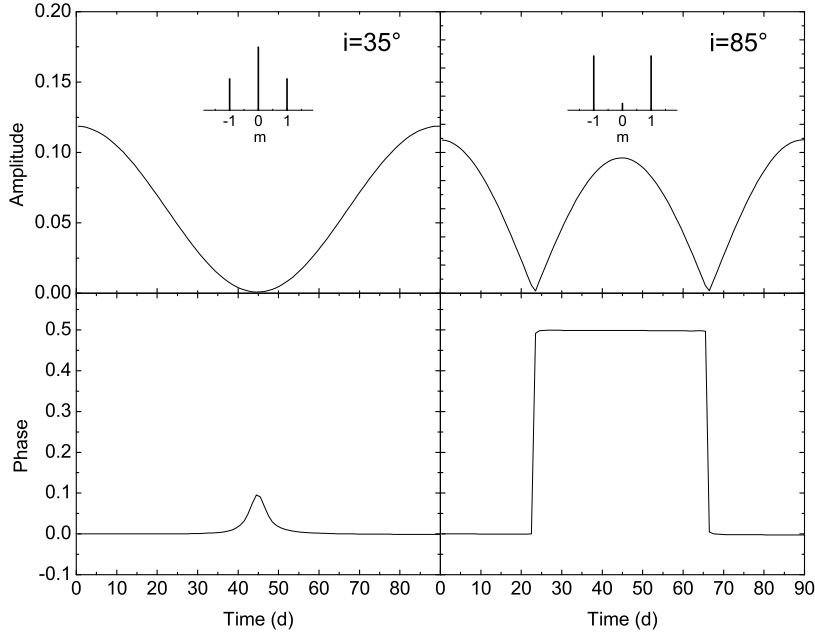


Figure 4.35: Beating between the frequencies of an unresolved rotational splitting of a dipole mode. The upper panels show the expected amplitude modulation for the lower and the upper limit of 44 Tau's inclination range. The lower panels present the corresponding phase change. The inset diagram shows the mode visibility at the given inclination.

for modes with amplitude modulations less than one year (see Breger & Bischof (2002) and Breger & Pamyatnykh (2006a)).

Nevertheless, we can study the time scales of amplitude modulation. For three-mode beating between the components of a dipole rotational splitting for different equatorial rotation rates the results are given in Table 4.11.

Frequency [cd^{-1}]	P_{mod} [d] for $V_{\text{rot}} = \dots$			
	1 km s^{-1}	3 km s^{-1}	5 km s^{-1}	
f_2	7.01	176	65	35
f_3	9.11	202	75	40
f_6	9.56	248	92	50
f_4	11.52	167	62	33

Table 4.11: Modulation period for three-mode beating.

For two-mode beating between the two non-axisymmetric modes in an $\ell = 1$ multiplet the values in the table can be divided by two. All modulation periods are smaller than one year. Consequently, beating between the components of a dipole triplet do not explain the observed changes in the photometric amplitudes.

Another explanation based on mode beating relies on the assumption that beating between the frequencies of close modes of different spherical degrees may occur. To generate amplitude modulation on the time scale of, say, 6 years the generating frequencies should be separated by only 0.0005 cd^{-1} . Close to the frequencies of the dipole modes f_2 and f_3 the pulsation model of 44 Tau predicts an $\ell = 3$ multiplet, and close to f_4 there is an $\ell = 4$ multiplet. However, it is unlikely that components of $\ell = 3$ and $\ell = 4$ reach amplitudes high enough to generate beating. It would require very high intrinsic amplitudes significantly larger than for the observed dipole modes.

Hence, beating between close frequencies does not explain the observed amplitude variability in 44 Tau.

4.8.3 Resonant coupling of pulsation modes

Up to now we considered the intrinsic amplitudes of the modes to be constant. In this section we will examine a modulation of the intrinsic amplitudes. A mechanism that could cause the temporal variation of the amplitudes of excited modes is resonant mode coupling. If two or more modes interact due to resonance, pulsation energy is transferred between the modes.

In the case of δ Scuti stars nonlinear effects are less important than for RR Lyrae stars as shown by Nowakowski & Dziembowski (2003). The occurrence of resonances in δ Scuti stars has been discussed mainly within the context of an amplitude limiting mechanism (e.g., Dziembowski & Krolikowska 1985; Dziembowski et al. 1988). However, some studies are explicitly devoted to the modulation effect of the amplitudes and phases. (Nowakowski 2005; Buchler et al. 1997; Moskalik 1985). In the context of this work we will restrict ourselves to use some of the results of these papers to qualitatively examine the impact of resonances on the mode amplitudes and phases in the case of 44 Tau. Currently, we still lack an ultimate confirmation of the presence of such nonlinear effects in δ Scuti stars.

The impact of nonlinear effects on the mode amplitudes are commonly studied within the framework of the so-called amplitude equations (Dziembowski 1982). This system of equations is difficult to study analytically and have to be solved numerically. Unfortunately, the time baseline of photometric data of 44 Tau is insufficient for a detailed examination of nonlinear effects by means of an integration of the amplitude equations.

Not long ago, resonant coupling between an unstable acoustic with stable g modes was studied for a model of the δ Scuti star XX Pyxidis by Nowakowski (2005). Due to resonance linearly stable modes of high ℓ are excited. From ground-based photometric data these modes cannot be detected, because the photometric amplitudes are very small due to large disc averaging factors. However, current satellite missions may provide the required

accuracy to find gravity modes of with high spherical degrees. Indeed, the first published results of a δ Scuti star observed with the CoRoT satellite mission, Poretti et al. (2009) detected a dense spectrum of nonradial modes. Fig. 3 in this paper shows many high order, high ℓ g modes below the identified fundamental mode at 6.92 cd^{-1} . Nowakowski (2005) also finds that the amplitude of the unstable acoustic modes shows irregular temporal behavior of its amplitude on a time scale which corresponds to the inverse linear amplitude growth rate of unstable mode. This is the typical time scale for many resonance effects.

	Frequency [cd^{-1}]	$\tau_{\text{res}} \approx 1/\gamma$ [yrs]
f_2	7.01	52.6
f_3	9.11	9.9
f_6	9.56	10.9
f_4	11.52	1.4

Table 4.12: Predicted time scales for resonance effects for a post-MS contraction model of 44 Tau. The inverse linear amplitude growth rates for the observed $\ell = 1$ modes are given.

For the dipole modes observed in 44 Tau which exhibit variable amplitudes the corresponding time scales are listed in Table 4.12. The predicted time scales are quite different while the observed time scales are similar for different modes. For f_2 the predicted resonance time scale is much longer than what we observe, whereas for f_4 τ_{res} is significantly shorter. Only for the two modes f_3 and f_6 which undergo an avoided crossing the time scale of 10 years is of the order of the observed amplitude modulation.

For a special type of resonance, the 1:1:1 resonance, the nonlinear interactions between the components of a rotationally split $\ell=1$ multiplet was examined by Buchler et al. (1995). Even at small rotation rates the frequency separation of the different azimuthal orders computed by linear theory is slightly asymmetric in frequency. It is assumed that the rotational triplet does not interact with other modes excited in the star. They found that the nonlinear frequencies are equally spaced due to resonance (meaning that the asymmetry of the rotational splitting is removed when the modes are coupled). This effect is called frequency locking and has been studied in great detail by Buchler et al. (1997). Consequently, in observed frequency spectra a rotational splitting may be found in exact resonance, while computed linear frequencies are only in near-resonance. This frequency mismatch (or off-resonance parameter), which characterizes the asymmetry of the linear frequencies is defined as

$$\delta\nu = \nu_{+1} + \nu_{-1} - 2\nu_0 \quad (4.2)$$

where the subscripts denote the corresponding m values. The higher the frequency mismatch, the less important is resonance. It is therefore obvious that in slowly rotating δ Scuti stars the 1:1:1 resonance might be an important effect. Moreover, Buchler et al. (1997)

found another condition that has to be fulfilled to generate resonant amplitude modulation:

$$\frac{\delta\nu}{\nu} \sim O\left(\frac{\Omega}{\nu}\right)^2 \lesssim O\left(\frac{\gamma}{\nu}\right) \quad (4.3)$$

where γ is the linear amplitude growth rate and Ω the rotation rate. γ/ν should be higher by an order of a magnitude. The authors also show that the period of the amplitude modulation corresponds to the inverse of $\delta\nu$.

To examine whether the observed amplitude variability of the dipole modes in 44 Tau can be explained by 1:1:1 resonance, we computed the rotationally split frequencies with a second order perturbation approach for equatorial rotation rates of 1, 3 and 5 km s⁻¹. The underlying model was the post-MS contraction model No. 3 in Table 4.9. Table 4.13 summarizes the results for the corresponding rotational splittings at different rotation rates. However it should be noted that we used the assumption of uniform rotation for the computation of the rotational splittings which may not be adequate. Differential rotation may modify the frequency spacing between the modes.

	Frequency [cd ⁻¹]	$\frac{\delta\nu}{\nu}$	$\frac{\gamma}{\nu}$	$\frac{\delta\nu}{\gamma}$	$\tau_{1:1:1}$ [yrs]	V_{rot}
f ₂	7.01	5.7 · 10 ⁻⁶	7.4 · 10 ⁻⁶	0.77	68	} 1 km s ⁻¹
f ₃	9.11	4.4 · 10 ⁻⁶	3.1 · 10 ⁻⁵	0.14	68	
f ₆	9.56	1.0 · 10 ⁻⁴	2.6 · 10 ⁻⁵	3.79	273	
f ₄	11.52	1.7 · 10 ⁻⁵	1.7 · 10 ⁻⁴	0.10	14	
f ₂	7.01	4.8 · 10 ⁻⁵	7.4 · 10 ⁻⁶	6.47	8.1	} 3 km s ⁻¹
f ₃	9.11	4.4 · 10 ⁻⁵	3.1 · 10 ⁻⁵	1.44	6.8	
f ₆	9.56	1.8 · 10 ⁻⁵	2.6 · 10 ⁻⁵	0.68	16.1	
f ₄	11.52	6.1 · 10 ⁻⁵	1.7 · 10 ⁻⁴	0.36	3.9	
f ₂	7.01	1.5 · 10 ⁻⁴	7.4 · 10 ⁻⁶	20.2	2.6	} 5 km s ⁻¹
f ₃	9.11	1.3 · 10 ⁻⁴	3.1 · 10 ⁻⁵	4.25	2.2	
f ₆	9.56	5.0 · 10 ⁻⁵	2.6 · 10 ⁻⁵	1.9	5.7	
f ₄	11.52	1.8 · 10 ⁻⁴	1.7 · 10 ⁻⁴	1.05	1.3	

Table 4.13: Amplitude modulation period for 1:1:1 resonance between the components of a rotational splitting of dipole modes, $\tau_{1:1:1} \approx |1/(\nu_{+1} + \nu_{-1} - 2\nu_0)|$.

At the lower limit of the rotation rates the predicted time scales for amplitude modulation due to 1:1:1 resonance are too long. Moreover, the factor $\delta\nu/\gamma$ should be larger than 1 (preferably of the order of 10) to suffice the condition given in Equation 4.3. This is not the case at this low rotation rate. At the upper limit of rotation the modulation time scales are shorter than observed for f₂, f₃ and f₄. For f₆ the predicted modulation period matches the observed variability. From these results we may conclude that within the limits of the measured rotation rate the time scales for the 1:1:1 resonance are of the order of

the observed changes in amplitudes. Remember that the underlying model relied on the assumption of rigid rotation. Nowadays, it is widely assumed that the internal rotation rate is a function of radius. For some β Cephei stars differential rotation could already be confirmed by observations of rotational splittings (Pamyatnykh et al. 2004).

It should be noted that for a rotation rate close to the upper limit of 5 km s^{-1} the components of triplet should have been detected since the frequency resolution of our data is smaller than the frequency separation between axisymmetric and nonaxisymmetric components of a triplet of $\sim 0.02 \text{ cd}^{-1}$ (provided that the amplitudes of these modes are large enough). These missing multiplets are an argument against 1:1:1 resonance because as the mode amplitude of one component goes down that of the other component should increase.

Again, the time baseline is too short to draw definitive conclusions. However, the examined time scales of the different effects point to resonance effects as the most plausible cause for the amplitude modulation observed in 44 Tau.

Chapter 5

Asteroseismic models for 4 CVn

The observed frequency range ($4.7\text{-}8.6\text{ cd}^{-1}$) and the low $\log g$ value of 3.34 ± 0.20 dex indicate a higher probability that 4 CVn is in the post-MS expansion phase. Nevertheless, the case of 44 Tau taught us that we should not neglect the possibility that 4 CVn is a less evolved object. Currently, we do not know its inclination angle and its $v \sin i$ value of approximately 120 km s^{-1} only poses a lower limit for the equatorial rotation rate. Imagine two stars in the same evolutionary stage and with the same mass. If star A rotates significantly faster than star B the observed $\log g$ value for star A will be smaller and it may, therefore, appear more evolved. This fact stresses the importance of considering models in earlier evolutionary stages even for this star.

A preliminary asteroseismic model of 4 CVn was presented by Zhou (1998). The author concluded that a post-MS model with a mass of $2.2 M_{\odot}$ matches the observed fundamental parameters well. Their pulsation model explains the seven dominant modes with spherical degrees between $\ell=1,2$ and 3. Unfortunately, their results are not supported by our mode identification.

5.1 Validity of the perturbation approach for rotation in the case of 4 CVn

Since the rotation rate of 4 CVn is high it is necessary to examine whether our perturbation approach to model rotational effects is still valid. As discussed in Section 2.3 the limit of the second order perturbation theory is expected when the equatorial rotation rate exceeds approximately 10% of the Keplerian break-up rate defined as

$$\Omega_K[\text{cd}^{-1}] \cong 54.233 \sqrt{\frac{M[M_{\odot}]}{R_e^3[R_{\odot}]}} \quad (5.1)$$

where R_e denotes the radius at stellar equator.

The mass and the radius of 4 CVn can be estimated from evolutionary models. A post-main sequence model in the expansion phase which fits the observed effective temperature and luminosity has a mass of $2.10 M_{\odot}$, and a radius of $4.30 R_{\odot}$. A main sequence model at the same position in the HR diagram has slightly different values with $2.17 M_{\odot}$ and $4.33 R_{\odot}$. Table 5.1 lists the results for the corresponding fraction Ω/Ω_K :

	α_{ov}	V_{rot} [km s ⁻¹]	Ω [cd ⁻¹]	Ω_K [cd ⁻¹]	Ω/Ω_K
post-MS	0.0	120	3.47	8.81	0.39
MS	0.4	120	3.44	8.87	0.39

Table 5.1: Ω/Ω_K for a MS and post-MS model in the center of the photometric box in the HR diagram.

As we can see for the given case the criterion $\Omega/\Omega_K \lesssim 0.10$ is not fulfilled. Moreover, attention has to be given to an additional requirement for the validity of the perturbation approach: $\Omega/\omega \ll 1$. For the frequencies detected in 4 CVn the fraction Ω/ω has a rather high value of ≈ 0.1 . Therefore, the second order perturbation approach does not allow us to accurately predict the individual frequency values of the observed modes and corresponding uncertainties in the results have to be taken into account. Considering the results by Lignières et al. (2006) these uncertainties may exceed 1 cd^{-1} . However, this does not prevent to derive some general conclusions from an asteroseismic investigation. Nevertheless, the uncertainties in our computations should be kept in mind for the next sections.

5.2 Inferences from the observed radial mode

In the case of 44 Tau the detected two radial modes put strong constraints on the pulsation models. In 4 CVn only one mode is identified as a radial mode with a high probability. Consequently, for 4 CVn the model parameters are less constrained. However, the radial mode at 6.98 cd^{-1} allows to approximately determine the mean density of the star. Since we only have one confirmed radial mode, we restricted the asteroseismic analysis to the use of OPAL opacities and GN93 mixture. Tests with different opacities and element mixtures only make sense if the theoretical models are well constrained by the observational data. This is (currently) not the case for 4 CVn. As we have seen in the previous section this standard recipe (OPAL GN93) successfully reproduced the observed modes of 44 Tau.

We computed sequences of evolutionary models adopting a mixing-length parameter of $\alpha_{MLT}=0.2$ and an initial equatorial rotation velocity of 150 km s^{-1} . The photometric indices indicate metal overabundance in the atmosphere of 4 CVn. To consider a possibly higher metallicity in the stellar interior two values for the metal mass fraction were adopted: 0.02 and 0.025. The hydrogen mass fraction was fixed with $X=0.70$. Moreover, the asteroseismic results were examined for different convective overshooting parameters ranging

from $\alpha_{ov}=0.0$ to 0.7. Due to the expected stronger rotationally induced mixing in 4 CVn the partially mixed region should be larger than in 44 Tau. Therefore, such high values of α_{ov} are justified. In the following sections pulsation models which fit the observed radial mode at 6.98 cd^{-1} are examined for different evolutionary stages. For the sake of brevity we will denote models which fit the first radial overtone to the frequency of 6.98 cd^{-1} as 1H models. The same scheme is used for the other radial overtones.

5.2.1 Post-main sequence models in the expansion phase

Figure 5.1 shows the position of post-main sequence models computed with $\alpha_{ov}=0.0$ in the HR diagram for two cases: a standard (solar) metallicity and metal overabundance.

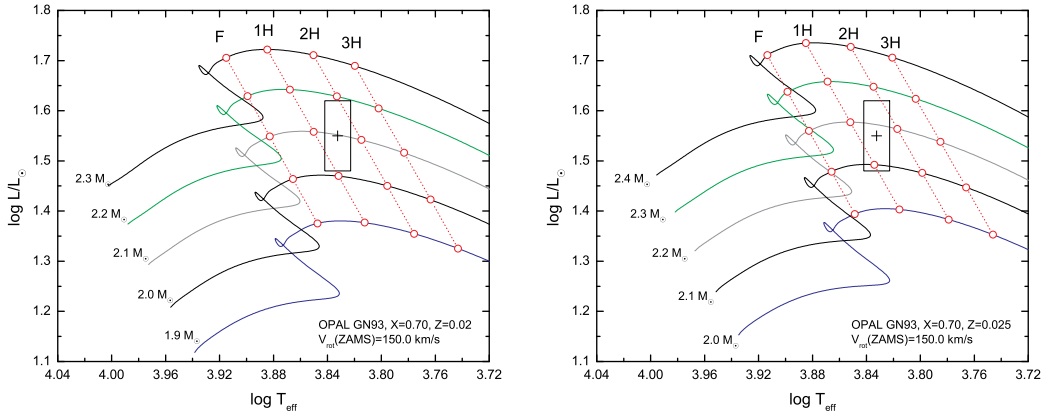


Figure 5.1: Evolutionary tracks of models with different mass in the HR diagram. The circles mark pulsation models in the post-MS expansion phase with a radial mode at 6.98 cd^{-1} . Asteroseismic models for the same radial overtone are connected with a line.

As we can see in the diagrams the models that fit the mode at 6.98 cd^{-1} as first or second radial overtone are inside or in the immediate vicinity of the photometric error box. The most likely value for the mass of 4 CVn ranges between $2.0 - 2.2 M_{\odot}$ for $Z=0.02$ and $2.1 - 2.3 M_{\odot}$ for $Z=0.025$. For these models the instability of the predicted modes was computed. The results are shown in Figure 5.2. Since the instability ranges for low-degree modes are nearly the same, the diagrams only present the results for quadrupole modes.

The computed instability ranges are quite different and allow to exclude some of the pulsation models. For example the pulsation models which fit the mode at 6.98 cd^{-1} as the radial fundamental mode can be discarded because the predicted instability range does not match the observed frequency range. The best agreement is found if the radial mode at 6.98 cd^{-1} is assumed to be the second overtone. However, some of the 1H and 3H models cannot be excluded. From the given results no conclusions about the metallicity can be made.

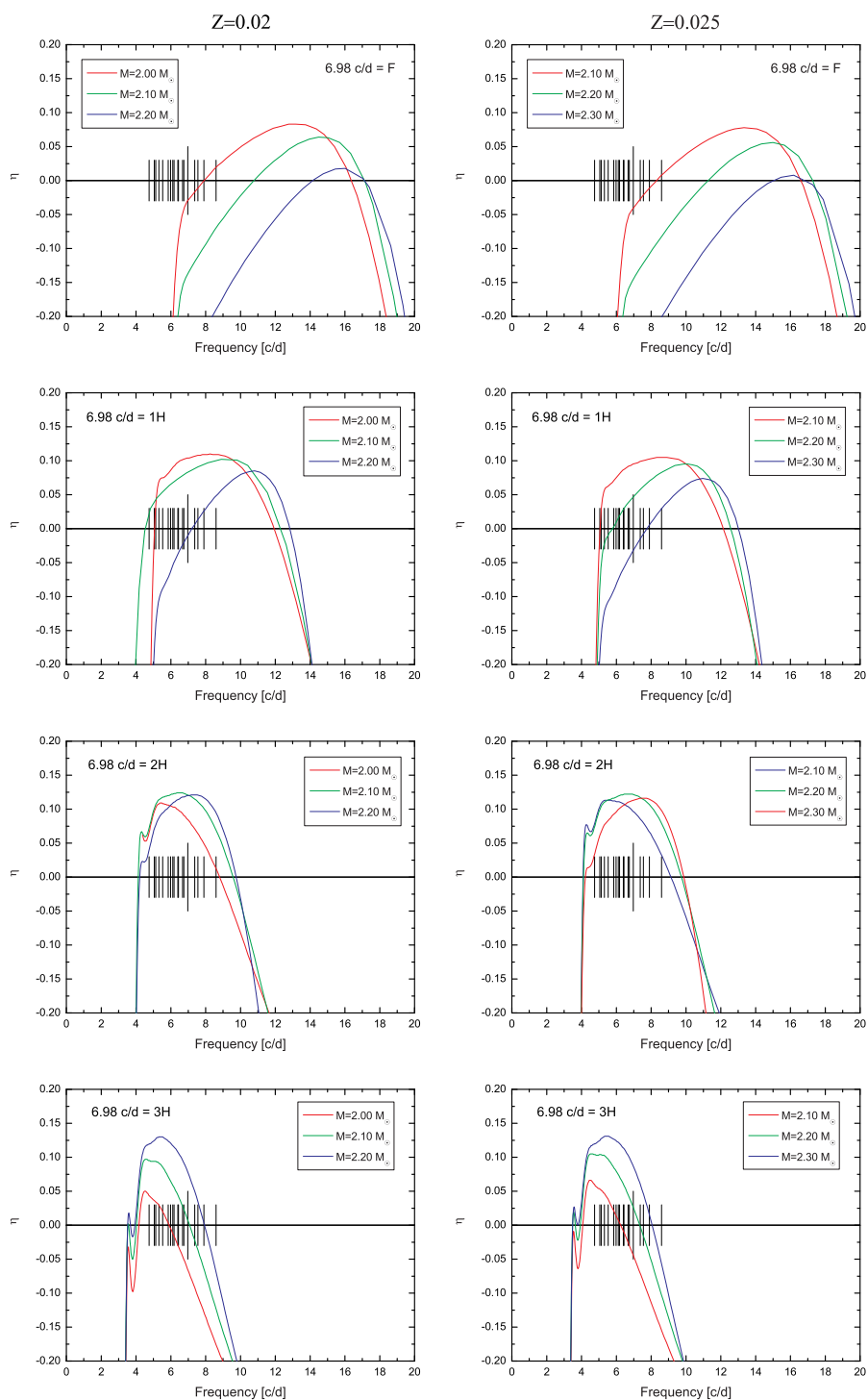


Figure 5.2: Instability parameter, η , for the predicted modes of selected post-MS models in the expansion phase. The vertical lines mark the observed modes. The longest vertical line delineates the position of the observed radial mode which is fit by all given models. The results for $Z=0.02$ are shown on the left side, those for $Z=0.025$ on the right side.

5.2.2 Post-main sequence models in the contraction phase

Pulsation models in the post-MS contraction phase provide a fit of the radial mode at 6.98 cd^{-1} only for specific overshooting parameters. To fit the radial first overtone to 6.98 cd^{-1} , an overshooting parameter of approximately 0.4 has to be chosen, whereas to fit the second radial overtone to this frequency a higher value of $\alpha_{\text{ov}}=0.7$ (for $Z=0.02$) or 0.6 (for $Z=0.025$) is required. The results for these models are shown in Figure 5.3. The corresponding instability ranges are given in Figure 5.4. For the first radial overtone scenario the observed frequencies are only predicted as unstable in models with a mass around $2.1 M_{\odot}$ and lower. For the case that the second radial overtone is at 6.98 cd^{-1} a good agreement is found for the given models. Note that the rotation rate slightly reduces with evolution, however, even for the 3H model the rotation rate is still within the expected uncertainty range of the derived $v \sin i$ value.

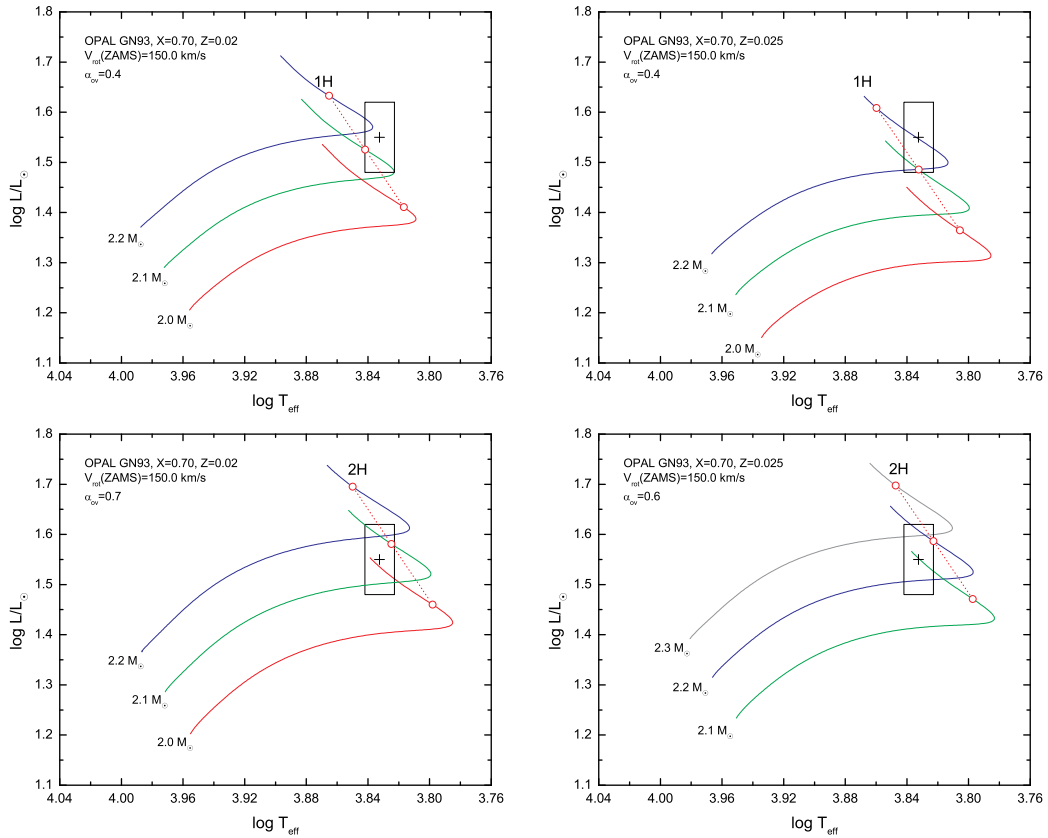


Figure 5.3: Evolutionary tracks of models with different mass in the HR diagram. The circles mark pulsation models in the post-MS contraction phase with a radial mode at 6.98 cd^{-1} . Like radial overtones are connected by a line.

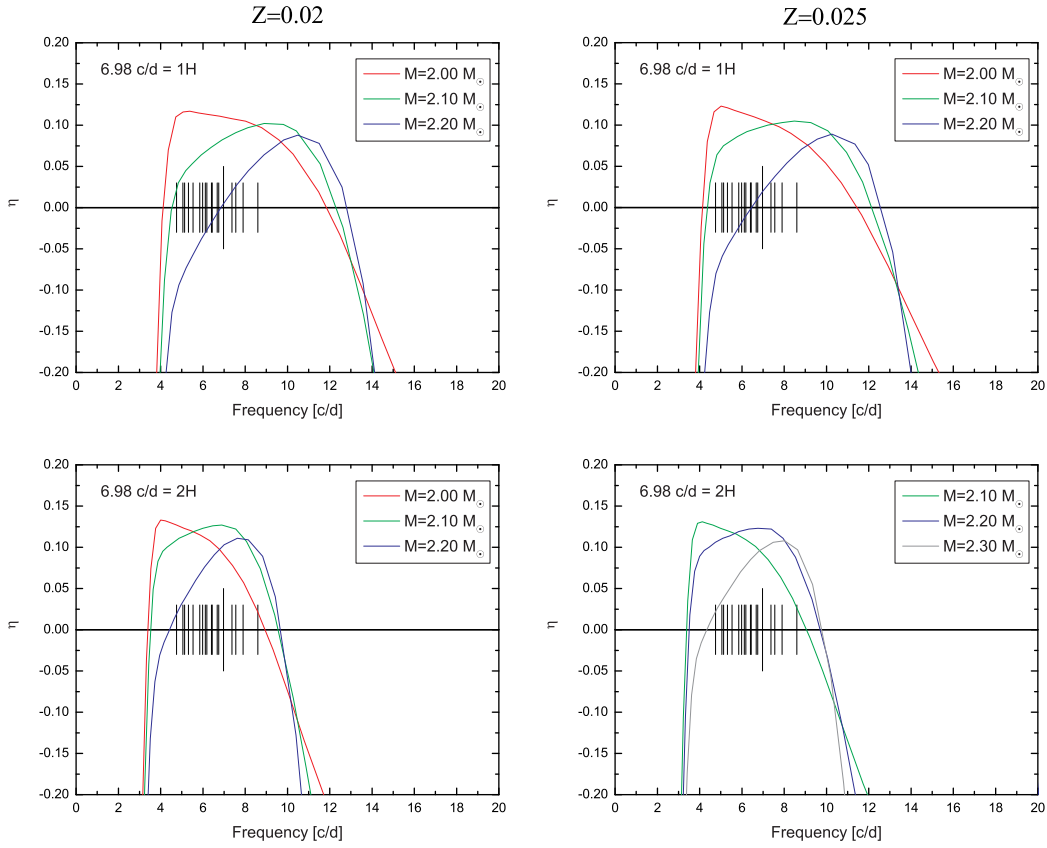


Figure 5.4: Instability parameter, η , for the predicted modes of selected post-MS contraction models. The vertical lines mark the observed modes. The longest vertical line delineates the position of the observed radial mode which is fit by all given models. The results for $Z=0.02$ are shown on the left side, those for $Z=0.025$ on the right side.

5.2.3 Main sequence models

The Figures 5.5 and 5.6 summarize the results for main sequence models. The best agreement is found for the assumption that the radial mode 6.98 cd^{-1} represents the first overtone for masses lower than $2.2 M_{\odot}$. If 6.98 cd^{-1} is assumed as the fundamental radial mode a large part of the observed frequency range is predicted unstable by a $2.0 M_{\odot}$ model. However, such a model also predicts excited modes at higher frequencies of up to 16 cd^{-1} which are currently not observed and does not reproduce the fundamental parameters well, as shown in Figure 5.5.

5.2.4 Theoretical frequency spectra

From the instability survey no clear preference for a specific model is given. Models explaining the frequency at 6.98 cd^{-1} as radial second overtone as well as first overtone are

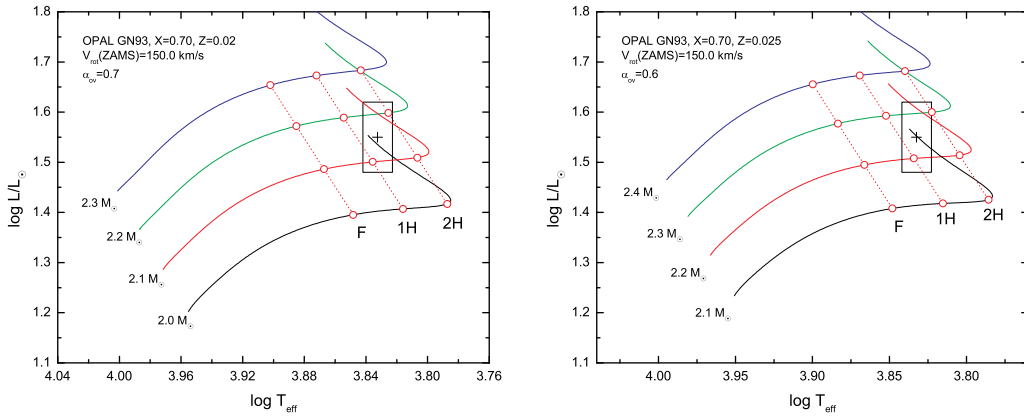


Figure 5.5: Evolutionary tracks of models with different mass in the HR diagram. The circles mark pulsation models in the main sequence phase with a radial mode at 6.98 cd^{-1} . Like radial overtones are connected by a line.

most probable. These models are also those closest to the photometric error box in the HR diagram. To examine whether the frequency spectra of models in different evolutionary stages can be used to make further constraints, the theoretical frequencies are compared to the observed frequencies for different models in Figure 5.7. For each case only the model closest to the derived luminosity and effective temperature of 4 CVn is shown.

Unfortunately, mode identification could not yet confirm the observation of a rotational splitting. The two $\ell=2$ mode at 5.53 cd^{-1} and 5.85 cd^{-1} may be candidates for a rotational splitting, however, the azimuthal order of the mode at 5.53 cd^{-1} is currently unknown. At an equatorial rotation velocity of 120 km s^{-1} the rotational splitting is very asymmetric. The asymmetry also depends on the Ledoux constant which is different for acoustic and gravity modes. Hence it will be necessary to observe at least three components of a rotational splitting to provide strong constraints on the rotational velocity of 4 CVn.

As can be seen the comparison between the structures of theoretical and observed frequency spectra does not provide a clear preference for a specific evolutionary stage. However, some general conclusions can be made: 6.98 cd^{-1} could be the only radial mode that is observed. The first radial overtone in 2H models is predicted at 5.60 cd^{-1} . This frequency is close to the mode at 5.58 cd^{-1} which though was already identified as a quadrupole mode. The fundamental radial mode would be expected at approximately 4.33 cd^{-1} and the third overtone at $\approx 8.34 \text{ cd}^{-1}$. For 1H models we generally expect the fundamental radial mode at approximately 5.42 cd^{-1} , and the second radial overtone around 8.68 cd^{-1} . Currently, no candidate peaks are found around these frequencies. The detection of a frequency at these values could be used to finally determine the radial order of the radial mode at 6.98 cd^{-1} . However, with our current instruments it will be unlikely to obtain reliable mode identification for a frequency with a presumably quite low amplitude.

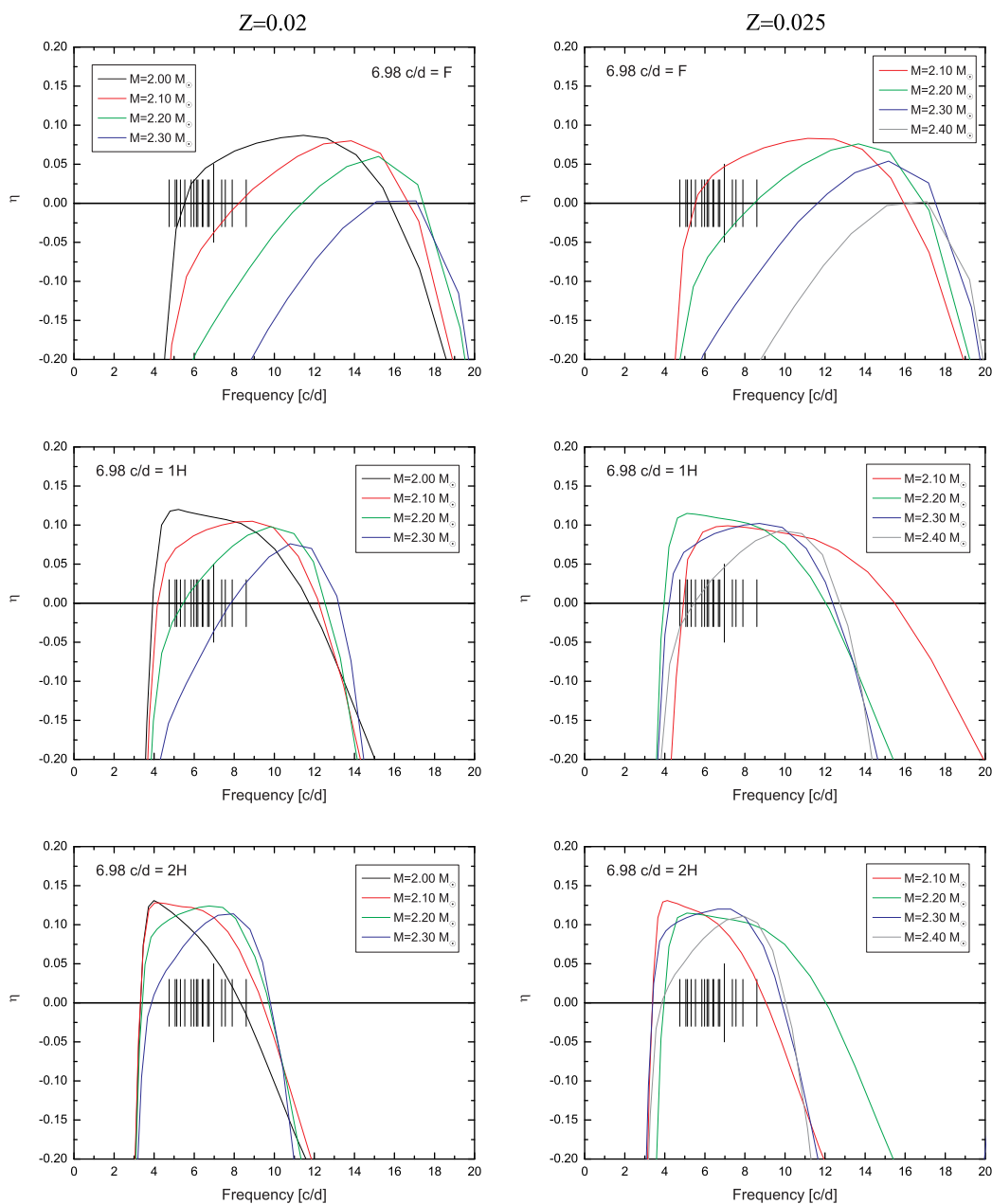


Figure 5.6: Instability parameter, η , for the predicted modes of selected main sequence models. The vertical lines mark the observed modes. The longest vertical line delineates the position of the observed radial mode which is fit by all given models. The results for $Z=0.02$ are shown on the left side, those for $Z=0.025$ on the right side.

Another difference between the 1H and 2H models is the corresponding $\log g$ value which is around 3.5 for 1H models, 3.38 for 2H models and 3.3 for 3H models. These predicted

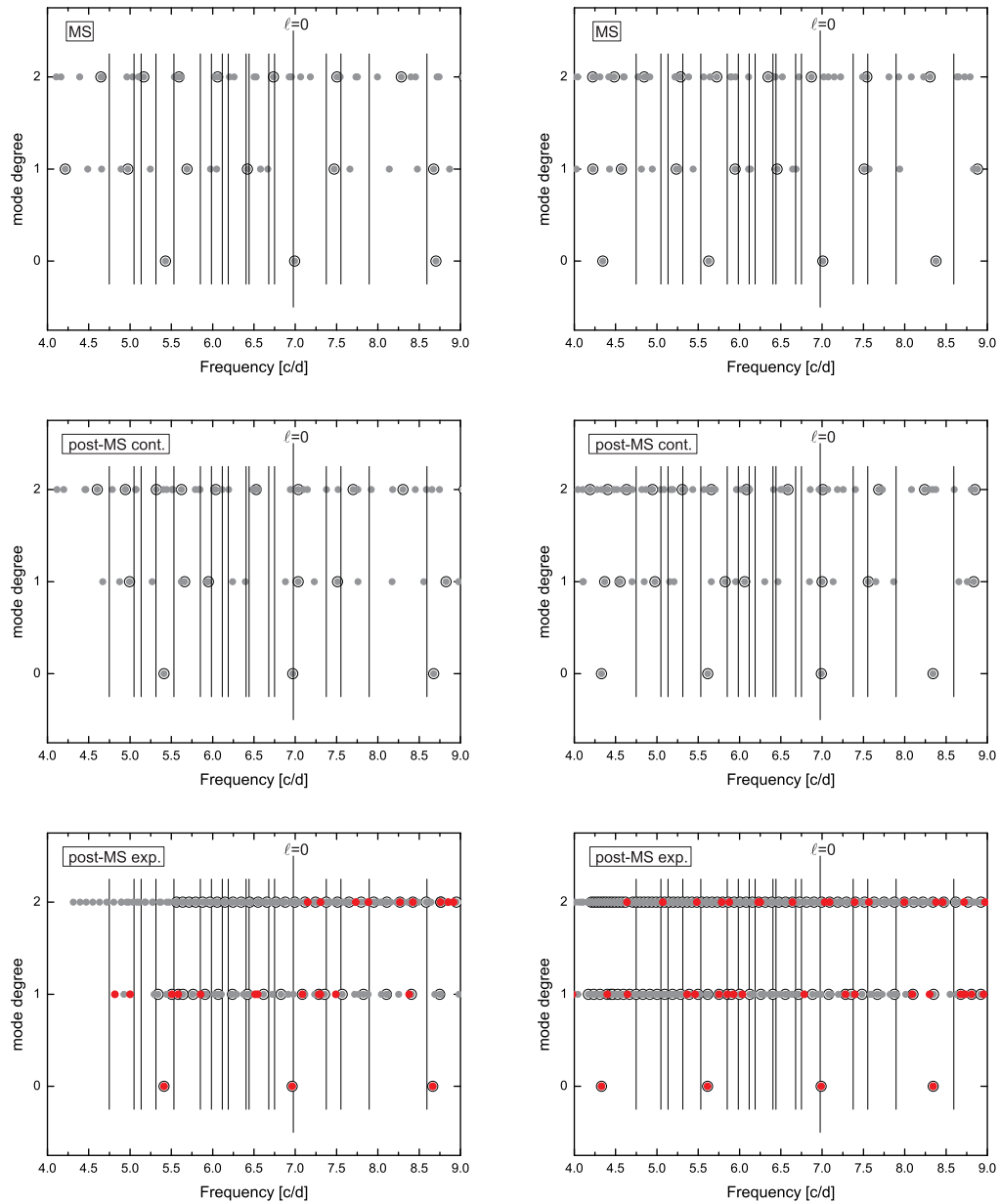


Figure 5.7: Theoretical frequency spectra of 1H (right) and 2H models (left) in all possible evolutionary stages. Observed frequencies are indicated as vertical lines. The theoretical modes are shown as filled grey circles. Axisymmetric modes are additionally marked with a concentric circle. For post-MS expansion models trapped modes are shown with red points.

$\log g$ values do not significantly change between MS and post-MS models. All these values are within the uncertainty range of the value derived from observations: 3.34 ± 0.20 . However, the results depend on the assumed rotational velocity. A higher rotation rate leads to a lower surface gravity. Therefore, a future determination of the $\log g$ value from spectroscopy would also provide valuable information as a consistency check and allow to decrease the error bars.

Contrary to 44 Tau, our asteroseismic analysis of 4 CVn was less successful in determining the optimum stellar model. The identification of the spherical degrees and azimuthal orders of additional modes will allow us to put stronger constraints on the asteroseismic models of 4 CVn. Moreover, a two-dimensional theoretical model and a proper implementation of rotational effects is required to obtain more accurate theoretical frequencies.

Chapter 6

Determination of intrinsic mode amplitudes

For evolved δ Scuti stars theory predicts many more unstable modes than observed with ground-based data. However, recent space missions such as CoRoT revealed that the pulsation spectra of δ Scuti stars consist of up to 1000 frequencies of which the majority has very low amplitudes (Poretti et al. 2009; García Hernández et al. 2009). These low-amplitude modes could only be found due to the excellent photometric accuracy of space telescopes.

These results imply that the predicted modes exist but only some of them are excited to large amplitudes. Consequently, a mode selection mechanism exists. Observational data can provide hints to identify this mechanism. For example low-degree modes which exhibit amplitudes that are high enough to be seen in ground-based data, tend to cluster around radial modes (Breger et al. 2009). This can be explained by trapping of specific modes in the acoustic cavity. Dziembowski & Krolikowska (1990) argue that trapped modes may have a higher probability to grow to large amplitudes due to their low kinetic energy.

In the framework of linear pulsation theory the amplitudes of pulsation modes cannot be predicted, because the mode amplitudes are not linearly related to the growth rates. The amplitude of a mode grows exponentially until nonlinear effects limit the growth and lead to a constant or modulated amplitude. Consequently, a nonlinear pulsation theory is required to determine the mode amplitudes. A detailed discussion of these effects is out of the scope of this work, therefore, we only briefly mention the two nonlinear main processes that may limit the mode amplitudes:

- Resonant coupling between pulsation modes.
Resonance occurs, e.g., when the frequency of one mode is n times the frequency of another mode, where n is an integer number. Due to mode coupling an exchange of pulsation energy takes place which modifies the amplitudes.

- Saturation of the driving mechanism.
Christy (1966) showed that the κ mechanism can be saturated, which means that the efficiency of the conversion of the radiative energy flux into work is limited.

The importance of these effects for a δ Scuti star was examined by Nowakowski (2005). The author compared the computed amplitudes for the star XX Pyx with observations and concluded that resonant mode coupling is not the dominant effect in a slightly evolved main sequence δ Scuti star like XX Pyx and that the collective saturation of the pulsation instability is important.

For these comparisons observationally derived intrinsic mode amplitudes are crucial. Hitherto, a reliable determination of mode amplitudes was hampered by the lack of reliable mode identifications. With the successful identification of the spherical degree and azimuthal order of many modes in 44 Tau and FG Vir, and the well constrained stellar inclination angle it is now possible to estimate the intrinsic mode amplitudes for these stars.

6.1 The method

The DD-method discussed in Chapter 3 not only evaluates the spherical degree of a mode based on the amplitudes and phases derived from multicolor photometry and radial velocity data, but also determines the quantity $\tilde{\varepsilon}$ from the semi-analytical equations 3.4 and 3.9. $\tilde{\varepsilon}$ is defined as

$$\tilde{\varepsilon} \equiv \varepsilon Y_{\ell}^m(i, 0) \quad (6.1)$$

where ε is a complex parameter fixing the amplitude and phase of the pulsation mode. The first parameter of the spherical harmonic, Y_{ℓ}^m , denotes the inclination and the second parameter is the azimuth angle. As the azimuth angle is unimportant due to symmetry, it is set to 0.

Consequently, if the spherical degree, the azimuthal order and the stellar inclination are known, the complex quantity ε can be derived. $|\varepsilon|$ then corresponds to $\langle \delta r / R \rangle_{\text{rms}}$ over the stellar surface. In the next sections the derived intrinsic amplitudes for 44 Tau and FG Vir are presented.

6.2 Intrinsic mode amplitudes of 44 Tau

The examined modes of 44 Tau are listed in Table 6.1 with their identified spherical degrees and azimuthal orders. The m -values were determined by means of the FPF-method by Zima et al. (2007). For f_{10} and f_{12} the azimuthal order is unknown. Therefore, all possible m values ($|m| \leq \ell$) were considered for these two pulsation modes. The ℓ values given in the table refer to the results of the DD-method presented in Chapter 3. For the two modes

		DD-method	Asteroseismic model	Zima et al. (2007)
Frequency [cd^{-1}]		ℓ	ℓ	m
f_{10}	6.3390	2	2	-
f_8	6.7955	2	2	0
f_1	6.8980	0	0	0
f_2	7.0060	1	1	1
f_7	7.3031	2	2	0
f_{11}	8.6391	2,1	2	0
f_5	8.9606	0	0	0
f_3	9.1174	1	1	1
f_{12}	11.2947	2,1,0	2	-
f_4	11.5196	1	1	0

Table 6.1: Set of modes of 44 Tau used for the analysis. Mode identification for the frequencies of 44 Tau with ℓ values according to the results of the DD-method and the post-MS contraction model presented in this work. m values from Zima et al. (2007).

f_{11} and f_{12} the DD-method did not yield an unambiguous solution. However, in both cases the lowest χ^2 values were found for $\ell=2$ which is supported by the post-main sequence contraction model presented in Chapter 4. Since this model was obtained solely relying on the uniquely identified modes and shows an excellent fit of these modes, the model can be used to point to the correct identification. The spherical mode degrees according to the model are shown in the last-but-one column in the table. The close pair f_6 (9.56 cd^{-1}) and f_9 (9.58 cd^{-1}) is not considered in this analysis since the resolution of the radial velocity data does not allow for a reliable determination of their amplitudes and phases.

To compute the intrinsic mode amplitudes the stellar inclination has to be known. Zima et al. (2007) measured the inclination of 44 Tau to be $60 \pm 25^\circ$. Moreover, an adequate atmosphere model is required. The fundamental parameters of Model 3 in Table 4.9 were adopted. The measured microturbulence velocity of $1\text{-}2 \text{ km s}^{-1}$ and normal (solar) metallicity were assumed.

The calculated estimates for the intrinsic mode amplitudes are shown in Figure 6.1 for several inclination angles within the possible range between 35 and 85° . The effect of the choice of the microturbulence velocity on the determination of intrinsic mode amplitudes was tested and found to be very small. The results are presented for $v_{\text{mic}} = 2 \text{ km s}^{-1}$. The intrinsic mode amplitudes, $|\varepsilon|$, for the measured mean inclination of 60° are listed in Table 6.2.

The Strömgren y amplitudes refer to the observed photometric values in 2004. The radial velocity amplitudes were taken from Zima et al. (2007). The corresponding formal uncertainties of the intrinsic mode amplitudes, $\sigma_{|\varepsilon|}$, are given in the last column. Since these uncertainties do not incorporate the uncertainties in the inclination angle they only represent lower limits. The discussion of these results follows after the next section which

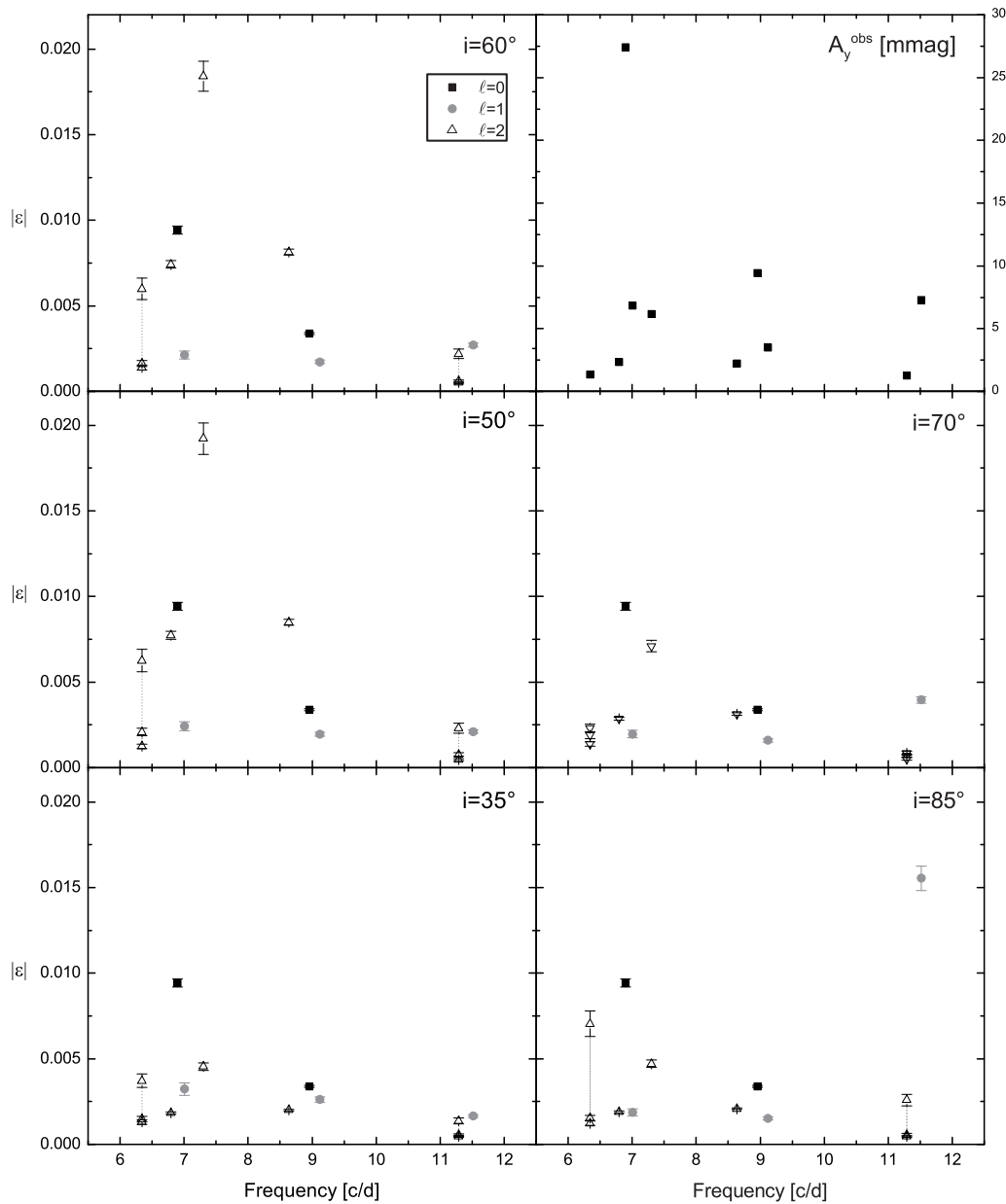


Figure 6.1: Intrinsic mode amplitudes of 44 Tau for the mean inclination $i=60^\circ$ and other possible angles within the uncertainty range. If there are several possible mode identifications for one frequency, the corresponding intrinsic amplitudes are connected with dotted gray lines.

	Frequency [cd^{-1}]	A_y [mmag]	A_{RV} [km s^{-1}]	ℓ	$ m $	$ \varepsilon $	$\sigma_{ \varepsilon }$
f_{10}	6.3390	1.36	0.21	2	0	0.0060	0.0007
				2	1	0.0014	0.0002
				2	2	0.0016	0.0002
f_8	6.7955	2.34	0.28	2	0	0.0074	0.0003
f_1	6.8980	27.42	2.22	0	0	0.0094	0.0003
f_2	7.0060	6.86	0.46	1	1	0.0021	0.0003
f_7	7.3031	6.19	0.70	2	0	0.0184	0.0009
f_5	8.9606	9.44	1.03	0	0	0.0034	0.0001
f_3	9.1174	3.51	0.44	1	1	0.0017	0.0002
f_4	11.5196	7.27	0.73	1	0	0.0027	0.0002
f_{11}	8.6391	2.21	0.32	2	0	0.0081	0.0002
f_{12}	11.2947	1.26	0.11	2	0	0.0022	0.0003
				2	1	0.0005	0.0001
				2	2	0.0006	0.0001

Table 6.2: Intrinsic mode amplitudes of 44 Tau for an inclination angle of 60° .

presents results for FG Vir.

6.3 Intrinsic mode amplitudes of FG Vir

FG Vir is a δ Scuti star in the main-sequence evolutionary stage. The latest frequency solution with 79 frequencies was published by Breger et al. (2005). Many authors contributed to the important task of mode identification (e.g., Viskum et al. 1998; Mantegazza & Poretti 2002, ...). The most recent mode identifications were obtained by Daszyńska-Daszkiewicz et al. (2005b) and Zima et al. (2006). These authors obtained their results based on a data set consisting of many more nights of data than previous mode identification studies. Their results are listed in Table 6.3.

Some spherical degree identifications of the FPF-method could be excluded by the DD-method and vice versa. The last column lists the subset of ℓ values which are in agreement in Daszyńska-Daszkiewicz et al. (2005b) and Zima et al. (2006). Only this set of ℓ values was used in this study. The results for modes without a unique identification should be taken with caution.

The data set used in this study was gathered in 2002 and was also used in the two papers mentioned above. For FG Vir, Daszyńska-Daszkiewicz et al. (2005b) determined the best value for the microturbulence velocity, v_{mic} , to be 4 km s^{-1} . This value is supported by the results from spectral line synthesis by Mittermayer & Weiss (2003) who found a value of $3.9 \pm 0.2 \text{ km s}^{-1}$. These authors also determined the photospheric element abundances and found a near-solar abundance pattern. The equatorial rotational velocity, $v \sin i$, is

Frequency [cd^{-1}]	JDD (2005)	Zima et al. (2006)		used in this work	
	ℓ	ℓ	m	ℓ	
f_6	9.199	2	1,2,3	1	2
f_8	9.656	2	0,1,2	0	2
f_3	12.154	0	0,1,2	0,1	0
f_1	12.716	1	0,1	0	1
f_{13}	12.794	2,1	2,3,4	-2	2
f_9	19.227	2,1,0	1,2	1	1,2
f_7	19.867	2,1	0,1,2	0	1,2
f_{10}	20.287	0,1	1,2,3	-1	1
f_4	21.051	1,0	0,1,2	0	0,1
f_5	23.403	2,1	2	0	2
f_2	24.227	1	0,1	0	1

Table 6.3: Mode identification for FG Vir frequencies according to Daszyńska-Daszkiewicz et al. (2005b) and Zima et al. (2006).

$21.6 \pm 0.3 \text{ km s}^{-1}$ and the inclination angle was determined to be $19 \pm 5^\circ$ by Zima et al. (2006). For the computation of the intrinsic mode amplitudes the same model parameters as given in Breger & Pamyatnykh (2006b), i.e., $M=1.80 M_\odot$, $\log T_{\text{eff}}=3.8658$, $\log L/L_\odot = 1.120$, $\log g = 3.980$ and $V_{\text{rot}} = 62.5 \text{ km s}^{-1}$ were used.

Figure 6.2 shows the results for $|\varepsilon|$ for the inclination angles 14° , 19° and 24° with corresponding error bars. If the identification of ℓ and/or m is ambiguous, the amplitudes for all possible (ℓ, m) values are plotted for this frequency. In Table 6.4 the intrinsic mode amplitudes for the mean inclination of 19° are listed. The Strömgren y amplitudes in the table and in Figure 6.2 refer to the values in 2002 using the frequency fit from Breger et al. (2005). The radial velocity amplitudes were taken from Zima et al. (2006).

6.4 Discussion

The intrinsic mode amplitudes are of the order of 0.1 % of the stellar radius for most of the modes in FG Vir, but significantly higher for the modes f_1 , f_6 and f_{13} . In the case of 44 Tau the inclination angle is not as well constrained as for FG Vir which results in larger uncertainties in the mode amplitudes. However, it can be concluded that the intrinsic mode amplitudes in 44 Tau are slightly higher, with values around 0.2 % of the stellar radius. A few modes also have significantly larger values of $|\varepsilon|$. In both stars there is no clear evidence that higher intrinsic mode amplitudes are limited to a specific region of the frequency spectrum. However, the modes with higher frequencies tend to have low intrinsic amplitudes.

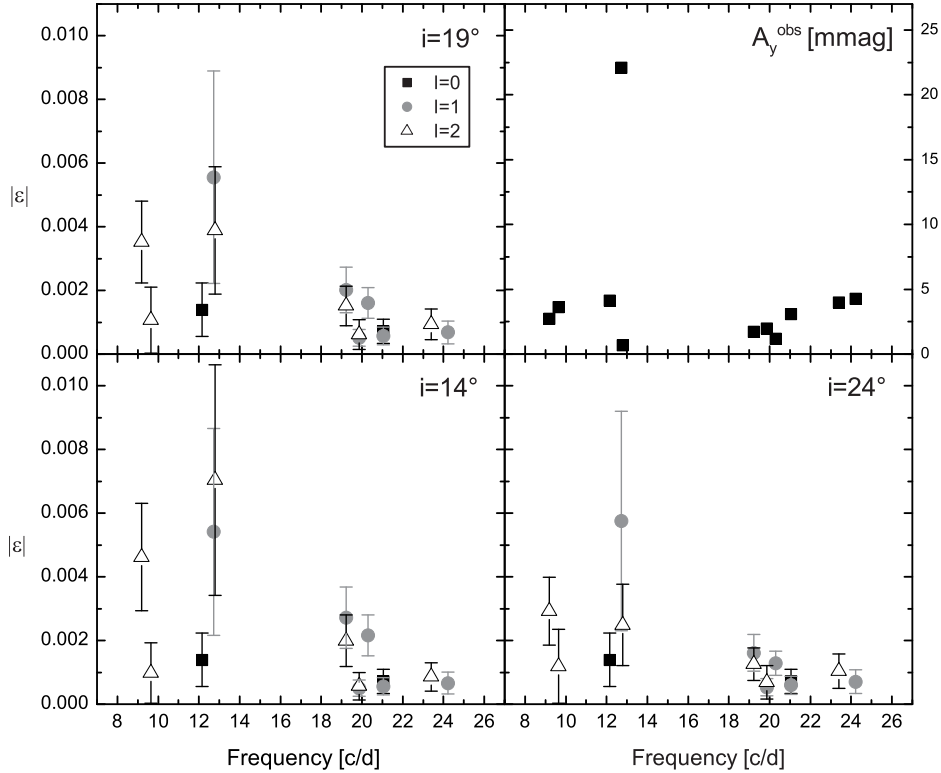


Figure 6.2: Intrinsic mode amplitudes, $|\epsilon|$, of FG Vir evaluated for the mean inclination angle of 19° and its uncertainty limits. If the identification of ℓ and/or m is ambiguous, the amplitudes for all possible (ℓ, m) values are plotted for this frequency and connected by a line. Upper right panel: observed Strömgren y amplitudes in the observing season 2002.

The correlation between photometric and intrinsic mode amplitudes for the two δ Scuti stars is examined in Figure 6.3. Similar plots comparing $|\epsilon|$ with the radial velocity amplitudes show essentially the same results.

Figure 6.3 shows that there is no clear correlation between the photometric y amplitudes and the intrinsic mode amplitudes, $|\epsilon|$, from the analyzed sample of frequency peaks in FG Vir. However, in a similar plot for 44 Tau (Figure 6.3) two slopes can be clearly seen. The modes identified as $(\ell, m) = (2, 0)$ show a different correlation between photometric and intrinsic amplitudes than the $\ell=0$ and $\ell=1$ modes. Generally, one can expect a correlation between photometric and intrinsic amplitudes as far as modes with like (ℓ, m) are concerned, because of the same geometrical cancellation factor. Modes with a different spherical degree and azimuthal order are expected to form different slopes. The steep slope of the quadrupole modes illustrates that a much higher intrinsic amplitude is needed to produce the same photometric amplitude as a dipole mode. For FG Vir we do not see a similar distinct structure in the diagram because not enough modes of the same species (i.e., with

	Frequency [cd^{-1}]	A_y [mmag]	A_{RV} [km s^{-1}]	ℓ	m	$ \varepsilon $	$\sigma_{ \varepsilon }$
f_6	9.1991	2.74	0.34	2	1	0.0035	0.0013
f_8	9.6563	3.62	0.26	2	0	0.0011	0.0011
f_3	12.1541	4.11	0.41	0	0	0.0014	0.0009
f_1	12.7163	22.10	2.23	1	0	0.0056	0.0034
f_{13}	12.7942	0.69	0.08	2	-2	0.0039	0.0020
f_9	19.2279	1.73	0.22	1	1	0.0020	0.0008
				2	1	0.0015	0.0007
f_7	19.8676	1.97	0.30	1	0	0.0005	0.0003
				2	0	0.0006	0.0005
f_{10}	20.2878	1.18	0.25	1	-1	0.0016	0.0005
f_4	21.0515	3.07	0.41	0	0	0.0007	0.0004
				1	0	0.0006	0.0003
f_5	23.4033	3.99	0.37	2	0	0.0009	0.0005
f_2	24.2280	4.27	0.48	1	0	0.0007	0.0004

Table 6.4: Intrinsic mode amplitudes, $|\varepsilon|$, for a FG Vir model with a mean inclination of 19° . The corresponding uncertainties, $\sigma_{|\varepsilon|}$, are given in the last column. The Strömrgren y amplitudes refer to the values in 2002 using the frequency fit from Breger et al. (2005). The radial velocity amplitudes were taken from Zima et al. (2006).

like ℓ and m values) were observed. For 44 Tau, with exception of two $\ell=1$ modes, all identified modes are axisymmetric, which causes a clearer structure in the diagram.

The aspect factor determined by the spherical harmonic can be removed from the photometric amplitudes. The results are shown in Figure 6.4. As expected, the slopes for $\ell=2$ and $\ell=1,0$ are closer but a difference remains. This is mainly due to the fact that the ratio A_y/Y_ℓ^m does not consider all geometrical effects as can be seen in equation 4.1.

It is an unexpected result that in both stars some $\ell=2$ modes have a very high intrinsic mode amplitude. In the case of 44 Tau the $(\ell, m)=(2, 0)$ mode f_7 has even a larger value of $|\varepsilon|$ than the fundamental radial mode. A similar result was found for the β Cephei star θ Oph by Daszyńska-Daszkiewicz & Walczak (2009) where a quadrupole mode was found to have a significantly higher intrinsic amplitude than a radial mode. The reason for the excitation of $\ell=2$ modes to such large values of $|\varepsilon|$ is currently not known.

The excellent theoretical fit of the observed modes in 44 Tau allows to examine the relation between intrinsic mode amplitudes and linear growth-rates or the fraction of kinetic energy confined in the gravity cavity, E_g/E_k , respectively. Table 6.5 lists the corresponding values predicted by Model 3 in Table 4.9. Figure 6.5 shows the results. No clear correlation is found between the intrinsic mode amplitudes and the linear growth-rates. This may indicate that nonlinear effects are important.

For δ Scuti stars the main uncertainties in this approach, originate from uncertainties in the modeling of the outer stellar layers, in particular the treatment of convection. This

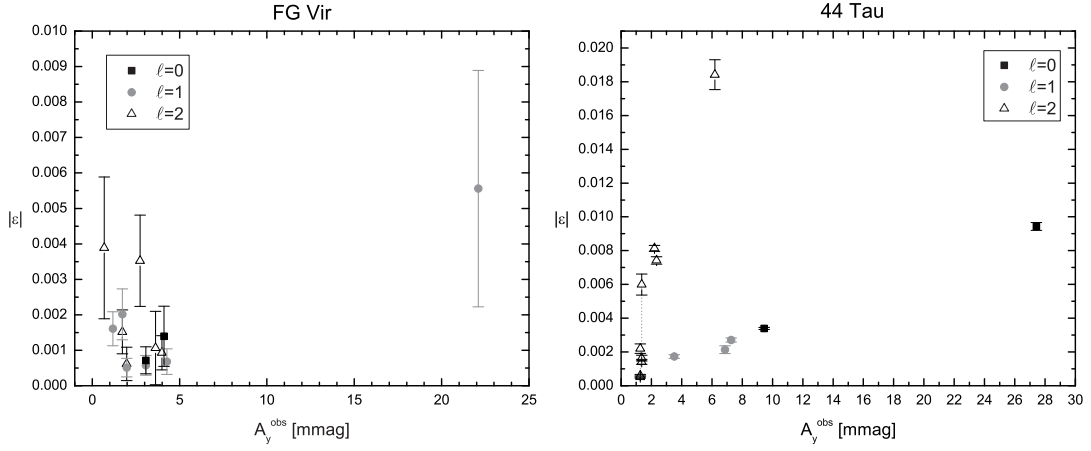


Figure 6.3: Correlation between the derived intrinsic mode amplitudes and the photometric Strömrgren y amplitudes for FG Vir (assuming $i=19^\circ$) and for 44 Tau (assuming $i=60^\circ$). The errors of the observed y amplitudes are smaller than the size of the symbols. If there are several possible identifications for one frequency, the corresponding intrinsic amplitudes are connected by lines.

affects the quadrupole modes more than the dipole modes and a confirmation of the results presented in this work with a time-dependent convection theory would be useful. Despite these uncertainties, our results show that with reliable mode identification and a good estimate for the inclination angle some constraints on the intrinsic mode amplitudes, $|\varepsilon|$, can be made which may lead to important insights in further studies of mode selection and amplitude modulation.

Frequency [cd^{-1}]	A_y [mmag]	A_{RV} [km s^{-1}]	ℓ	$ m $	$ \varepsilon $	$\sigma_{ \varepsilon }$	γ [yr^{-1}]	E_g/E_k
f_1	6.8980	27.42	0	0	0.0094	0.0003	0.01787	0.0
f_5	8.9606	9.44	0	0	0.0034	0.0001	0.14827	0.0
f_2	7.0060	6.86	1	1	0.0021	0.0003	0.01898	0.13
f_3	9.1174	3.51	1	1	0.0017	0.0002	0.00707	0.87
f_4	11.5196	7.27	1	0	0.0027	0.0002	0.10290	0.35
f_8	6.7955	2.34	2	0	0.0074	0.0003	0.00437	0.68
f_7	7.3031	6.19	2	0	0.0184	0.0009	0.01080	0.67
f_{11}	8.6391	2.21	2	0	0.0081	0.0002	0.04054	0.64

Table 6.5: Intrinsic mode amplitudes of 44 Tau for an inclination angle of 60° . Theoretical frequencies of $m=0$ modes predicted by Model 3 listed in Table 4.9.

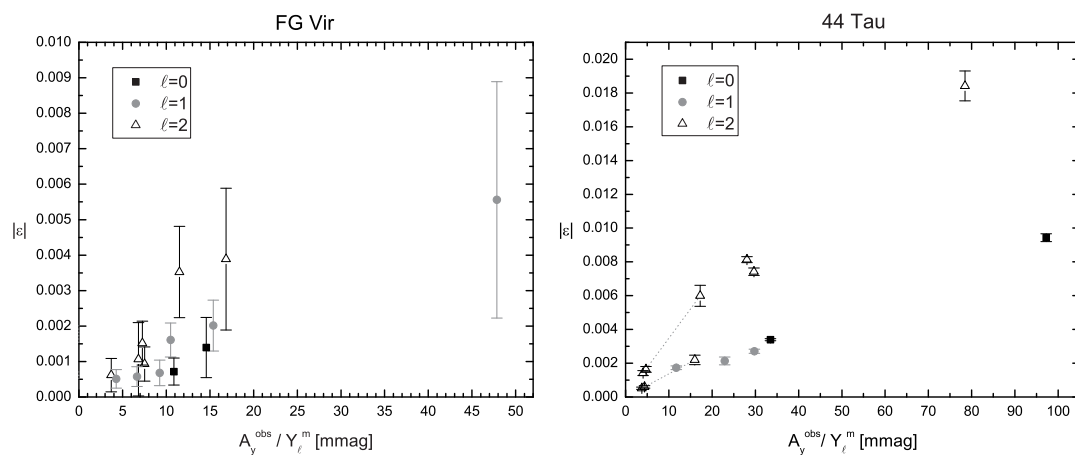


Figure 6.4: Correlation between derived intrinsic mode amplitude and the Strömgren y amplitudes divided by the aspect factor of the mode for FG Vir (left panel) and 44 Tau (right panel). The errors of y amplitudes are smaller than the size of the symbols. Ambiguous ℓ identifications are connected by a line.

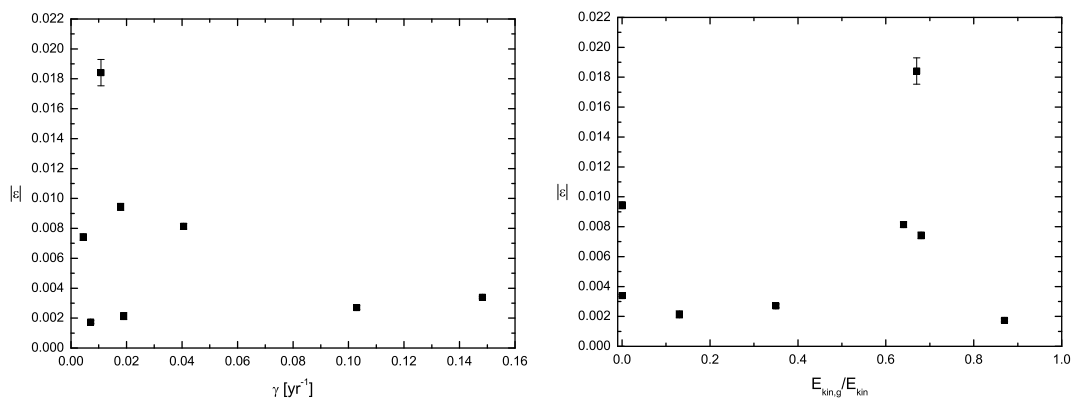


Figure 6.5: Correlation between derived intrinsic mode amplitude and growth-rates (left panel) or E_g/E_k (right panel) in 44 Tau.

Chapter 7

Conclusion

In this work mode identification and an asteroseismic analysis was carried out for the two δ Scuti stars 44 Tau and 4 CVn.

In the slowly rotating star 44 Tau the spherical degree of 10 modes could be determined by (i) modeling the observed amplitude ratios and phase differences between the Strömgren v and y passband and (ii) utilizing the method by Daszyńska-Daszkiewicz et al. (2003). The results of both methods were found to be in excellent agreement. Two modes could be identified as radial, which puts tight constraints on asteroseismic models. The detailed examination of the radial period ratio in pulsation models obtained with OPAL and OP opacities points to an underestimation of opacity by the OP opacities at temperatures around $\log T=6.05$.

An avoided crossing between two observed $\ell=1$ modes could be confirmed and played an important role in the determination of the evolutionary stage of 44 Tau. A post-MS model in the contraction phase was found to provide an excellent fit of all 15 independent frequencies observed in 44 Tau. The detected frequency spectrum can be explained solely with $\ell \leq 2$ modes. The predicted range of unstable frequencies is in excellent agreement and the fundamental parameters in good agreement with observations. 44 Tau, therefore, is an example for a successful determination of the evolutionary stage of a star by asteroseismology.

The excellent fit of the observed modes allowed to investigate the efficiency of partial element mixing and the extent of the overshoot layer above the convective core through mixed modes. Different models of the hydrogen abundance profile were tested according to the approach described in Dziembowski & Pamyatnykh (2008). The results favor efficient mixing in a small overshoot layer to inefficient mixing in a large overshoot layer. The main uncertainties in the determination of the size of the partially mixed layer arise from the uncertainties in the opacities.

The observed amplitude modulation of 44 Tau between 2000 and 2006 was examined. Different reasons for amplitude variability, such as beating between close frequencies or

resonance phenomena, were examined. However, the time base line of the observations is too short to draw definitive conclusions on the cause of the amplitude modulations.

The second star examined in this work is 4 CVn. This star exhibits a $v \sin i$ of approximately 120 km s^{-1} and metal overabundance. Based on unpublished data the spherical degree of five modes could be uniquely determined by means of photometric mode identification. The results from the mode identification method by Daszyńska-Daszkiewicz et al. (2003) were shown to be partly affected by the fast rotation of the star. At the present stage no components of the same rotationally split multiplet could be confirmed.

Unfortunately, the mode identification of 4 CVn does not put as tight constraints to the models as in the case of 44 Tau. Only one radial mode was found. Therefore, there are many free parameters in the asteroseismic modeling of 4 CVn of which the unknown equatorial rotation rate is of main concern. The second order perturbation approach used in this work is not well suited to accurately predict the frequencies of individual modes in 4 CVn and corresponding uncertainties have to be taken into account. The comparison between observed and predicted fundamental parameters points to an identification as the radial first or second overtone. These results are confirmed by the predicted instability ranges. The best agreement between the theoretical and the observed frequency range is found if the radial mode is assumed to be the second overtone. At the present stage the evolutionary stage is still unclear and the theoretical frequency spectra computed for each evolutionary stage do not show a clear preference. The case of 4 CVn shows that more mode identifications are still necessary to put additional constraints on the models.

Finally, we showed that if the spherical degree and the azimuthal order of pulsation modes, and the stellar inclination angle are well determined (such as in 44 Tau and FG Vir), estimates of the intrinsic mode amplitudes can be derived. The mode amplitudes were found to range between approximately 0.05 and 2 % of the stellar radius. The comparison between the intrinsic amplitudes of 44 Tau and the corresponding linear growth rates does not show a correlation. Hence nonlinear effects are important to explain the given mode amplitudes. These empirical data for the mode amplitudes may be important input data for the nonlinear pulsation theory.

Bibliography

- Aerts, C. 1996, *A&A*, 314, 115
- Aizenman, M., Smeyers, P., & Weigert, A. 1977, *A&A*, 58, 41
- Alexander, D. R. & Ferguson, J. W. 1994, *ApJ*, 437, 879
- Antoci, V., Breger, M., Rodler, F., Bischof, K., & Garrido, R. 2007, *A&A*, 463, 225
- Asplund, M., Grevesse, N., & Sauval, A. J. 2005, in *Astronomical Society of the Pacific Conference Series*, Vol. 336, *Cosmic Abundances as Records of Stellar Evolution and Nucleosynthesis*, ed. T. G. Barnes, III & F. N. Bash, 25–+
- Asplund, M., Grevesse, N., Sauval, A. J., Allende Prieto, C., & Kiselman, D. 2004, *A&A*, 417, 751
- Badnell, N. R., Bautista, M. A., Butler, K., et al. 2005, *MNRAS*, 360, 458
- Bahcall, J. N., Pinsonneault, M. H., & Wasserburg, G. J. 1995, *Reviews of Modern Physics*, 67, 781
- Baker, N. & Kippenhahn, R. 1965, *ApJ*, 142, 868
- Balona, L. A. 1986, *MNRAS*, 219, 111
- Balona, L. A. & Evers, E. A. 1999, *MNRAS*, 302, 349
- Balona, L. A. & Stobie, R. S. 1979, *MNRAS*, 189, 659
- Bessell, M. S., Castelli, F., & Plez, B. 1998, *A&A*, 333, 231
- Böhm-Vitense, E. 1958, *Zeitschrift für Astrophysik*, 46, 108
- Breger, M. 2000, *MNRAS*, 313, 129
- Breger, M. & Bischof, K. M. 2002, *A&A*, 385, 537
- Breger, M., Handler, G., Garrido, R., et al. 1999a, *A&A*, 349, 225
- Breger, M. & Lenz, P. 2008, *A&A*, 488, 643

- Breger, M., Lenz, P., Antoci, V., et al. 2005, *A&A*, 435, 955
- Breger, M., Lenz, P., & Pamyatnykh, A. A. 2009, *MNRAS*, 396, 291
- Breger, M. & Pamyatnykh, A. A. 2006a, *MNRAS*, 368, 571
- Breger, M. & Pamyatnykh, A. A. 2006b, *MNRAS*, 368, 571
- Breger, M., Pamyatnykh, A. A., Pikall, H., & Garrido, R. 1999b, *A&A*, 341, 151
- Breger, M., Stich, J., Garrido, R., et al. 1993, *A&A*, 271, 482
- Buchler, J. R., Goupil, M.-J., & Hansen, C. J. 1997, *A&A*, 321, 159
- Buchler, J. R., Goupil, M. J., & Serre, T. 1995, *A&A*, 296, 405
- Castanheira, B. G., Breger, M., Beck, P. G., et al. 2008, *Communications in Asteroseismology*, 157, 124
- Castor, J. I. 1968, *ApJ*, 154, 793
- Christensen-Dalsgaard, J. 2009, ArXiv e-prints
- Christensen-Dalsgaard, J. & Däppen, W. 1992, *A&A Rev.*, 4, 267
- Christensen-Dalsgaard, J., di Mauro, M. P., Houdek, G., & Pijpers, F. 2009, *A&A*, 494, 205
- Christy, R. F. 1966, *ARA&A*, 4, 353
- Claret, A. 2000, *A&A*, 363, 1081
- Cox, A. N., Morgan, S. M., Rogers, F. J., & Iglesias, C. A. 1992, *ApJ*, 393, 272
- Cox, J. P. 1963, *ApJ*, 138, 487
- Cox, J. P. 1984, *PASP*, 96, 577
- Crawford, D. L. 1975, *AJ*, 80, 955
- Däppen, W. & Guzik, J. A. 2000, in *NATO ASIC Proc. 544: Variable Stars as Essential Astrophysical Tools*, 177–+
- Daszyńska-Daszkiewicz, J., Dziembowski, W. A., & Pamyatnykh, A. A. 2003, *A&A*, 407, 999
- Daszyńska-Daszkiewicz, J., Dziembowski, W. A., & Pamyatnykh, A. A. 2005a, *A&A*, 441, 641
- Daszynska-Daszkiewicz, J., Dziembowski, W. A., & Pamyatnykh, A. A. 2007, *Acta Astronomica*, 57, 11

- Daszyńska-Daszkiewicz, J., Dziembowski, W. A., Pamyatnykh, A. A., et al. 2005b, *A&A*, 438, 653
- Daszyńska-Daszkiewicz, J., Dziembowski, W. A., Pamyatnykh, A. A., & Goupil, M.-J. 2002, *A&A*, 392, 151
- Daszyńska-Daszkiewicz, J. & Walczak, P. 2009, *MNRAS*, 1046
- Dupret, M.-A., Grigahcène, A., Garrido, R., Gabriel, M., & Scuflaire, R. 2004, *A&A*, 414, L17
- Dziembowski, W. 1977a, *Acta Astronomica*, 27, 203
- Dziembowski, W. 1977b, *Acta Astronomica*, 27, 95
- Dziembowski, W. 1980, in *Lecture Notes in Physics*, Berlin Springer Verlag, Vol. 125, Nonradial and Nonlinear Stellar Pulsation, ed. H. A. Hill & W. A. Dziembowski, 22–33
- Dziembowski, W. 1982, *Acta Astronomica*, 32, 147
- Dziembowski, W. & Krolikowska, M. 1985, *Acta Astronomica*, 35, 5
- Dziembowski, W. & Krolikowska, M. 1990, *Acta Astronomica*, 40, 19
- Dziembowski, W., Krolikowska, M., & Kosovitch, A. 1988, *Acta Astronomica*, 38, 61
- Dziembowski, W. A. 1971, *Acta Astronomica*, 21, 289
- Dziembowski, W. A. 1975, *Memoires of the Societe Royale des Sciences de Liege*, 8, 287
- Dziembowski, W. A. & Goode, P. R. 1992, *ApJ*, 394, 670
- Dziembowski, W. A., Moskalik, P., & Pamyatnykh, A. A. 1993, *MNRAS*, 265, 588
- Dziembowski, W. A. & Pamyatnykh, A. A. 1993, *MNRAS*, 262, 204
- Dziembowski, W. A. & Pamyatnykh, A. A. 1991, *A&A*, 248, L11
- Dziembowski, W. A. & Pamyatnykh, A. A. 2008, *MNRAS*, 385, 2061
- Eddington, A. S. 1919, *MNRAS*, 79, 177
- Ferguson, J. W., Alexander, D. R., Allard, F., et al. 2005, *ApJ*, 623, 585
- Fossati, L., Kolenberg, K., Reegen, P., & Weiss, W. 2008, *A&A*, 485, 257
- García Hernández, A., Moya, A., Michel, E., et al. 2009, *ArXiv e-prints*
- Garrido, R. 2000, in *Astronomical Society of the Pacific Conference Series*, Vol. 210, Delta Scuti and Related Stars, ed. M. Breger & M. Montgomery, 67–+
- Gautschy, A. & Saio, H. 1996, *ARA&A*, 34, 551

- Glebocki, R. & Stawikowski, A. 2000, *Acta Astronomica*, 50, 509
- Goupil, M.-J., Dziembowski, W. A., Pamyatnykh, A. A., & Talon, S. 2000, in *Astronomical Society of the Pacific Conference Series*, Vol. 210, *Delta Scuti and Related Stars*, ed. M. Breger & M. Montgomery, 267–+
- Grevesse, N. & Noels, A. 1993, in *Origin and Evolution of the Elements*, ed. N. Prantzos, E. Vangioni-Flam, & M. Casse, 15–25
- Guzik, J. A., Bradley, P. A., & Templeton, M. R. 2000, in *Astronomical Society of the Pacific Conference Series*, Vol. 210, *Delta Scuti and Related Stars*, ed. M. Breger & M. Montgomery, 247–+
- Hauck, B. & Mermilliod, M. 1997, *VizieR Online Data Catalog*, 2215, 0
- Heiter, U., Kupka, F., van't Veer-Menneret, C., et al. 2002, *A&A*, 392, 619
- Henry, G. W. & Fekel, F. C. 2005, *AJ*, 129, 2026
- Heney, L. G., Forbes, J. E., & Gould, N. L. 1964, *ApJ*, 139, 306
- Iglesias, C. A. & Rogers, F. J. 1996, *ApJ*, 464, 943
- Kurtz, D. W. 1982, *MNRAS*, 200, 807
- Lenz, P. & Breger, M. 2005, *Communications in Asteroseismology*, 146, 53
- Lignières, F., Rieutord, M., & Reese, D. 2006, *A&A*, 455, 607
- Loumos, G. L. & Deeming, T. J. 1978, *Ap&SS*, 56, 285
- Lovekin, C. C. & Deupree, R. G. 2008, *ApJ*, 679, 1499
- Mantegazza, L. & Poretti, E. 2002, *A&A*, 396, 911
- McNamara, D. H. & Powell, J. M. 1985, *PASP*, 97, 1101
- Meléndez, J. & Ramírez, I. 2003, *A&A*, 398, 705
- Miglio, A., Montalbán, J., & Dupret, M.-A. 2007, *MNRAS*, 375, L21
- Mittermayer, P. & Weiss, W. W. 2003, *A&A*, 407, 1097
- Montalbán, J. & Dupret, M.-A. 2007, *A&A*, 470, 991
- Montalban, J. & Miglio, A. 2008, *Communications in Asteroseismology*, 157, 160
- Moskalik, P. 1985, *Acta Astronomica*, 35, 229
- Moskalik, P. & Dziembowski, W. A. 1992, *A&A*, 256, L5

- Nendwich, J., Heiter, U., Kupka, F., Nesvacil, N., & Weiss, W. W. 2004, *Communications in Asteroseismology*, 144, 43
- Nowakowski, R. M. 2005, *Acta Astronomica*, 55, 1
- Nowakowski, R. M. & Dziembowski, W. A. 2003, *Ap&SS*, 284, 273
- Paczyński, B. 1969, *Acta Astronomica*, 19, 1
- Paczyński, B. 1970a, *Acta Astronomica*, 20, 47
- Paczyński, B. 1970b, *Acta Astronomica*, 20, 195
- Paczyński, B. 1970c, *Acta Astronomica*, 20, 287
- Pamyatnykh, A. A., Handler, G., & Dziembowski, W. A. 2004, *MNRAS*, 350, 1022
- Pérez Hernández, F., Claret, A., Hernández, M. M., & Michel, E. 1999, *A&A*, 346, 586
- Petersen, J. O. & Jørgensen, H. E. 1972, *A&A*, 17, 367
- Poretti, E., Michel, E., Garrido, R., et al. 2009, *ArXiv e-prints*
- Reese, D., Lignières, F., & Rieutord, M. 2006, *A&A*, 455, 621
- Rogers, F. J., Swenson, F. J., & Iglesias, C. A. 1996, *ApJ*, 456, 902
- Roxburgh, I. W. 2004, *A&A*, 428, 171
- Roxburgh, I. W. 2006, *A&A*, 454, 883
- Royer, F., Grenier, S., Baylac, M.-O., Gómez, A. E., & Zorec, J. 2002, *A&A*, 393, 897
- Rufener, F. 1976, *A&AS*, 26, 275
- Scuflaire, R. 1974, *A&A*, 36, 107
- Seaton, M. J. 2005, *MNRAS*, 362, L1
- Seaton, M. J. & Badnell, N. R. 2004, *MNRAS*, 354, 457
- Smith, M. A. 1982, *ApJ*, 254, 242
- Solano, E. & Fernley, J. 1997, *A&AS*, 122, 131
- Stellingwerf, R. F. 1978, *ApJ*, 224, 953
- Suárez, J. C., Garrido, R., & Goupil, M. J. 2006, *A&A*, 447, 649
- Templeton, M., Basu, S., & Demarque, P. 2001, *ApJ*, 563, 999
- Templeton, M., Basu, S., & Demarque, P. 2002, *ApJ*, 576, 963

Townsend, R. H. D. 2003, *MNRAS*, 343, 863

Viskum, M., Kjeldsen, H., Bedding, T. R., et al. 1998, *A&A*, 335, 549

Watson, R. D. 1988, *Ap&SS*, 140, 255

Yakovlev, D. G. & Urpin, V. A. 1980, *Soviet Astronomy*, 24, 303

Zhou, A. 1998, *Delta Scuti Star Newsletter*, 12, 13

Zima, W. 2008, *Communications in Asteroseismology*, 157, 387

Zima, W., Lehmann, H., Stütz, C., Ilyin, I. V., & Breger, M. 2007, *A&A*, 471, 237

Zima, W., Wright, D., Bentley, J., et al. 2006, *A&A*, 455, 235

Appendix A

Appendix

A.1 Zusammenfassung

δ Scuti Sterne sind pulsierende Sterne, die sowohl radiale Schwingungsmoden als auch nicht-radiale Druck- und Schwerkraftmoden aufweisen. Der Hauptaspekt dieser Arbeit ist die Bestimmung der Geometrie der Schwingungsmoden (Modenidentifikation) und eine asteroseismische Analyse der δ Scuti Sterne 44 Tau und 4 CVn.

Der langsam rotierende Stern 44 Tau pulsiert mit 15 unabhängigen Frequenzen. Für die 10 dominanten Moden konnte der Grad der zugehörigen Kugelflächenfunktion ermittelt werden. Zwei radiale Moden und die Interaktion zwischen einer Druck- und Schwerkraftdipolmode schränken die möglichen Pulsationsmodelle stark ein. Ausgehend von den erhaltenen Modenidentifikationen, wurden Modelle in allen drei möglichen Entwicklungsphasen untersucht: der Hauptreihenphase, der darauf folgenden Kontraktionsphase und der Nach-Hauptreihen-Expansionsphase. Ein Pulsationsmodell in der Nach-Hauptreihen-Kontraktionsphase zeigt eine ausgezeichnete Übereinstimmung mit allen 15 beobachteten Frequenzen.

Der Vergleich asteroseismischer Modelle, die mit OPAL und OP Opazitäten berechnet wurden, deutet darauf hin, dass die OP Opazitäten die wahre Opazität bei einer Temperatur von $1.1 \cdot 10^6$ K unterschätzen. Die Auswirkung der unterschiedlichen Modellierung der Mischung zwischen dem konvektiven Kern und den darüberliegenden radiativen Schichten wurde getestet. Die Übereinstimmung zwischen theoretischen und beobachteten Frequenzen ist für ein Modell, das eine effiziente Elementvermischung innerhalb einer schmalen Schichtdicke annimmt, besser als bei einer ineffizienten Elementvermischung in einer größeren Schicht.

Im Stern 4 CVn konnte nur eine Schwingungsmode als radial identifiziert werden. Die Modenidentifikation erlaubt in diesem Fall keine so starken Einschränkungen der asteroseismischen Modelle wie für 44 Tau. Eine allgemeine Modellstudie lässt den Schluss zu, dass es sich bei der radialen Mode um den zweiten Oberton oder, jedoch mit geringerer Wahrscheinlichkeit, um den ersten Oberton handelt.

Weiters wird anhand der zwei δ Scuti Sterne 44 Tau und FG Vir gezeigt, dass mit eindeutiger Modenidentifikation und bekanntem Inklinationswinkel die intrinsischen Amplituden der Pulsationsmoden aus den Beobachtungen abgeschätzt werden können.

A.2 Abstract

The δ Scuti stars are pulsating stars which exhibit radial modes as well as nonradial low-order acoustic and gravity modes. The main scope of this work is the determination of the spherical mode degrees and an asteroseismic analysis of the δ Scuti stars 44 Tau and 4 CVn.

The slowly rotating star 44 Tau pulsates in 15 independent frequencies. For the 10 dominant modes the spherical degree could be determined. Two radial modes and an avoided crossing between two dipole modes put strong constraints on the models. Taking into account the mode identifications, models in all three possible evolutionary stages were examined: the main sequence phase, the overall contraction phase after the TAMS and the post-main sequence expansion phase. A model in the post-main sequence contraction phase was found to provide an excellent fit of all 15 observed frequencies.

The comparison of asteroseismic models computed with OPAL and OP opacities indicates that the OP opacities underestimate the true opacity at a temperature of approximately $1.1 \cdot 10^6$ K. The effect of different modeling of the partially mixed region above the convective core on the mixed modes were tested. The fit between theoretical and observed frequencies is better for a model with efficient mixing in a small overshoot layer than inefficient mixing in a more extended overshoot layer.

For the star 4 CVn only one mode could be identified as radial. Consequently the mode identifications do not put as strong constraints on the asteroseismic models as for 44 Tau. A general model survey allows to conclude that the radial mode is the second or, less likely, the first overtone.

It is shown for the case of the two δ Scuti stars 44 Tau and FG Vir that with unambiguous mode identifications and a well constrained inclination angle an estimate of the intrinsic mode amplitudes can be derived.

A.3 Danksagung / Acknowledgement

Ich danke Michel Breger für seine langjährige Unterstützung, viele Diskussionen beim Mittagessen und die Freiheiten, die er mir bei meiner Arbeit gelassen hat.

I would like to thank Alosa Pamyatnykh for providing the computer codes used in this work, many scientific discussions and introducing me to the world of long-distance bicycle tours.

Ich danke Vichi Antoci für viele wissenschaftliche Diskussionen und ihre sehr wertvollen Kommentare zur ersten Version dieses Manuskripts.

Danke auch an Gerald Handler für das Korrekturlesen der Arbeit und für das Erwecken der Begeisterung für das Drachenboot-Paddeln, das oft geholfen hat, den Kopf etwas frei zu bekommen.

Ich danke Paul Beck für die vielen gemeinsamen Mittagessen und dass er mich oft gezwungen hat, gewisse wissenschaftliche Aspekte der Pulsationstheorie zu erklären. Das hat mir selber oft geholfen.

Mein Dank gilt auch Wolfgang Zima für die Überprüfung der Radialgeschwindigkeiten auf Frequenzen an theoretisch vorhergesagten Werten des 44 Tau Modells.

Ich danke auch allen anderen aktuellen und ehemaligen Mitgliedern der TOPS Gruppe für die schöne Zeit, die wir gemeinsam verbrachten.

The radial velocity data of 4 CVn presented in this work were obtained with the software package FAMIAS developed in the framework of the FP6 European Coordination Action HELAS (<http://www.helas-eu.org/>)

A.4 Lebenslauf

Name: Patrick Lenz
 Titel: Mag. rer. nat.
 Geboren am: 5. Februar 1981
 Geburtsort: Dornbirn, Vorarlberg
 Staatsbürgerschaft: Österreich

Schulische Ausbildung

1987 - 1991 Volksschule Dornbirn-Haselstauden
 1991 - 1995 Hauptschule Dornbirn-Haselstauden
 1995 - 1999 Bundesoberstufenrealgymnasium Lauterach
 (naturwissenschaftlicher Zweig)
 24. Juni 1999 Reifeprüfung mit ausgezeichnetem Erfolg bestanden

Akademische Ausbildung

10/1999 Beginn des Astronomie-Studiums an der Universität Wien
 10/2000 - 09/2001 Unterbrechung des Studiums zwecks Ableistung des Zivildienstes
 in den Pfarreien Bregenz-Mariahilf und Dornbirn-Schoren
 18. Dez. 2002 1. Diplomprüfung mit ausgezeichnetem Erfolg abgeschlossen
 24. Nov. 2005 Studienabschluss, 2. Diplomprüfung mit ausgezeichnetem Erfolg abgeschlossen.
Titel der Diplomarbeit: Period04 - A statistical software package to
 extract multiple periodicities from astronomical data sets
Betreuer: Michel Breger
 03/2006 Beginn des Doktoratsstudiums (Dissertationsgebiet Astronomie)
Betreuer: Michel Breger

Beobachtungsaufenthalte

10. April - 13. Mai 2003 Siding Spring Observatory, Australien
 (FG Virginis Kampagne 2003)
 8. Juli - 26. August 2005 Siding Spring Observatory, Australien
 (HD210111/UV Oct/SS For Kampagne 2005)

Forschungsaufenthalte

20. - 24. Februar 2006 Copernicus Astronomical Center, Warschau, Polen
 21. - 25. Mai 2007 Copernicus Astronomical Center, Warschau, Polen
 18. - 22. Februar 2008 Copernicus Astronomical Center, Warschau, Polen
 22. - 25. Juni 2009 Copernicus Astronomical Center, Warschau, Polen

Studienbegleitende Tätigkeiten

10/2002 - 12/2004	Mitarbeit im Rahmen des FWF-Projekts PHY-P14546
01/2005 - 12/2005	Mitarbeit im Rahmen des FWF-Projekts PHY-P17441
SS2003	Tutor für die Lehrveranstaltung EDV in der Astronomie
WS2003-WS2008	Tutor für das Observatoriumspraktikum (Nordkuppelbeobachtung)
01/2006 - 12/2006	Bezug eines Forschungsstipendiums der Universität Wien
01/2007 - 12/2008	Mitarbeit im Rahmen des FWF-Projekts PHY-P17441